RENE Master of Science,
KTH Royal Institute of Technology,
Stockholm, Sweden, Jun-Dec 2020.

Imperial College London

Vestas

InnoEnergy

Master Thesis Report

Loads Control Aerodynamic in Offshore Wind Turbines

Lorenzo Cantoni

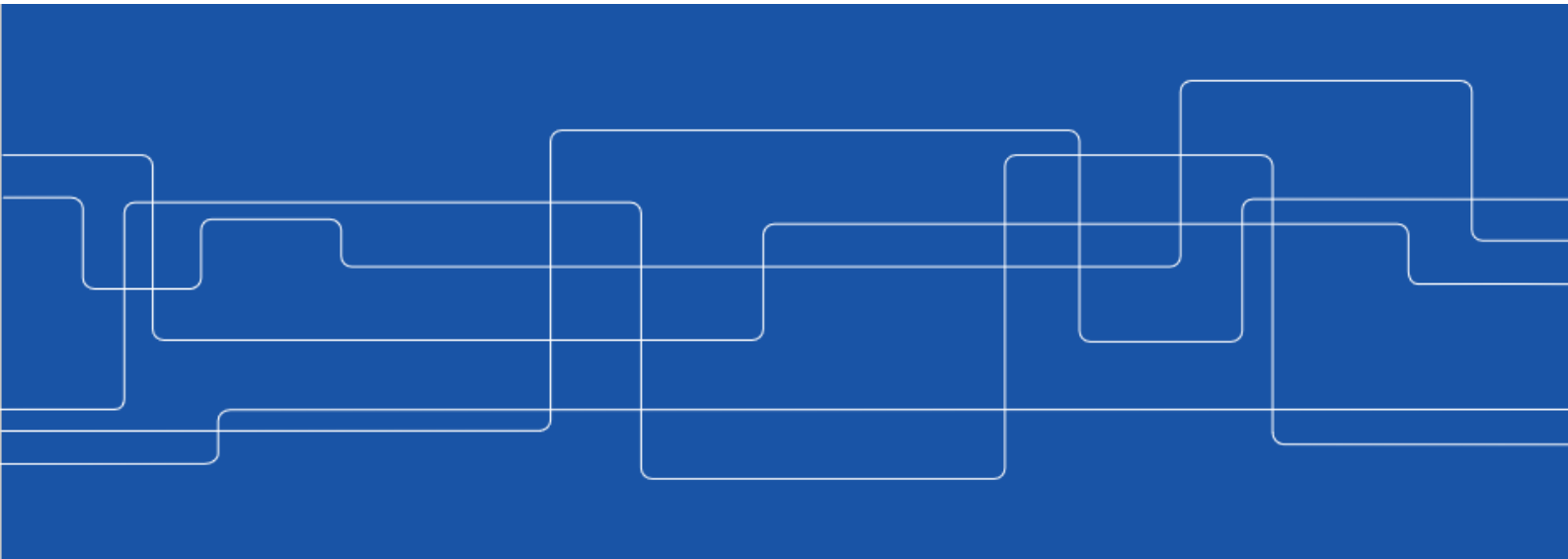

Authors

Lorenzo Cantoni <lorenzo.cantoni95@gmail.com>
School of Industrial Engineering and Management
KTH Royal Institute of Technology

Parties involved in the Project

Lorenzo Cantoni
KTH Royal Institute of Technology
Imperial College London
Vestas Wind Systems A/S

Examiners

Andrew Martin
Professor, Department of Energy Technology, KTH Royal Institute of Technology

Supervisor

Ricardo Vinuesa Motilva
Assistant Professor, KTH Royal Institute of Technology

Abstract

Due to the increase of rotor size in horizontal axis wind turbine (HAWT) during the past 25 years in order to achieve higher power output, all wind turbine components and blades in particular, have to withstand higher structural loads. This upscaling problem could be solved by applying technologies capable of reducing aerodynamic loads the rotor has to withstand, either with passive or active control solutions.

These control devices and techniques can reduce the fatigue load upon the blades up to 40% and therefore less maintenance is needed, resulting in an important money savings for the wind farm manager. This project consists in a study of load control techniques for offshore wind turbines from an aerodynamic and aeroelastic point of view, with the aim to assess a cost effective, robust and reliable solution which could operate maintenance free in quite hostile environments.

The first part of this study involves 2D and 3D aerodynamic and aeroelastic simulations to validate the computational model with experimental data and to analyze the interaction between the fluid and the structure. The second part of this study is an assessment of the unsteady aerodynamic loads produced by a wind gust over the blades and to verify how a trailing edge flap would influence the aerodynamic control parameters for the selected wind turbine blade.

Keywords

Wind Turbine, Offshore, Blade, Rotor, Computational Fluid Dynamics, Airfoil, Aerodynamic, Aeroelasticity, Simulation, Fluid, Structure, Interaction, Loads, Control, Response, Harmonics, Vibration, Damping, Flutter, Trailing Edge, Flaps, Wind Gust, Lift, Drag, Unsteady, Pressure, Velocity

Acknowledgements

I would like to thank the following people, without whom I would not have been able to complete this research project, and without whom I would not have made it through my Masters Degree Programme with InnoEnergy!

The Aeroelasticity Group at Imperial College London, especially to my supervisor Professor Mehdi Vahdati, whose insight and knowledge into the subject matter steered me through this interesting research topic. And special thanks to Kirubakaran, whose support as part of his PhD allowed my studies to go the extra mile (sorry for all the extra work and countless questions Karan!).

The wind energy company Vestas, which gave me the opportunity to have access to a lot of data useful for my purpose, especially with Dr. Tomas Vronsky who supported me during the whole research period. Thanks also to Professor Ricardo Vinuesa to be my supervisor at KTH and to guide me through the administrative process for the completion of my Master Degree in Stockholm.

And my biggest thanks to my family for all the support you have shown me through this research, the culmination of two years of distance learning. For my good friends who have been by my side all my life, and for all the new friends I have made during this fantastic InnoEnergy Master Program in Barcelona and Stockholm. Special thanks mainly to Berto (Lini), Urielle, Beona, Martino, Anto, Albert and Filipe. Thanks a lot also to my personal digital creator and old friend Luca Luke Martini to help me with the creation of the digital contents and videos shown during the presentation of the project, your help was fundamental for me man.

Finally, many thanks to all participants and places that took part in this study path and enabled everything I have done to be possible.

Acronyms

CFD Computational Fluid Dynamics

HAWT Horizontal Axis Wind Turbine

VAWT Vertical Axis Wind Turbine

LCOE Levelized Cost Of Energy

AFC Active Flow Control

DOF Degree of Freedom

UAE Unsteady Aerodynamics Experiment

BEM Blade Element Momentum

ABL Atmospheric Boundary Layer

LES Large Eddies Simulation

EOG Extreme Operating Gust

Contents

List of Figures

List of Tables

Chapter 1

Introduction

Due to the uncertainties and risks associated with the price of fossil fuel, investment in renewable energy sources such as wind power, with the nature of being a stable and long term alternative, has been an increasingly favourable choice in the energy sector with growing investment in both the European Union and the United States [78]. Among all the renewable energy sources, both onshore and offshore wind power are among the cleanest when the environmental impact of various renewable energy sources are considered [82]. Therefore, there have been growing research interests in assessing and optimising wind turbine designs, especially how to increase the rotor size maintaining good safety structural requirements.

1.1 Problem Overview

During the past 25 years, the size of utility scale horizontal axis wind turbines grew uninterrupted, constantly seeking a reduction of the cost of energy, as it is shown in figure 1.1.1. As the rotor size increases, all wind turbine components, and the blades in particular, have to withstand higher loads. In the past, the higher structural requirements were mainly satisfied by increasing the weight of the structure, or by employing more expensive compounds with an higher specific strength [9]. According to Sieros et al. [67] such growing trend is likely to hit a limit, above which further upscale of the turbine size would not yield any benefit in term of cost reduction, unless technological breakthrough are introduced to allow for further upscale in a cost-efficient way.

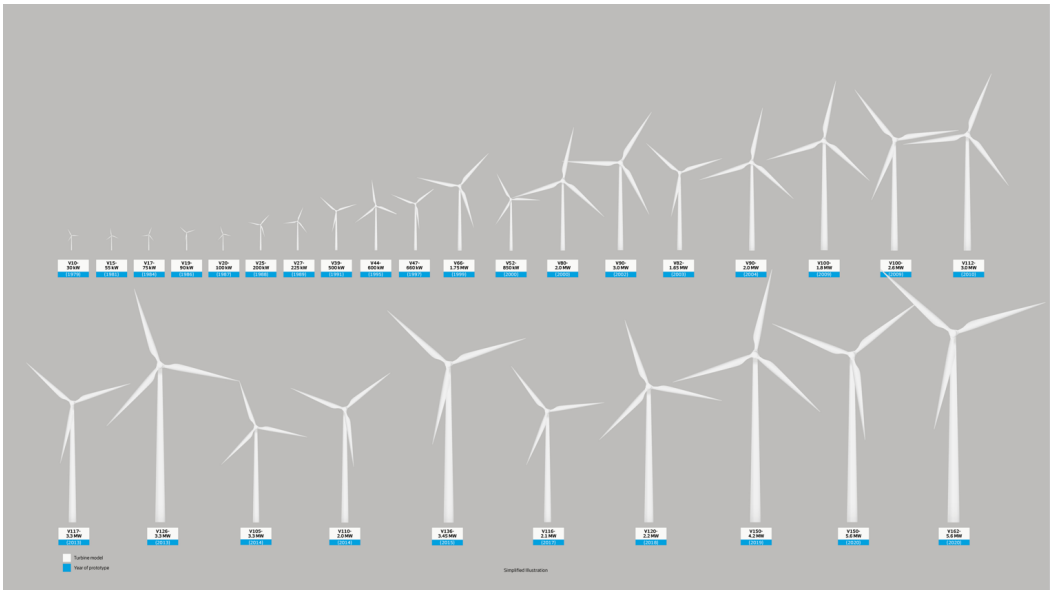

Figure 1.1.1: Continuous growth of rated power during the last years

The upscale problem could be solved by applying technologies capable of reducing the aerodynamic loads the rotor has to withstand, either with passive or active load control solutions. Passive load control could be achieved by bend-twist aeroelastic coupling of the blades deformations: the blades would respond to an increase of the aerodynamic forces with a torsion deformation that twist the blade toward lower angles of attack, and therefore reduces aerodynamic loads [14]. Active load control is instead achieved by a wind turbine rotor that, through a combination of sensor, control units, and actuators, compensates for the variation in the wind field swept by the blades, and thus actively reduces the aerodynamic loads it has to withstand.

1.2 Scope of the Work and Project Outline

The aim of this project is to calculate and reduce the loads upon an offshore wind turbine blade with an aerodynamic simulation tool able to account for the presence of an adaptive trailing edge flap. In this way it is possible to gain an insight on the effects this solution has on the aerodynamic and aeroelastic forces, hence on the response of the structure and loads experienced by the blades. With these insights it will be possible to understand the blade loads reduction and, in particular, the changing in lift due to input wind gust will be analysed. Thanks to this load reduction, it would be possible to minimize the maintenance in the hostile environment of an offshore wind turbine.

The starting point of this study is a literature review about aerodynamic, aeroelasticity and structural mechanics of an offshore wind turbine, to gain a good problem overview and to understand the state of the art of load control techniques. Moreover, a validation of the numerical method will be done to assess its accuracy, comparing the results of the Computational Fluid Dynamics (CFD) simulation with experimental data obtained in the wind tunnel test.

Afterwards, a 3D fluid structure-interaction analysis will be performed to a specific wind turbine blade, using the provided specifications. From the results it will be possible to analyze the reaction of the blade to the incoming wind, studying the total deformations, stresses and forces experienced by the blade.

Finally, the effectiveness of applying a trailing edge flap to the airfoil during a wind gust will be assessed. The airfoil response with its standard configuration will be tested and then compared to the configuration including the movable flap, in order to understand the importance and the possible application of this devise in reducing the loads produced by an incoming wind gust.

1.3 Wind Turbine Layout: HAWT vs VAWT

Depending on the axis relative to the ground plane that wind turbines rotate about, they can be divided into two categories: Horizontal Axis Wind Turbine (HAWT) and Vertical Axis Wind Turbine (VAWT), among which the former is more common and better developed for commercial applications.

Wind turbines date back to 200 B.C. in the world's history, and the most famous HAWTs were evidently the Dutch windmills. The most important components of an HAWT are located on the top of the tower, which capture the kinetic energy of the wind and ultimately convert it in to electrical energy. The reception of mechanical energy from the air stream is completed by the rotation of the turbine blades about the rotor shaft due to the lift force generated on the blades. The torque induced drive then goes through gear box and the generator does the rest of the job [27]. An horizontal axis wind turbine must face directly to the wind in either upwind or downwind setup in order to achieve the best efficiency and also avoid fatigue failure by cyclic loading. Older and smaller HAWTs can be adjusted manually with the help of wind vanes, while modern larger ones usually employ automated yaw drives [27].

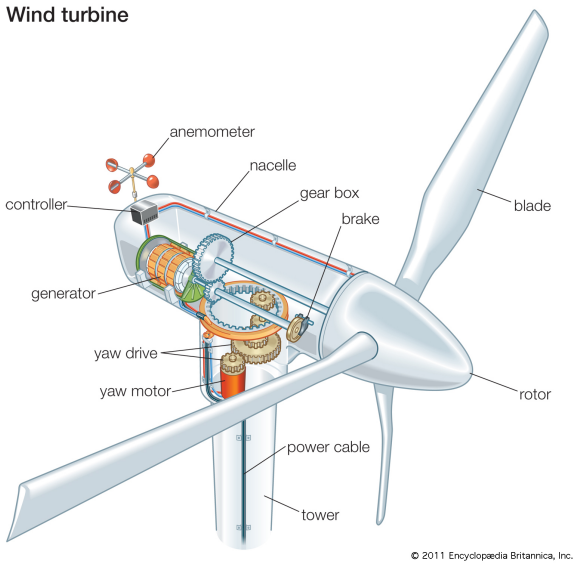

Figure 1.3.1: Components of an HAWT

VAWT has quite different structural layout and operation conditions. The gearbox and generator which sit on the top of the tower of a HAWT now can be placed directly on the ground as the rotating shaft goes vertically to the bottom. Moreover, vertical axis wind turbines can operate regardless of the incoming wind direction as they generally have helical blades along the axis, however some may require a start motor at low wind speed [4].

Figure 1.3.2: Layout of a VAWT

1.4 Load Control in a Wind Turbine

The key quantity when it comes to assess the competitiveness of a source of energy is the Levelized Cost Of Energy (LCOE), given by Equation 1.1, which must be kept as low as possible [25].

$$LCOE = \frac{\text{Sum of Costs Over Lifetime (Capital Costs + O\&M Costs)}}{\text{Sum of Energy Produced Over Lifetime}} \tag{1.1}$$

Looking at this equation, there are several ways to lower the LCOE. The first one is to decrease the capital cost. This can be achieved by decreasing the amount of materials or improving manufacturing techniques. Another way would be to reduce the Operation and Maintenance (O&M) costs by making more reliable turbines [25].
The last way, which is the most relevant in this project, is to increase the Sum of Energy Produced Over Lifetime. There are two factors influencing this quantity for a wind turbine: its size and its lifetime [25]. These two parameters are linked: by increasing the rotor diameter, which is the current design trend, one would impose higher loads to the structure and hence reduce its lifetime. Nowadays, it is thus a prime objective to control the loads on a wind turbine and more and more techniques are being investigated to this end. Of course, this load control cannot be done without considering the power output of the wind turbine, the main quantity of interest as it is directly related to the production of energy. Figure 1.4.1 presents the typical power curve of a commercial wind turbine.

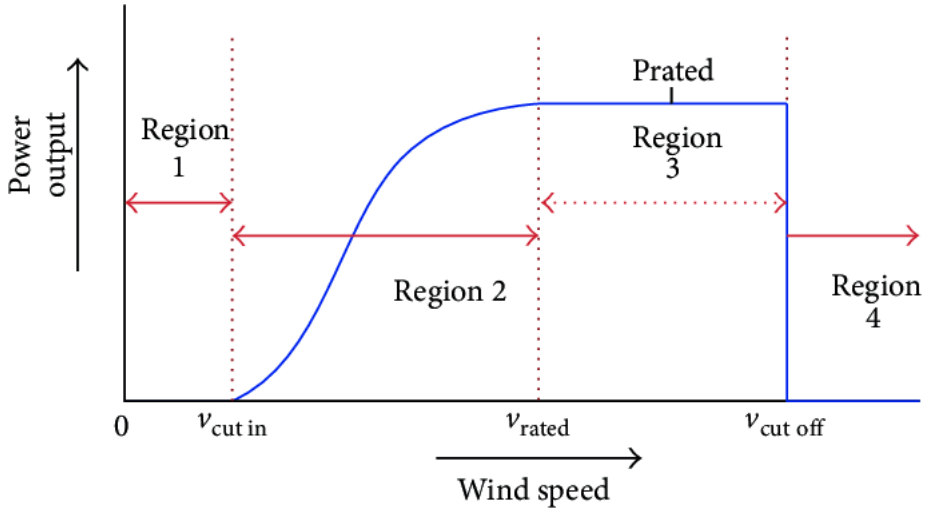

Figure 1.4.1: Simplified power curve for commercial wind turbine

The regions of interest when it comes to load control are regions 2 and 4. In region 2, the turbine operates below design - or rated - power. Near region 4, the wind speed is higher than the design wind speed and thus the power output is the same but with higher loads which can hence be detrimental to the wind turbine. Several techniques are currently being investigated for the purpose of controlling the loads on the blades. They are better understood considering the general equation of the lift experienced by a wind turbine blade.

$$L = \int_0^b \frac{1}{2}\rho[C_{L\alpha}(\theta_{pitch})V_{wind}^2 + (2\pi nr)^2 c]dr \tag{1.2}$$

With: b the blade lenght, θ_{pitch} the blade incidence angle, V_{wind} the wind speed, n the rotor speed and c the chord of the blade. From this equation, four control strategies can be pointed out:

- Pitch Control and Stall Control
- Variable Speed Rotor
- Variable Blade Length
- Blade Section Aerodynamic Optimization

1.4.1 Pitch Control and Stall Control

The over working wind turbine can be controlled by adjusting the blade pitch angle, which in turn reduces the angle of attack, so that the loading and thus the power output is limited. This can be achieved by either employ a mechanical device which changes the pitch by balancing the excessive centrifugal force, or use electronic controller to alter the pitch angle according to measured power output [1].

Regarding stall control, in contrast with pitch control methods, wind turbine blades are designed to exhibit an increase in angle of attack once the critical overload point is reached. The rise of incidence stalls the blade by creating flow to separate from the suction surface to become turbulent, which consequently reduces the lift and thus the rotational speed of the blades. Similarly, two approaches are possible to achieve this. Passive stall control depends on the aerodynamic and structural dynamic design of the wind turbine blades to ensure the angle of attack reaches stall condition when

wind speed exceeds a safe limit. It usually comes with twisted blades along its span to produce a gradual stall and avoid sudden change of load. The advantage of passive stall control is the exclusion of moving parts, which decreases the possibility of component failure.

The other approach is to control the stall of wind turbines actively. This method is very much similar to pitch power control, except that the electronic controller increases instead of decreases the angle of attack to create stall. Compared with the passive method, active stall controlled wind turbines are generally able to maintain their rated power at high wind speeds without a significant drop [1].

1.4.2 Variable Blade Length

The idea is the implementation of an extendable tip blade out of a root blade, in order to increase the diameter in case of low wind speed to maximize the energy production and decrease the diameter in high wind speed conditions to alleviate the loads on the turbine [25]. Results of experiments showed a potential increase in power generation up to 50%, but increase in extreme and fatigue loads in low wind speed conditions [55]. This concept is presented in figure 1.4.2.

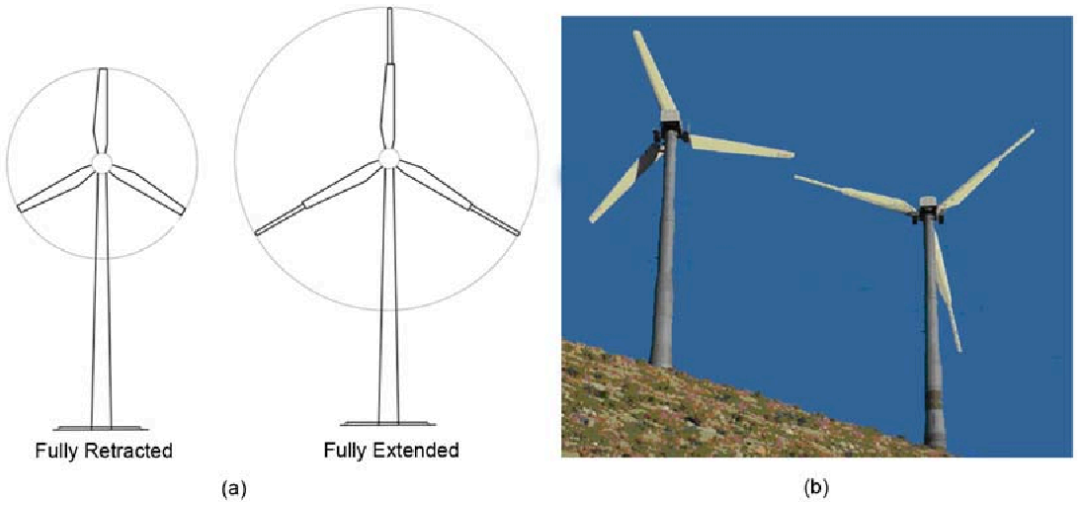

Figure 1.4.2: Variable blade length concept

1.4.3 Aerodynamic Optimization

As previously mentioned, the purpose of this project is to control the loads on the blades by means of Active Flow Control (AFC) devices. The term ”active” implies the use of actuators and sensors along with integrated control theory able to adapt to any change in the flow conditions that can have negative impact on the blades [25].
Figure 1.4.3 shows different passive/active devices on which experimental or numerical researches have been conducted. It is worth noticing that, even if some of this devices showed promising results, none of them have been tested on full-scale wind farms [25]. Moreover, not all of them have been investigated for wind turbines specifically, but for other related fields (i.e. aeronautic/aerospace).

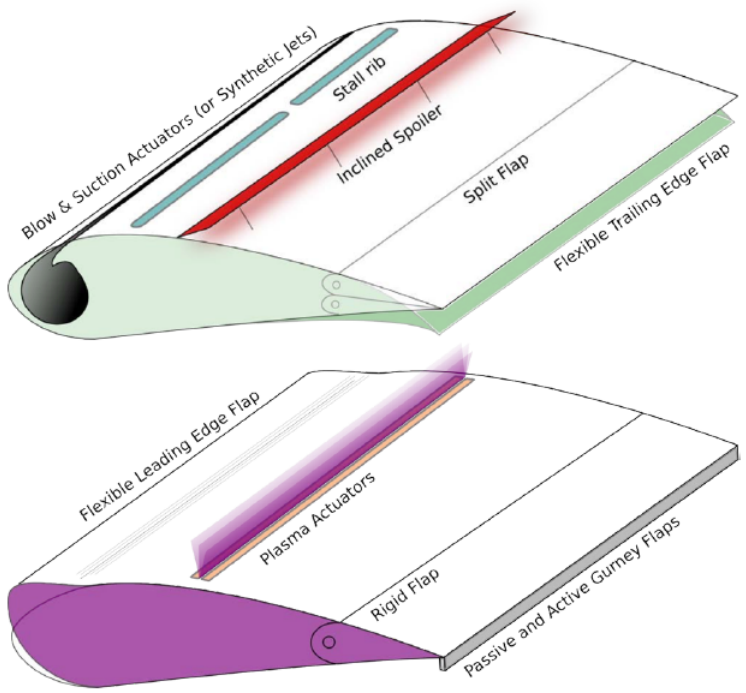

Figure 1.4.3: Schematic representation of existing AFC devices

Trailing Edge Flap

This is probably the most promising AFC device thanks to its proven success in aircraft control and its principle is exactly the same, which is described in Figure 1.4.4: deflection of the flap to the pressure surface generates an increase in aerodynamic load, while a deflection to the suction surface decreases the aerodynamic load [25].

The implementation of the T.E. flap on wind turbines is the subject of numerous investigations with emphasis on load alleviation purpose [2] [6], even if there has been some interest also to rotor stall [51]. Thanks to wind tunnel measurements, Pechlivanoglou and al. [51] proved the T.E. flap to have a significant lift variation potential which may even eliminate the need for pitch systems. They also conducted a parametric study to assess the optimal flap position and length and found out that the optimal configuration leads to a load reduction potential characterized as the root bending moment of 52%. Moreover, Buhl and al. [16] showed that a T.E flap can be suitable when it comes to deal with the unsteady loads as well. Using a 2D model, they found indeed that when a blade experiences a wind step of 10 to 12 m/s the standard variation of the lift can be reduced of up to 95% and in case of a turbulent wind field, the reduction can be of 81%. However, different studies conducted on the T.E. flap might prevent it from being installed on commercial wind turbine in the near future due to the complexity of its linkage with the remaining part of the blade, its expected slow response and noise that the gap between the main blade and the flap might generate.

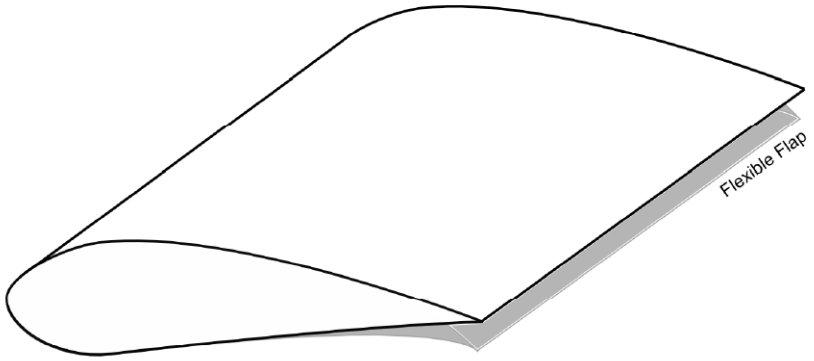

Figure 1.4.4: Flexible trailing edge flap

Leading Edge Flap

The leading leading edge flap (L.E. flap) works the same way as the flexible T.E. flap, except that it is fixed on the leading edge of the blade, as it is shown in figure 1.4.5. Some concepts have been suggested, but the development of the L.E. flap is far from being as active as for the T.E. flap.

Nevertheless, Pechlivanoglou and al. [51] did test this solution in a wind tunnel and the effect on the lift is interesting: the lift variation at very high or very low angle of attack α is negligible. The control influence of this AFC solution is thus generally limited to the near-stall region which could make it a suitable candidate for active stall control.

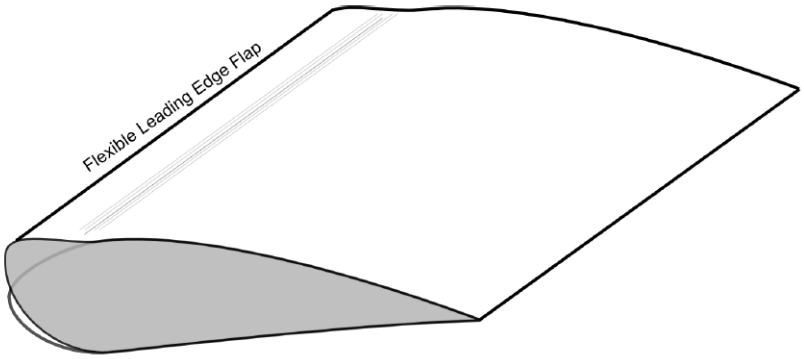

Figure 1.4.5: Flexible leading edge flap

Active Gurney Flap

This device consists of a simple flat plate (on the order of 1% of the chord length) as shown in Figure 1.4.6. Different investigations reveal promising results: Van Dam and al. [50] showed that it is suitable for load alleviation and it has been confirmed by the results obtained in their wind tunnel by Pechlivanoglou and al. [51]. The reduction of the root bending moment value reaches 35.8%. Nevertheless, they also showed that these results were obtained with a constant high deflection of the Gurney Flap contrary to the T.E. flap, which means the control authority of the Gurney Flap is much more limited than the T.E flap. This is due to the small size of this device.

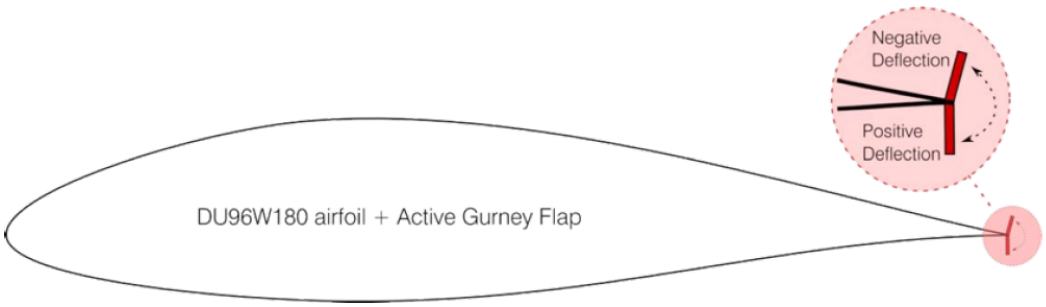

Figure 1.4.6: Active Gurney flap

Chapter 2

Experiments and Literature Review

2.1 Experimental Testing for Wind Turbines

The experimental reference test case was chosen to be the Unsteady Aerodynamics Experiment of wind turbines conducted by the U.S. National Renewable Energy Laboratory, which was comprehensively staged and has a well recorded database stored in the International Energy Agency Annex programmes [40]. The founding component of the turbine blades exclusively used in this experiment was the S809 airfoil designed by NREL and Airfoil Inc.

NREL UAE Phase VI

The U.S. Department of Energy's National Renewable Energy Laboratory (NREL) conducted the Unsteady Aerodynamics Experiment (UAE) testing wind turbines in the world's largest wind tunnel (24.4×36.6 m or 80×120 ft), of that time, located at NASA-Ames Research Centre in Silicon Valley, California [68]. The testing was completed in May 2000 and provided data for more than 1,700 different turbine test conditions. The test consisted of 6 phases investigating 6 different wind turbines, where Phase II-V were detailed in the IEA Annex XIV project and Phase VI is most studied by authors all over the world.

The Phase VI experiment was carried out on a two bladed, tapered and twisted 10 m diameter turbine inside the wind tunnel with thoroughly controlled inflow conditions, which marks the first time in history of comprehensive in door testing of large wind

turbines [15]. The advantages of wind tunnel tests over field tests being more reliable and accurate due to minimisation of inflow turbulence make the NREL Phase VI testing more suitable as a study case. A ”blind comparison” was staged after the completion of the wind tunnel testing in which worldwide wind turbine experts and institutes were invited to predict the NREL wind turbine behaviour, either with the help of Blade Element Momentum (BEM) method or CFD.

DUT wind tunnel testing of NREL S809 airfoil

The S809 airfoil was originally designed by Griffin [31] from Airfoils Incorporated under the supervision of NREL in 1989. The purpose of designing this thick airfoil was specifically for horizontal axis wind turbine applications, which was very different from the designs of National Advisory Committee for Aeronautics (NACA) and National Aeronautics and Space Administration (NASA) airfoils. Restrained maximum lift, insensitive to roughness and low profile drag were the design objectives and had been successfully achieved. Experimental verification was carried out in the low turbulence wind tunnel of the Delft University of Technology (DUT) low speed laboratory, the Netherlands. The testing was conducted at various Reynolds number ranging from 1,000,000 to 3,000,000 and the effect of hysteresis was investigated. Comparison between prior theoretical calculations and experimental results showed good agreement.

OSU wind tunnel testing of NREL S809 airfoil

The Ohio State University (OSU) of the United States was contracted by National Renewable Energy Laboratory (NREL) to conduct a wind tunnel test programme to assess the performance of NREL wind turbine airfoils [59], among which the S809 airfoil is the most recognised one due to NREL’s Unsteady Aerodynamics Experiment Phase II-VI. Steady and unsteady angles of attack were tested during the experiments.

2.2 Literature Review of Previous Work

A significant amount of work has been done by worldwide authors to study the accuracy of CFD codes in predicting the aerodynamic behaviour of air flow at various speeds over the NREL Phase VI two-bladed 10m diameter wind turbine [5] [58] [60] [70]. Moreover, studies of wind turbine aeroelasticity are also reviewed [35] [76].

2.2.1 Aerodynamics of Wind Turbine

Traditionally, due to relatively low tip flow speed in earlier wind turbine studies, CFD works were performed primarily with incompressible solvers such as widely used code EllipSys3D developed in cooperation between Technical University of Denmark (DTU) and Risø National Laboratory [5] and CFD-ACE solver developed by ESI Group which was used by Wolfe and Ochs to study the S809 airfoil [79]. However, as the size of wind turbines increase, the compressibility effects need to be accounted for at near blade tip regions. Thus, studies using compressible codes were also carried out by many researchers, including OVERFLOW developed by Buning et al at NASA [20].

The grid construction was generally achieved using multi blocks structured mesh among the literature, with sizes ranging from 1 to 12 million cells [30]. Most authors considered only the isolated rotor [21] [30], however, some also investigated the interactions between the tower and blades by modelling the whole assembly with a tower [26] [81]. There are also studies about the effects of the wind tunnel walls on the turbine performance, and specific concentration on aeroacoustic problems relating the tip vortex region or the influence of root section [3].

2.2.2 Aeroelasticity of Wind Turbine

The current aeroelasticity design issues relating to wind turbines are well presented and analysed in the overview paper by Madsen and Hansen [35] from Risø national laboratory for sustainable energy of Technical University of Denmark (DTU), which is the world leading wind energy research group. Some other overview papers of wind turbine aeroelasticity published by researchers including Sepahy et al. [65] and Vermeer et al. [76], besides Madsen and Hansen, were also reviewed.

Load concerns

Evolving from the old NACA type general airfoils, the current wind turbine blade designs usually adopt specific tailored characteristics for particular application. This involves various design parameters such as design lift, drag and noise characteristics as well as structural stiffness. Robustness against varying load conditions is now becoming more and more important as wind turbines becomes bigger and more flexible. The load induced on wind turbine rotors mainly comes from the aerodynamic forcing of the incoming free stream wind. However, other site parameters including turbulent wake generated loads for turbines within wind farms and also the controller load. This can be the unsteady loading on the blades when they are travelling through turbulent eddies caused by the wake flow of other turbines, or the bending load on the tower induced by the thrust on the turbine rotor. Even though the tower bending mode by thrust along the wind flow is usually damped out by the structure at low wind load, the bending mode perpendicular to the flow direction is generally left undamped or lowly damped resulting in possible fatigue failure. Therefore, simulation of wind turbine load conditions plays an important role in the design stage with the key tool to solve it being aeroelastic analysis.

For the past decade, aeroelastic codes were developed and tested all over the world. Among them, the most developed and widely used codes are HAWC2 from Risø DTU [43], BLADED by the world's largest renewable energy consultancy GL Garrad Hassan [13] and FLEX4 by Stig Øye [53]. Multi body finite element method is used in HAWC2, while the latter two codes are based on modal form computations. It is very worth noting that all three aforementioned aeroelastic codes utilise BEM theory to simulate aerodynamic performance, which holds some disadvantages when compared with CFD codes.

Modes of Instability

The main objective of aeroelastic analysis is to capture the possible occurrence of aeroelastic instability, which was detailed explained in the U.S. National Renewable Energy Laboratory (NREL) research paper [11] and Hansen's paper [38].
The aeroelastic instability originates from the unstable behaviour of wind turbine modal dynamics, where two common types of instabilities are classical flutter and stall induced vibration, or stall flutter. Classical flutter can be initiated by coupling

of several structural modes when flow is still attached. Once the rotor blade is stalled, even the normally stable modes like flapping mode could become negatively damped leading to stall flutter. Knowing the modal dynamic behaviour of a general wind turbine that how the lower order modes can be involved in aeroelastic response, specific aeroelastic flutter motions need to be studied, which will be further explained in the next chapter.

Stall flutter is able to take place when the turbine blade is stalled, where the air flow is separated from the blade surface causing fluctuation of aerodynamic forces. Almost any type of vibration mode will be susceptible once stalled, especially for blades designed with abrupt stall characteristics airfoils. The stall induced vibration can be compensated by structural damping, but normally by a very limited amount. This was further proved by the researches on aerodynamic stall flutter of wind turbines by many authors [12] [23] [36] [38] [56] [57] [61] [62] [73]. On the other hand, classical flutter can be initiated without the separation of flow but coupling of the first torsional and flapwise bending modes. This flutter motion begins with a torsional deformation leading to unfavourable phased force with flapwise bending, leading to highly negative damping and thus instability. Researches on isolated blade flutter by Lobitz [44] [45] had showed that unsteady computations result in higher flutter speed predictions compared with quasi steady calculations caused by the decrease of the lift slope. Also, as rotor gets bigger, the first torsional mode can couple with the second flapwise mode to produce flutter. Moreover, studies of full turbine assembly flutter [37] also proved Lobitz's theory about larger bladed turbines stating that the aeroelastic damping will be decreased with smaller natural frequency ratio between the two coupled modes.

Despite various studies and conclusions made on wind turbine aeroelasticity, there are still a lot of researches undergoing currently, including stall induced vibrations at standstill, dynamic stall, structural damping enhancement, flutter limits for yawed flow and non linear coupling flutter.

2.2.3 Smart Rotors and Loads Control for Wind Turbines

This part is focused on available literature and research of interest for smart rotor applications and progress related to wind turbine applications. Although the amount of available progress in this specific field is quite new and can not be compared to the available progress in rotor-craft, inspired by these similar applications and by the need for more advanced active control, research programs investigate the possibilities for such concepts in wind turbines.

DUWIND (TU Delft)

An important research work, concerning feasibility studies on smart dynamic rotor control for wind turbine applications, has been conducted by Marrant, van Holten and Kuik for the STW project ”Smart Dynamic Rotor Control for Large Offshore Wind Turbines”.

The first report [47] deals with the inventory of rotor design options and possible load reductions. The fluctuating loads on a wind turbine are described and possibilities of influencing fatigue loads or structural loads are discussed. Active rotor control concepts are presented, which include pitch control concepts (collective, cyclic, higher harmonic), individual blade control (part-span pitch, aileron control, active twist) and active damping of blade and tower vibrations. Also semi-active and passive control options are discussed (passive tips, self-twisting blades, compliant blades). Concluding, individual pitch control was considered as the most powerful strategy (because of the ability to reduce aerodynamic loads both due to temporal and spatial variances in inflow), but active structural damping was also considered interesting (for reducing the loads due to axial tower mode and blade flapwise bending mode).

The second report [48] summarizes present techniques with regard to sensors, actuators, aerodynamic constructions and control strategies and their application on large offshore pitch regulated variable-speed wind turbines. Regarding sensors, strain gauges, accelerometers and force sensors were analyzed. Piezoelectric force sensors at the blade root were considered a feasible solution for the measurement of aerodynamic loads. Optical fibers were considered expensive and not well established for measuring strains on blades. Passive accelerometers were considered a good solution due to their low bandwidth and low frequency limit.

Regarding control strategies, four control strategies that had been developed to actively suppress vibrations in rotorcraft are analyzed: a feed forward adaptive control algorithm (Broadband filtered X-LMS and tonal control), a Fourier synthesis algorithm, a real-time adaptive neural network controller and an iterative learning controller. Some important considerations regarding the connection between controller design and wind turbine design are also pointed out. Regarding actuators, many categories are analyzed: conventional (pneumatic, hydraulic, electro-motors), smart materials (electrorheological, magnetorheological, shape memory alloys (SMA), electrostrictive, piezoelectric, magnetostrictive).

The third report [49] summarizes theoretical and software tools, which are necessary for the design of a smart rotor. Also hardware for testing of a smart rotor is mentioned. It is assumed that existing quasi-steady BEM models are not enough for smart rotor applications, vortex methods may be more reliable and unsteady aerodynamics are very important for the simulation of the fluctuating inflow and loads. It is also stated that new reliable dynamic models for smart materials and control algorithms must be incorporated. Regarding software tools, WOBBE is mentioned for stability calculations, and PHATAS/FOCUS, DAWIDUM and ADAMS for load calculations. For controller requirements, a PC with Matlab/dSPACE is necessary. Concerning hardware and testing, mainly wind tunnel and laboratory requirements are discussed.

An interesting first approach to the application of active control on wind turbine blades was that of Aguirre at the TU Delft [52]. A blade section with a trailing edge flap was used for the wind tunnel experiment. Strain gauges were implemented for measuring the lift change on the blade, potentiometers for measuring the pitch angle and the flap angle and servomotors as actuators for changing the pitch angle and the flap angle. The experimental procedure was based on the idea of changing the pitch angle of the blade and then, using a real time controller, activating the flap in order to reduce the changes in lift. Steady measurements were firstly performed for different angles of attack and flap. Unfortunately no model could be build because of the disturbances in the signals. This experiment was a good simple approach to use active control on a blade and showed the challenges and requirements for such efforts.

ADAPWING (RISØ)

A very important contribution to the research about smart rotor control for wind turbines is made by the wind energy research group of Risø, the National Laboratory in Denmark. Through the project Adapwing (Adaptive wing geometry for reduction of wind turbine loads), the possibilities of eliminating the fast fluctuating loads on wind turbines as a consequence of the turbulence in the wind and the tower shadow through the use of adaptive wing geometry regulation are being investigated. By cooperation between researchers and students from DTU many interesting reports have been presented.

All cover computational studies on variable geometry airfoils using aero-servo-elastic models. Firstly, in the MSc thesis of Basualdo, a two-dimensional model is developed [8]. The aerodynamics is described using "Thin Airfoil Theory" for attached, irrotational, incompressible flow and solved numerically using a Panel Method for steady and unsteady situations. The structural model consists of two degrees of freedom (edgewise, flapwise), expressed by spring and damper models. For control, a simple control algorithm is used, with a target control strategy to minimize the tip deflection variation of the blade. The results show the potential of such a control. The standard deviation of the airfoil displacements has been reduced to 25% of the value corresponding to no control, during the 2 sec simulations. In all the other simulations (e.g. 100 sec, gust) the decrease in the displacement amplitudes is evident. But, it must be pointed out that the model consists of a simple control simulation, not taking into account any delays caused by aerodynamics, actuator performance or noise.

In the work of Troldborg, as for his MSc thesis, a 2D computational study is being performed [74]. The aerodynamic characteristics of the Risø-B1-18 airfoil equipped with different compliant trailing edge flaps are calculated. The solver used was Ellipsys2D (in-house RANS code) with a k-ω SST turbulence model for fully turbulent flow, at Re=1.6 million. The calculations on the baseline airfoil were compared with experimental data and showed perfect agreement. A comparison with the potential theory solver developed by Gaunna [29] is also made. The influence of various key parameters such as flap shape, flap size, and oscillating frequencies was investigated so that an optimum design is suggested: a moderately curved flap with flap chord to airfoil curve ratio between 0, 5 and 0, 10. Finally a study was conducted on an oscillating

airfoil fitted with an oscillating flap, with the objective to prescribe the motion of the flap so that the lift remained constant.

Through the project Adapwing, as have been mentioned previously, computational studies were performed in order to find general design directions for deformable controllable airfoil geometry. The choice, as can been seen through the computational studies, was deformable trailing edge flaps. An experimental setup for wind tunnel tests was prepared. The actuator/control surface chosen was a piezoceramic uniform bender actuator (Thunder TH-6R). So, no discrete servo or hinge flap was used but just a piezo-bender device which serves as both a flap and actuator. The flap had 10% chord length and could operate with deflection between -5 and +5 degrees. Firstly, the actuator performance was measured [19]. Through static and dynamic tests, the deflections of the bender were studied at various voltage inputs. An important result was that the actuator response showed a clear hysteresis loop. Optimal voltage operation regions were found. A blade section was constructed base on the Risø-B1-18 Airfoil. A number of Thunder actuators were glued to the trailing edge. Static and dynamic measurements were performed studying the pitch change and flap change and their behaviour together at different frequencies of operation. No active controller was implemented. Unfortunately, there are no official publications available regarding this experiment yet.

All important results from the computational work in Adapwing have been included in a series of publications [8] [17] [18] [74].

Chapter 3

Aerodynamics and Aeroelasticy

3.1 Fundamental Dimensionless Quantities

Reynolds Number (Re)

In fluid dynamics, the Reynolds number characterises the ratio of inertia to viscous forces and is defined as

$$Re = \frac{inertia forces}{viscous forces} = \frac{\rho U^2/L}{\mu U/L^2} = \frac{\rho U L}{\mu} \tag{3.1}$$

The terms ρ, U and μ are the density, velocity and dynamic viscosity of the fluid and L is the characteristic length, usually taken as the chord length for an airfoil. The Reynolds number is a dimensionless number which determines the flow regime of the system, i.e. laminar or turbulent. Low Reynolds number indicates a dominance of viscous forces in the flow and hence the flow is generally considered to be steady, smooth and laminar. Turbulence is present at an high Reynolds number where the flow is dominated by inertia forces with the appearance of eddies and vortices. Simulation of models can be carried out providing that dynamic similarity is met between the model and the real case, which implies a same Reynolds number.

Mach Number (M)

For an object in air flow, the Mach number is the ratio of its relative moving velocity to the speed of sound and is in the form of

$$M = \frac{U}{a} \tag{3.2}$$

where U is the relative speed and a is the environmental sound speed. Analyses based on Mach number are usually found in researches of high speed fluid flow such as gas turbine or flying airplane, where M is close to unity and phenomena like choking or shock wave may take place. The relative air flow speed around a wind turbine blade is generally very low compared with the sound speed so that Mach number is only used as a non dimensional form of the flow velocity.

Pressure Coefficient (Cp)

The pressure coefficient is a non dimensional value of local pressure

$$Cp = \frac{P - P_\infty}{\frac{1}{2}\rho U_\infty^2} \tag{3.3}$$

where P is the local pressure, P_∞ is the freestream pressure, ρ is the fluid density and U_∞ is the free stream velocity. Pressure coefficient is widely used for analyses of pressure distribution around airfoils of aircraft wings or wind turbine blades, where pressure is normalised for easier comparison to assess the computation performance and to compute other aerodynamic force coefficients.

Drag Coefficient (Cd)

The dimensionless quantity of drag force, which is the opposing force acting on an object in a fluid flow, is used to measure its resistance in air environment and is defined as

$$C_d = \frac{Drag\ Force}{Reference\ Force} = \frac{F_{drag}}{\frac{1}{2}\rho U^2 A} \tag{3.4}$$

where F_{drag} is the drag force, ρ is the fluid density, U is the relative velocity between the object and the fluid, and A is the reference area which is usually replaced by the chord length *c* to give a sectional drag coefficient.

The drag force is consisted of both pressure drag and shear drag due to skin friction. Pressure drag is created by the pressure difference between the airfoil surfaces, caused by the acceleration of flow on the suction side. Skin friction denotes the shear of air on blade surfaces along air flow direction, which is commonly approximated with respective to local Reynolds number in turbulent boundary layer by the "1/7 Power Law" derived by Theodore von Kármán as $c_f = 0.0576 Re_x^{1/5}$ for $5 \cdot 10^5 < Re_x < 10^7$. The two components of drag can be calculated using

$$\text{Pressure Drag} = \sum P_i A_i n_i \cdot k \tag{3.5}$$

$$\text{Frictional Drag} = \sum C_{f,i} A_i \frac{1}{2} \rho_i U_i \cdot k \tag{3.6}$$

where *i*, *P*, *A*, *n*, ρ, *U* and C_f are the number, pressure, area, unit normal, density, relative velocity and skin friction coefficient of the local grid element respectively; **k** is the unit vector in the direction of drag, i.e. free stream flow direction. Thus, the front of a blade will receive high pressure drag and the attached flow surfaces will contribute most of the skin friction.

Lift Coefficient (Cl)

Similar to drag coefficient, the lift coefficient is also a non-dimensional value and is defined with the same formula

$$C_l = \frac{Lift\ Force}{Reference\ Force} = \frac{F_{lift}}{\frac{1}{2}\rho U^2 A} \tag{3.7}$$

The reference area A for lift coefficient calculation is usually the same as the one used for drag coefficient , which is the chord projection area. The lift force can be evaluated as

$$\text{Lift Force} = \sum P_i A_i n_i \cdot k \tag{3.8}$$

where the unit vector **k** of lift is perpendicular to free stream velocity. Lift coefficient is generally more important compared with drag coefficient for airfoils, mainly because the amount of lift induced determines the power output of a wind turbine or the upward force of an airplane.

Pitching Moment Coefficient (Cm)

The pitching moment coefficient is also an important parameter in determining both the performance and the stability of an airfoil or a wind turbine blade. It is defined as

$$C_m = \sum_{i=1}^{n} \{(\frac{p_i + p_{i+1}}{2})[(x_{i+1} - x_i)(\frac{x_i + x_{i+1}}{2} - 0.25) + (y_{i+1} - y_i)(\frac{y_i + y_{i+1}}{2}]\} \quad (3.9)$$

where x and y are grid coordinates and the moment is usually calculated about 0.25 chord.

3.2 Blade as Airfoil

The general design of a wind turbine blade usually contains two main components: the outer aerodynamic shell for performance and inner main spar for maximum stiffness at a relatively low structural weight. An example of wind turbine blade cross section design is shown below in Figure 2.2.1

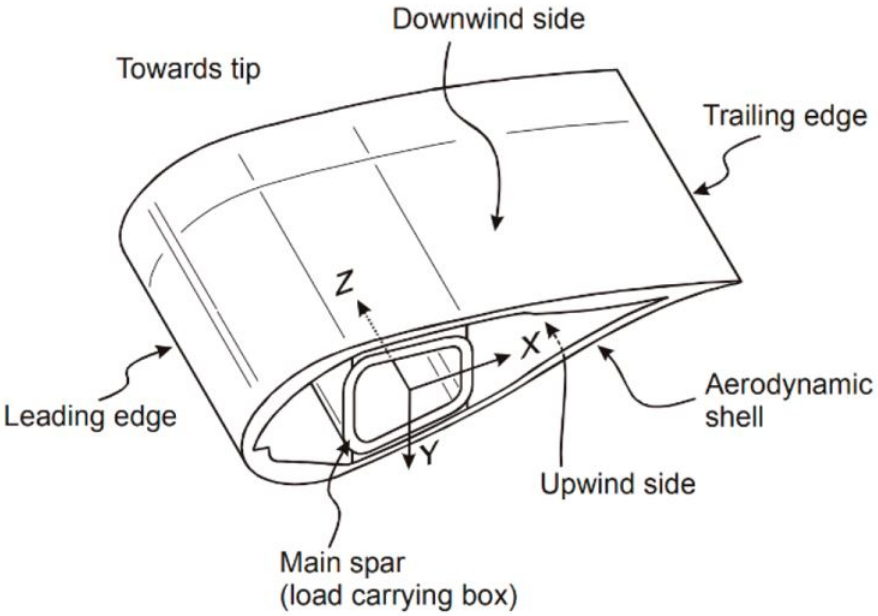

Figure 3.2.1: Cross section of a modern wind turbine blade

The outer shell of a turbine blade is normally manufactured using low density synthetic fibre composites, while the inner load carrying D-spar is usually made of carbon-fibre plastic composites, which has an extremely high strength to weight ratio in order to ensure both high bending and torsional stiffness [68].

For a general airplane wing airfoil, the leading edge can be recognised as the very front point facing the incoming flow, and the trailing edge at the very end. The line connecting the leading and trailing edges is defined as the chord line and the camber line is just a geometrical term to express the curvature of the airfoil.

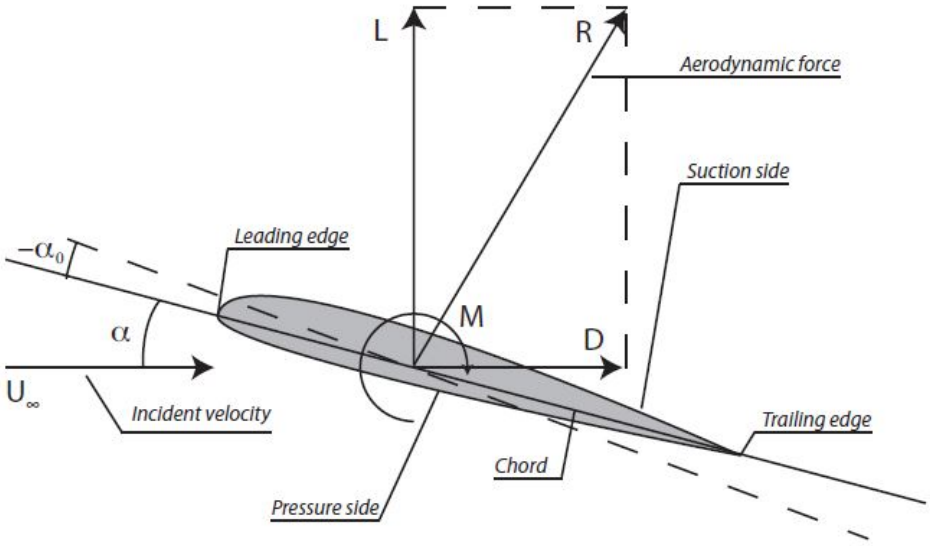

Figure 3.2.2: Schematic of an airfoil

Similar to aircraft wings, wind turbine airfoils also possess aerodynamic characteristics such as lift perpendicular to incoming wind direction and pressure drag along the wind direction. A sketch of the general characteristics of a generic airfoil is shown above in Figure 3.2.2. Wind turbine airfoils differ from aircraft wings since they have to rotate about an axis, making the actual angle of attack dependent on the rotational speed.

The generation of aerodynamic forces is closely related to the pressure field around the airfoil in airflow. As flow approaches the airfoil, it is directed to form a faster stream on the upper surface than the lower surface. According to Bernoulli's equation, faster flow speed corresponds to lower pressure. Thus the pressure on the upper surface will be lower than that on the lower surface, leading to an overall upward lifting force.
A drag force is also created by the shear stress of the flow on the surface and pressure

difference of the front and back of the blade. Therefore a good designed airfoil normally has an optimised compromise of these characteristics.

3.3 Boundary Layer Theory

In fluid dynamics, boundary layer, represents a thin region very close to the body surface in the flow path where the skin friction induced by the surface interferes with the flow [10].

3.3.1 Concept of Boundary Layer

Outside of the layer, due to negligible effects of the viscous friction, flow is recognised as inviscid, governing by potential theory where flow speed is more or less constant at any position. Within the boundary layer, the flow adheres to the surface, getting slowed down. Right on top of the surface, fluid stays relatively stationary which is referred to as the no slip condition.

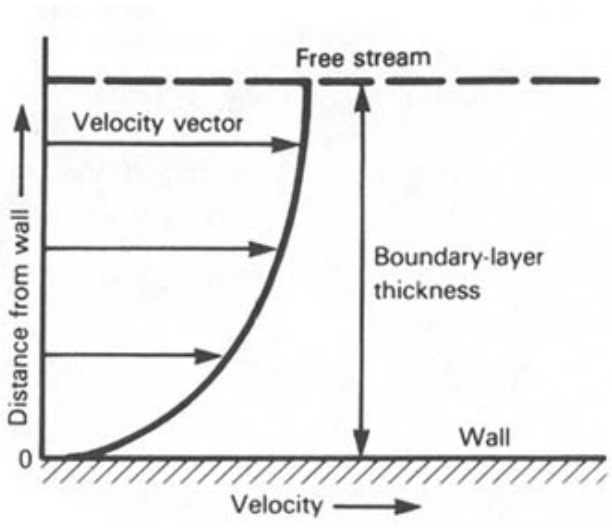

Figure 3.3.1: Profile of a typical boundary layer

The interaction between the fluid and the surface consequently produces a so called wall friction, or wall shear stress τ_w [10] expressed as

$$\tau_w = \mu \frac{\partial \mu}{\partial y}|_w \tag{3.10}$$

where μ is the viscosity of the fluid, $\frac{\partial \mu}{\partial y}|_w$ states the velocity gradient normal to the surface.

It is now clear that the fluid closer to the surface will be more affected due to a much larger velocity gradient as shown in Figure 2.3.1 above , while in the outside inviscid region the wall shear stress is negligible since the velocity difference is very small. This viscous wall shear stress within the boundary layer eventually results in the globally known skin friction drag.

The thickness of the boundary layer can be determined as the distance δ between the surface and the point where the fluid speed has reached 99% of the free stream velocity. It depends on the distance that the fluid has travelled from the leading edge of the surface, and also the viscosity of the fluid where higher viscosity usually leads to thicker boundary layer. It is worth noting that for very high viscosity, or small Reynolds number, the thin layer approach of the boundary layer theory is no longer valid.

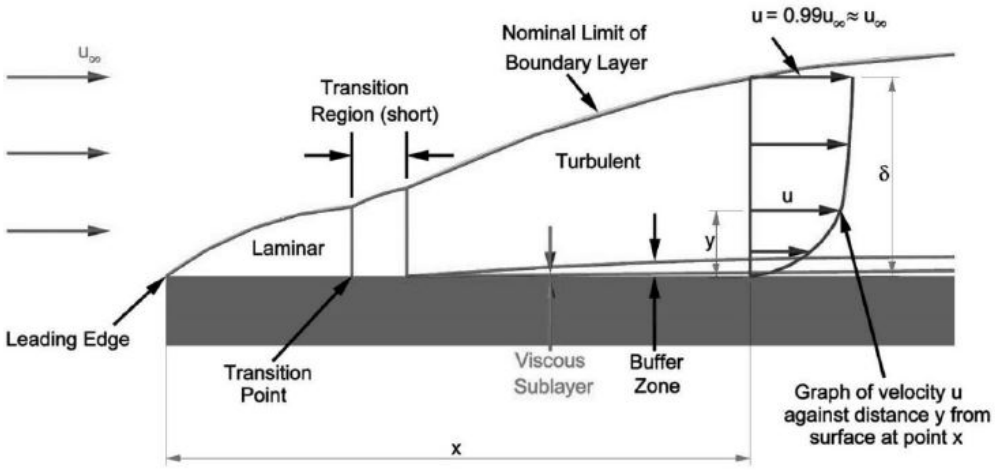

Figure 3.3.2: Boundary layer on a flat plate

As shown above in Figure 3.3.2, boundary layer can be categorised into three main sections, namely laminar, transition and turbulent. Similar to flow regimes, the types of boundary layer also depends on the Reynolds number. However instead, a local Reynolds number Re_x [10] is considered, which is expressed as

$$Re_x = \frac{\rho U x}{\mu} \tag{3.11}$$

where symbols have their usual meanings except that the length scale is taken to be the distance x advanced from the leading edge.

The transition region exists in between the laminar and turbulent boundary layers, it is usually very short and corresponds to a certain critical local Reynolds number Re_x^{crit}. Below this value, the boundary layer is laminar where layers of constant velocity flow are present. Above this value, fluctuation motions can be identified in the turbulent boundary layer. Since the local Reynolds number increases as the flow advances, the boundary layer transforms from laminar to turbulent.

3.3.2 Flow separation and Airfoil Stall

One of the most important limiting factor of the performance of an airfoil is stall, which is closely related to flow separation. As flow separation starts inside the boundary layer, it is of great importance for this study.

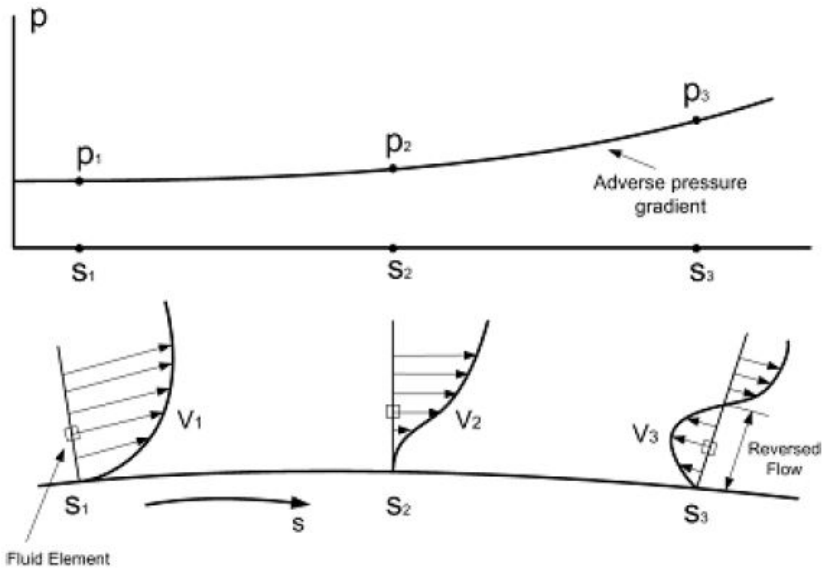

Figure 3.3.3: Flow separation schematics

Flow separation occurs when boundary layer gets detached from the surface: this is mainly due to the change in pressure field as boundary layer travels along the surface. At an earlier stage, boundary layer experiences favourable positive pressure gradient ($\frac{dp}{dx} < 0$), which exhibits suction effect and keeps the flow attached. When it advances far enough, the kinetic energy of the flow which is reduced due to frictional interaction with the surface can no longer hold against the pressure field in front of the flow, producing an adverse pressure gradient ($\frac{dp}{dx} > 0$) [10]. After travelling in this adverse pressure gradient for a certain distance, the boundary layer may eventually slow down to zero velocity or even leading to reversed flow as shown in figure 3.3.3.

For a typical airfoil at zero incidence, the adverse pressure gradient is usually too small to separate the boundary layer from the surface. Thus the flow is said to be attached and the flow pattern is smooth. With a certain angle of attack, the air stream over the upper (or suction) surface moves faster than that passing underneath (or pressure surface) as shown below on the left of Figure 3.3.4. According to Bernoulli's principle, faster velocity produces lower pressure and vice versa. Therefore as the boundary layer travels through the suction surface towards trailing edge, it will eventually encounter a substantial adverse pressure gradient and may then separate from the surface.

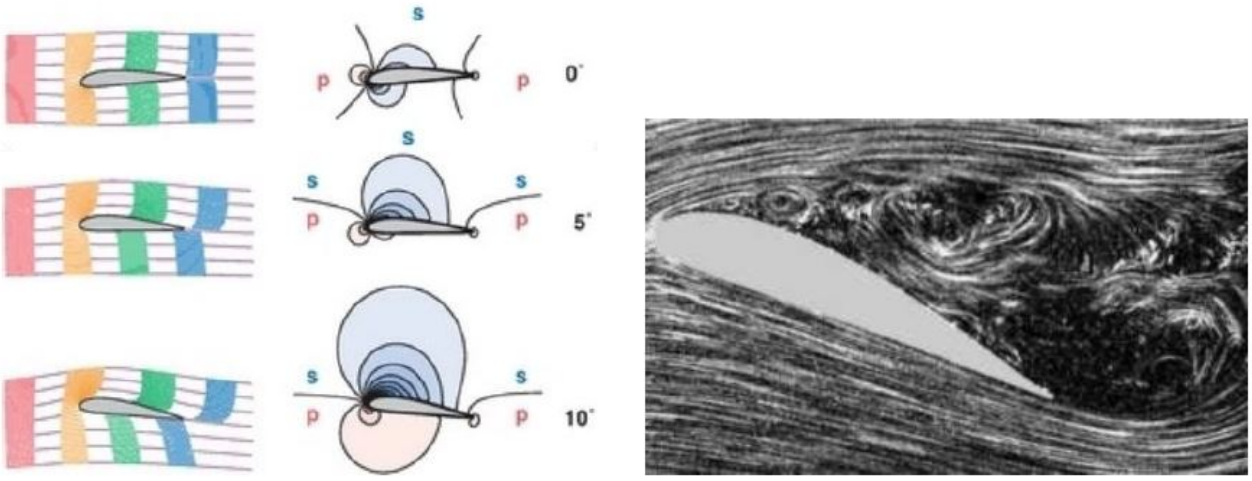

Figure 3.3.4: Airfoil pressure distribution (left) and stall of the airfoil (right)

As the angle of attack increases, the suction effect magnifies causing the flow over the upper surface to be even faster. Thus the pressure will be even lower according to Bernoulli and more energy will be lost in friction due to higher wall shear stress, both resulting in a weaker ability of the boundary layer to advance in the adverse pressure gradient. At a certain point, the flow may stop moving relative to the airfoil or even move back wards to lower pressure zones. The airfoil is said to be stalled at this point shown on the right of Figure 3.3.4 [10].

Accompanying stall, eddies are formed due to the reversed flow, and will eventually contribute to a low pressure wake. Since boundary layer no longer exists after flow separation, the original structure which provides the lift of the airfoil experiences a sudden decrease of upward force. This phenomenon of sudden loss of lift is one of the most important consequences of stall. The other effects include the considerable increase of pressure drag due to a higher pressure difference on both surfaces, and the diminish of frictional drag because of the separation of the viscous boundary layer.

Therefore, avoiding flow separation will maintain a high level of lift and relatively low amount of drag. In spite of many merits of avoiding stall, some passive stall controlled wind turbines still rely on the stall of the turbine blades at a proper time in order to protect them from potential aerodynamic induced vibration damage. However, the stall delay effect (or rotational augmentation) which usually happens with rotor-crafts, could bring problems to operating wind turbines where the rotation is found to have a delaying effect on flow separation. This may potentially damage the wind turbines by allowing excessive loads on blades with delayed stall and is well studied in Breton's thesis [15] and the paper by Schreck et al [64].

3.4 Flutter

Flutter is a dangerous vibration motion of flexible structures, as a result of the interactions among aerodynamic, elastic and inertial forces first defined by Arthur Roderick Collar in 1947. There may exist a point where the structural damping is no longer sufficient to damp out the increasing vibration motion introduced by a change of operating condition like a higher flow speed. This could eventually lead to a catastrophic failure of the structure. There are many types of flutter for blades and the most common two are introduced below.

3.4.1 Classical Flutter

Classical flutter is caused by coupling of modes, which indicates a flutter motion initiated with the interference of blade mode shapes. As shown below in Figure 3.4.1, at the start of a cycle (t=0), the airfoil is displaced with a rotation. This rotation, causing a change in angle of attack, produces extra force that starts lifting the airfoil, while the rotation is recovered to zero by its torsional stiffness (t=T/4). Due to the return of the rotation, the extra lift no longer exists, and the bending stiffness tries to pull the airfoil back to the neutral position with the airfoil rotating in a nose down manner owing to inertia (t=T/2). This series of motions is carried out in a mirrored way with the airfoil plunging down (t=3T/4) instead of rising up, and finally completes a full cycle (t=T). This aerodynamic coupling of the torsional and bending vibration modes of an airfoil is at its worst when the rotation mode leads the plunge mode by 90 degrees [33]. The bending stiffness of the blade and aerodynamic forcing will eventually damp out the plunge motion, however leaving the rotation undamped. The aerodynamic

damping on an airfoil will be explained in depth in the following section. The induced rotational vibration motion cannot be compensated by normal structural damping and may diverge leading to structure failure.

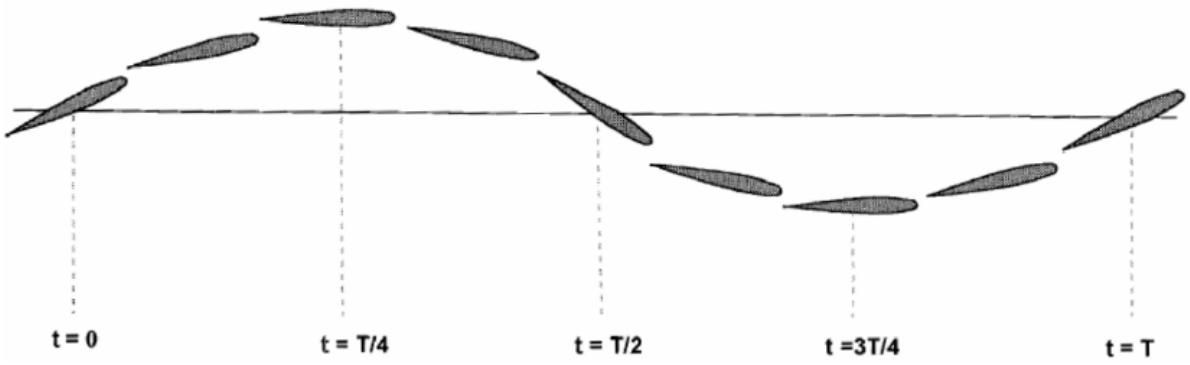

Figure 3.4.1: Rotation and plunge motion for an airfoil experiencing flutter

It is worth noting that the classical flutter is a two degree of freedom motion purely caused by coupling of the first torsional and bending modes in an unfavourable phase, causing large negative aerodynamic damping which cannot be compensated by the mechanical structural damping. There is still no actual report of wind turbine flutter failure, however it happens without the separation of flow from the wind turbine blades which means wind turbines with high tip speeds and long, flexible blades are especially susceptible and thus highly likely to happen in the future.

For a wind turbine to experience classical flutter, the air flow around the blade surface has to be attached, i.e. stall is not reached. Furthermore, the turbine blade must have high aspect ratio to produce large enough tip speed to ensure high energy air flow. The bending and torsional modes' natural frequencies also need to be low enough to be well coupled to produce a flutter mode. Therefore, flutter is more likely to become a problem in pitch controlled wind turbines since their blades are regulated to operate constantly below stall. The risk increases if the wind turbine operates with a higher tip speed, which is normally limited by noise and safety considerations, but could be initiated by highly yawed inflow [24].

3.4.2 Stall Flutter

Unlike the classical flutter that can happen with steady flow, stall flutter is always found with airfoils near or above the stall speeds where flow becomes unsteady. At this point, the airfoils are usually under very high loads and the flow separates during stall. The fluctuation of separated flow and the high loading force lead to a substantial increase of the induced pitching moment, which corresponds to a single degree of freedom torsional mode that may eventually cause flutter [72].
Fortunately, stall flutter can be compensated with a well aerodynamic design and sufficient structural damping, since it is initiated by the separation of flow and it is a single Degree of Freedom (DOF) motion. For wind turbine blades, the occurrence of stall flutter usually comes with abrupt stall characteristics designed airfoil sections and low structural damping . In contrast with classical flutter, stall flutter is a more serious problem for stall regulated wind turbines as the rotor blades are either designed or controlled to operate in stalled conditions to limit the power output, while pitch regulated turbines generally do not operate within this range [24].

3.4.3 Flutter in Airfoils

Individual Modes

In general, flutter of airfoils can be typed into two main categories: aerodynamic induced flutter and mechanical structure flutter, which essentially correspond to stall and classical flutter respectively.

Critical stability, i.e. zero damping, happens at stall when the lift curve gradient decreases to zero where theoretically the airfoil vibration will not be attenuated once started. Beyond this point, the lift force induced on the airfoil begins to drop, corresponding to a negative lift slope. Therefore a negative damping is present at this post stall stage, where the aerodynamic forcing which is supposed to damp out the airfoil motion becomes out of phase, causing an amplification of vibration and hence negative damping effect. Although, as explained in the previous section, the major possibility of stall flutter comes from the simple torsion mode due to sudden rise of airfoil pitching moment after stall, the plunge mode is also highly likely to experience flutter since the fluctuation of lift force is very high.

On the other hand, classical flutter is possible to occur without stalling the airfoil through a mixing of simple structural modes, which in this case are the first plunge and first twist mode. Now, the two modes are considered individually by consulting their schematics shown below in Figure 3.4.2

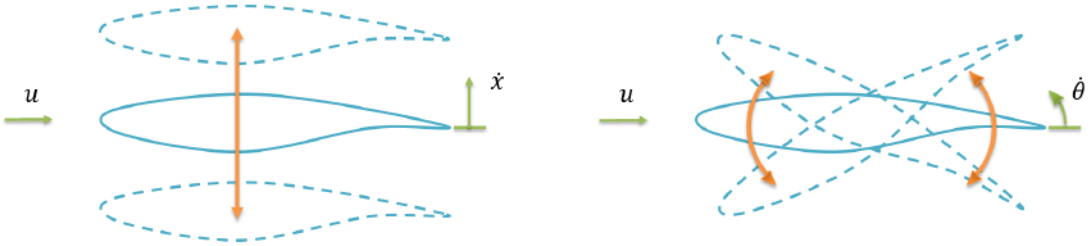

Figure 3.4.2: Schematic of plunge (left) and twist (right) modes of an airfoil

From the energy point of view, a damped system is considered to lose energy to its surrounding air flow while flutter means the system is gaining energy. Thus damping can be related to the work done to the airfoil by the flow, which is

$$\text{Work} = \int_{period} \text{force} \cdot \text{velocity dt} \tag{3.12}$$

where the phase difference between the force and the velocity will determine the sign of the resulting work and thus the system stability. A positive air flow work means a gaining of energy of the airfoil and therefore negative damping leading to instability, and vice versa. The general relationship between the phase difference and the resulting damping can be expressed as follows:

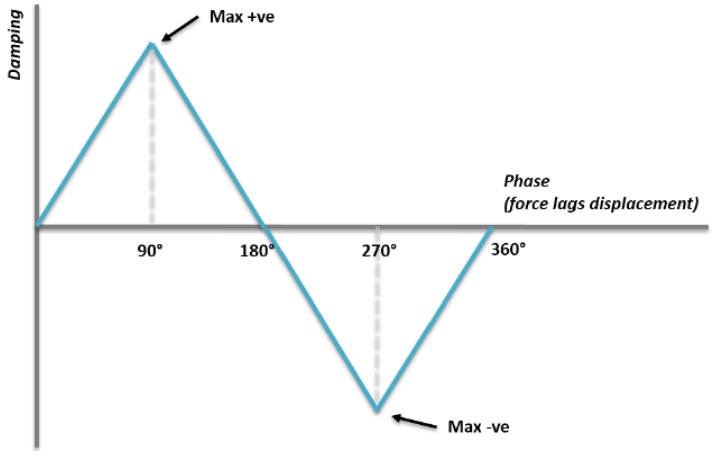

Figure 3.4.3: Schematic of the phasing between force and velocity

A simple schematic of the relationship between damping and force/displacement phase is constructed above in Figure 3.4.3, based on the work integral. Since velocity leads displacement by 90°, so if force is totally in phase or out of phase with displacement, the work will always be an integral of the product of a sine and a cosine which results in zero damping. As force leads displacement, aerodynamic damping will become negative and reach a maximum when the lead is 90° (or lags 270°). Consequently, damping will reach its positive maximum at 90° lagging displacement. Therefore, by analysing the phasing between force and displacement response of a case, the stability can be determined.

For the plunge motion, the lift force created can be treated as proportional to the angle of attack, when the vibration amplitude is small. The additional induced angle of attack due to the airfoil vertical motion can be expressed as $-\frac{\dot{x}}{U}$ where $\dot{x}$ is the plunge velocity and U is the free stream velocity. Thus the lift force can be expressed as

$$\text{Lift Force} \propto -\frac{\dot{x}}{U} \tag{3.13}$$

Based on this relationship, it can be deduced that the real component of the force is in phase with the airfoil velocity $\dot{x}$ but opposite in sign, which creates plunge damping to the system. The imaginary component is in phase with airfoil displacement x with opposite sign, thus generating a plunge stiffening effect causing an increase in the resulting vibration frequency, especially when frequency is low. It also has a potential to destabilise the twist motion by enlarging the pitching moment, according to few researches [72].

The twist motion can be analysed similarly: since the change in angle of attack for an airfoil twisted about its mid chord is just the twist angle θ, it would follow the relation of

$$\text{Lift Force} \propto \theta \tag{3.14}$$

Correspondingly, the real component of the force is totally in phase with θ causing a rotational de-stiffening effect, while the imaginary component is in phase with $\dot{\theta}$, but opposite in sign providing rotational damping [72].

Generally, it is the real component of the force that determines the amount of damping for a vibrating system. Therefore, the plunge motion is damped out eventually and the twist motion will be left undamped, which proves the aero-damping theory of classical flutter introduced in the previous section.

Mixed Modes

However, individual modes are only possible on two dimensional like' objects with unity hub tip ratio, meaning a uniform extension in the third dimension. For a common wind turbine, the rotor blade is usually twisted and tapered, leading to a hub tip ratio smaller than 1. In this case for the NREL Phase VI wind turbine, the ratio between the root and the tip chord length is about 2.06. Therefore, the real vibration mode of a wind turbine blade is always a mix of simple modes.
Despite the individual damping characteristics, the situation becomes very different when the two modes are mixed together. If we let $\bar{\phi}$ stands for mode shape, or the eigenvector of this case, then the mixed mode shape can be expressed as

$$\bar{\phi}_m = \bar{\phi}_P + \bar{\phi}_T \tag{3.15}$$

where $\bar{\phi}_m$, $\bar{\phi}_P$ and $\bar{\phi}_T$ corresponds to the eigenvectors of the mixed, plunge and twist modes respectively and α is the twist to plunge ratio controlling the relative amplitude between plunge and twist motion.

It is known that certain mixing of the two modes would cause the structure to flutter even though none of the two will experience instability by its own. This can be understood as the result of the coupling effect where the stable force induced by one mode motion contributes to the instability of the other mode. Specifically speaking, the aerodynamic force created by plunge mode denoted as F_p is a positive damping force contributing to stability, while the twist mode force F_p is negative in sign leading to instability. Therefore theoretically the blade will flutter if the sum of the two forces becomes negative, i.e.

$$|F_t| > |F_p| \tag{3.16}$$

Based on the above theory, the relation can be further derived as

$$\frac{F_p}{F_t} \propto \frac{k}{\alpha} \tag{3.17}$$

where F_p and F_p stand for the induced aerodynamic forces by these two modes and k is the reduced frequency and is in a form of the Strouhal number. The reduced frequency k is a non dimensionalised frequency term characterising the variation of flow with time defined as

$$k = \frac{fL}{u} \tag{3.18}$$

where f is the cyclic frequency in Hz, L is the reference length taken as the full chord in this study and u is free stream velocity.

It is clear that flutter will become a problem once the frequency is reduced to very low. It is worth noting that this relation only applies to small amplitude motions where a quasi linear relationship between the aerodynamic force and angle of attack is valid. Once the airfoil is stalled, classical flutter by mixing of modes no longer exists and stall flutter will be present.

Chapter 4

2-D Validation & Analysis

4.1 Geometric Model of the S809 Airfoil

The airfoil selected for 2D validation is the S809 airfoil designed specifically for HAWT applications [69]. It has a thickness of 21% chord length which belongs to the NREL thick airfoil family optimised to compete with the widely used NACA-HAWT airfoil series with primary objectives of restrained maximum lift, insensitive to leading edge roughness and low profile drag [69]. A sketch of the S809 airfoil is shown below in Figure 4.1.1 and the detailed S809 airfoil profile characteristics are included in APPENDIX A: S809 Airfoil Profile Coordinates.

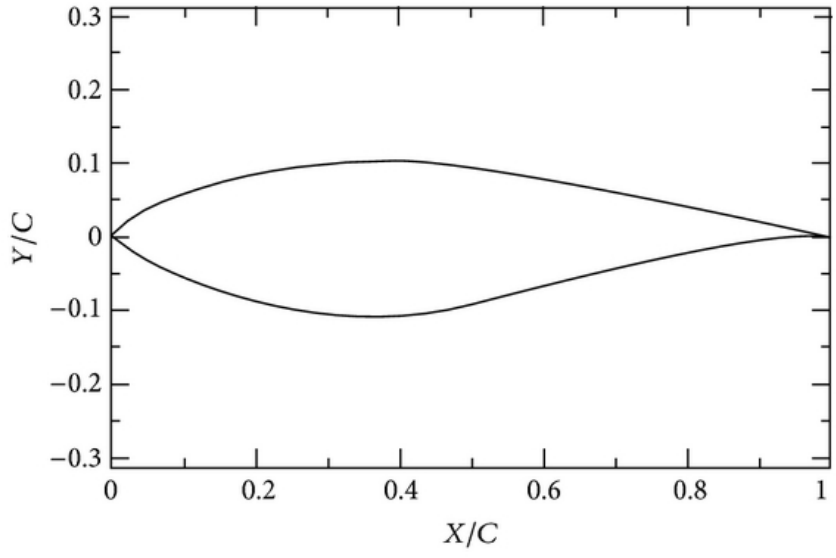

Figure 4.1.1: Schematic of the NREL S809 airfoil

The airfoil section model tested in Netherlands Delft University of Technology (DUT) Low Speed Laboratory has a chord length of 600 mm. The experiments conducted in the low turbulence wind tunnel, which is 1.8 m by 1.25 m, recorded basic, low speed, two dimensional aerodynamic characteristics of the S809 airfoil [79].
A 457 mm constant chord model of the airfoil was further tested by Aeronautical and Astronautical Research Laboratories (AARL) of Ohio State University (OSU), concentrated on the effects of leading edge roughness, which was one of the primary design objective [39]. The experimental wind tunnel data, which includes pressure distributions and aerodynamic force coefficients, was documented in the final reports by Somers et al [69] and Reuss et al [39] for the DUT and OSU tests respectively.

4.2 Geometric Model of the NREL Wind Turbine

The test turbine of the NREL NASA-Ames Unsteady Aerodynamics Experiment was a two bladed, 10 meters rotor diameter stall-regulated wind turbine with rated power of 19.8 kW. It has a tower height of 12.2 m and was rotating at 72 rpm synchronous speed. Both upwind and downwind configurations were tested, as well as various yaw and blade tip pitch angles. A photo of the actual test turbine inside the wind tunnel is shown below in Figure 4.2.1.

Figure 4.2.1: UAE phase VI rotor in the NASA Ames wind tunnel

The two blades of the turbine were non-linearly twisted and linearly tapered, using exclusively the aforementioned S809 airfoil developed by Airfoils Incorporated under contract by NREL, which was optimised for better wind power production [34]. The blade dimensions are illustrated below in Figure 4.2.2 and the blade chord and twist distribution along the span are shown in APPENDIX B: NREL Phase VI Turbine Chord and Twist Distributions.

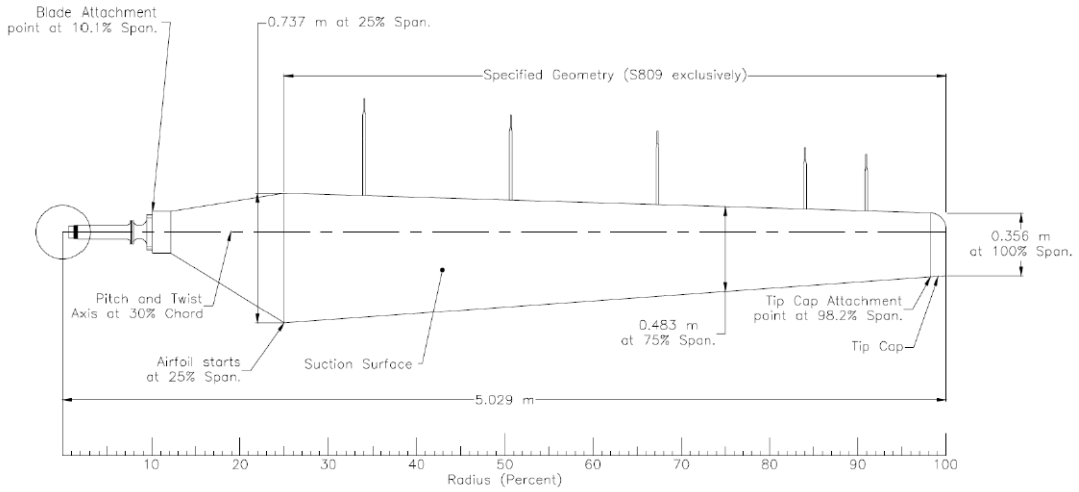

Figure 4.2.2: Blade platform dimensions

Apart from the specified geometry where the S809 airfoil was used exclusively from 25% span to the tip, where the blades were tapered with the chord length decreasing from 0.737 m to 0.356 m , the root and hub adapter part shows a transition in cross section from the airfoil shape to a circle towards the hub at 12% span, and it is shown in details in APPENDIX C: NREL Phase VI Turbine Blade Root Surface Depiction.
However, the near hub root section and the tip section were not specifically defined in the technical report [34], therefore a simple interpolation with linear transition was applied to the root section and the tip was treated as a flat surface, which would certainly have effects on the accuracy of computational predictions.

With pressure taps along the blade span and various types of sensors mounting on the turbine body, pressures distribution on the blades and the hub, shaft torque, and the root flapwise and edgewise bending moments were measured and recorded. At 5 nominated span-wise sections shown as black solid lines in Figure 4.2.3 (i.e. 0.30, 0.47, 0.63, 0.80 and 0.95 r/R), full distribution of pressure around the sections were

captured by 22 taps, allowing the corresponding aerodynamic force coefficients to be calculated and compared with computation results [34].

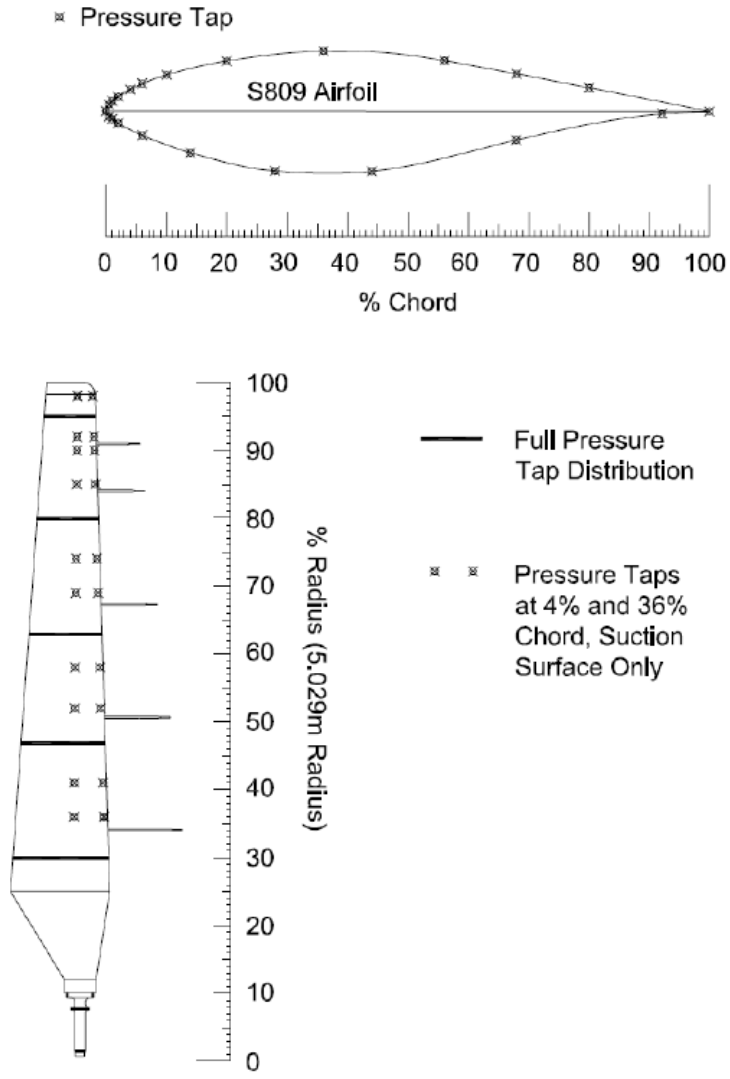

Figure 4.2.3: Blade surface pressure tap locations

As the NREL Phase VI wind turbine was stall regulated instead of pitch regulated, its maximum power generation depends entirely on the extreme condition at stall. Therefore, the accurate prediction of stall initiation on the turbine blades becomes crucial in controlling the turbine rotation, which remains a rather challenging task for CFD modelling.

4.3 Test Case Configuration

4.3.1 S809 configuration

The model was tested experimentally by DUT at Reynolds number ranging from 1.0×10^6 to 3.0×10^6 based on the model chord. Tests started with increasing angle of attack from 0° until a full separation of flow on the upper surface at about 20° and then decreased incidence angle to determine hysteresis. Based on the experiment, detailed computational case configurations were drawn and listed below.

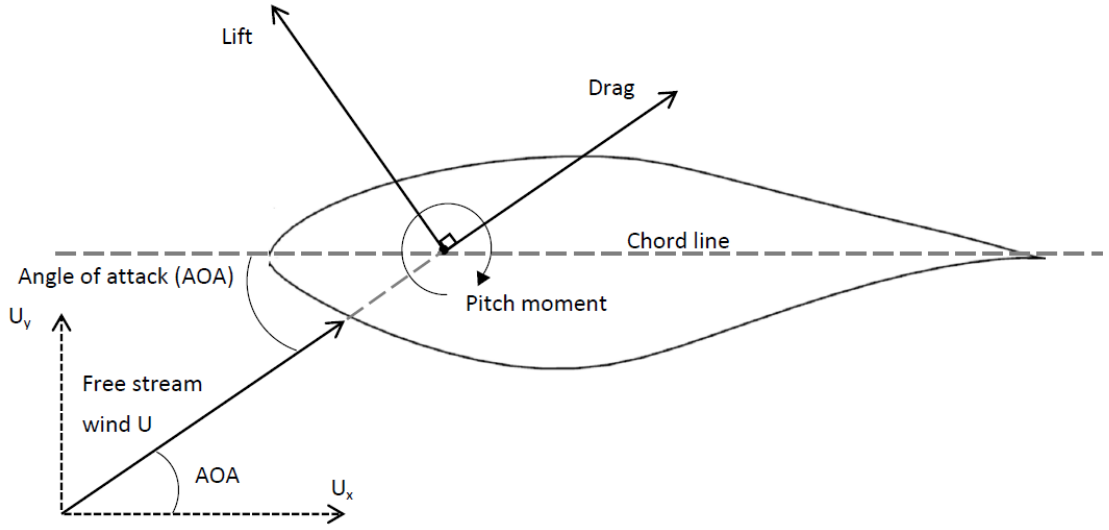

Figure 4.3.1: Velocity and aerodynamic forces conventions

Cases	AOA	$U_x(m/s)$	$U_y(m/s)$
1	0.00°	15.00	0.00
2	5.13°	14.94	1.34
3	7.17°	14.88	1.87
4	9.22°	14.81	2.40
5	12.22°	14.66	3.175
6	14.24°	14.54	3.69
7	20.15°	14.08	5.17

Table 4.3.1: Test cases at 15 m/s free stream velocity

Various angles of attack were investigated with the maximum being 20.15°. Since one of the major tasks was to capture the initiation of stall, which was found to be around 9° from NREL experimental data, test cases were concentrated around this angle. The free stream velocity of M=0.044, i.e. 15 m/s, was chosen to give a Reynolds number of 1.0×10^6 and was decomposed into the horizontal and vertical components with respect to the angle of attack.

4.3.2 NREL Phase VI configuration

Numerous data based on different test sequences were captured during the experiment. Sequence 'S' is chosen to be the candidate in the following analysis, which was also used in the blind comparison. This sequence included a series of upwind tests with 3 blade tip pitch and slow yaw sweep. The inlet wind speed was varied from 5 m/s to 25 m/s, while the turbine was maintained at a 72 rpm rotational speed. Structurally, all connection were rigid, cone angle was set to 0 and no probes were attached, allowing free transition to occur [34].

Case	Tip Pitch Angle (°)	Yaw Angle (°)	Air T (°C)	Wind Speed (m/s)
S0700000	3.0	0.0	11.1	7.0
S1000000	3.0	0.0	11.0	10.0
S1300000	3.0	0.0	13.7	13.0
S1500000	3.0	0.0	14.2	15.0

Table 4.3.2: Computational cases and parameters

It is worth noting that standard Spalart-Allmaras turbulence model was used exclusively for the 3D cases.

4.4 CFD Methodology

The computational fluid dynamic package used for this project is ANSYS, which is a platform of integrated engineering simulation programs capable of complex multi-physics solutions. The core code solver used is FLUENT, that is an implicit, unstructured, time accurate flow solver for both inviscid and viscous compressible flows. Apart from the main solver, the platform also contains programs for mesh generation, finite element based mode shape interpolation, pre- and post-processing.

Governing Equations

The point of CFD analysis is discretization. During the simulation the flow motion is not solved in any position of the domain, but in the center of all the fluid elements of the computational grid. The basis of the numerical method applied stands in the Navier-Stokes equations set, which include some pillar principles of physics: the conservation of mass, momentum and energy. The incompressible fluid approximation has been employed, as the involved Mach number values are low enough. The conventional limit is considered at 0.3, and for the highest wind speed simulated in this work a value around 0.1 has been computed. Therefore, the flow velocity doesn't introduce significant changes in air temperature or in its density ρ . This is a common approach not only for liquids, but even for air flowing at moderate speeds. The next two equations are the aforementioned conservation equations considering the incompressibility hypothesis: mass (4.1) and momentum (4.2)

$$\nabla \cdot \vec{u} = 0 \tag{4.1}$$

$$\frac{\partial \rho \vec{u}}{\partial t} + \rho(\vec{u} \cdot \nabla)\vec{u} + \nabla p = \mu \nabla^2 \vec{u} + \rho \vec{g} + \vec{F} \tag{4.2}$$

Also, if ρ is constant, energy equations are an independent set, not correlated to continuity and momentum. As the analysed situation doesn't treat heat transfer, these equations are not considered in the model.

Since the flow to be solved is characterized by turbulence, the variables experience a continuous random fluctuation in time. Any of these variables ϕ can be represented by an average value $\overline{\phi}$ plus an oscillating term ϕ'. The $\overline{\phi}$ term is a time-averaged value and if this method is applied to the previous relations, Reynolds averaged Navier-Stokes (RANS) equations are obtained.

The solutions are average values in the time interval Δt, which is big enough compared to molecular scales causing the momentum transfer, but much smaller than the characteristic scales of the analysed problem. This procedure of continuum approximation strongly reduces the computational effort when the detailed solution of turbulence structures is not of first importance, and when the mean flow has a dominant effect on the anisotropy of turbulence. Moreover, the direct calculations of turbulent fluctuation for smaller scales, like Large Eddy Simulations (LES) and Direct Numerical Simulations (DNS), is still prohibitive for most of the practical applications.

Turbulence

The turbulence model choice is a fundamental step that significantly influences numerical results, because they are employed to obtain an estimation of the Reynolds stresses and close the RANS system of equations. They can be roughly divided in one-equation or two-equations models: in one equation model, like Spalart-Allmaras, the differential transport equation for turbulent kinetic energy k is solved. In two-equations models, like $k-\epsilon$ or $k-\omega$, in addition to the k equation another one is solved, determining either the rate of k dissipation, ϵ, or the specific dissipation $\omega = k/\epsilon$.

Another widespread turbulence models employed in wind turbine simulations is the $k-\omega$ SST model. It is a combination between the two previously mentioned models: a blending function ensures the gradual variation from $k-\omega$ to $k-\epsilon$ moving away from the wall, such that advantages are taken from both. In this project, three turbulence models will be investigated, in order to understand which one is the best for the considered case.

Boundary Conditions

The computational mesh was imported in Fluent pre-processor. Air was considered as an incompressible fluid, as already stated, and its density was set to the experimental value for each wind speed, as reported in Table 4.4.1. No slip wall condition was set for the blade, velocity inlet condition was applied for the front section, with wind direction normal to the surface. Turbulent intensity was set to 5%, which is Fluent standard value, even if a lower value could be suggested to simulate the wind tunnel controlled inflow conditions.

Zero gauge pressure was set to the rear section of the control domain with the pressure outlet condition, and the same turbulence parameters of the inlet section were applied. Discretization for pressure, momentum, k and ω was imposed to second order. A maximum allowable Courant number of 40 was chosen, accordingly to Fluent advice and explicit relaxation factors of 0.5 and 10^{-6} residuals were used. A lift and drag monitor were set to check the convergence trends during the simulation and then 10000 iterations were launched.

Table 4.4.1: Wind speeds, densities and pressures

Speed $[m/s]$	Density $[Kg/m3]$	Pressure $[Pa]$
7.016	1.246	101959.328
10.047	1.246	101894.813
13.069	1.227	101410.336
15.098	1.224	101365.945
20.131	1.221	101204.07
25.109	1.22	101025.648

4.5 Results and Analysis

4.5.1 2-D Grid of the S809 Airfoil

For grid generation, the integrated mesh generator in ANSYS was used, due to its extensive mesh functions and ease of use. The S809 airfoil has a chord of 600 mm and 21% thickness and it is to be tested with a Reynolds number of 1.0×10^6. The chord length of the airfoil geometrical model was set to 1 m in ANSYS, which resulted a free stream air flow of about 15 m/s due to dynamic similarity. To avoid possible effects of far field boundary on the flow around the airfoil, the grid domain was set to be 30 chord in horizontal and 30 chord in vertical direction away from the blade, as it is possible to see in figure 4.5.1.

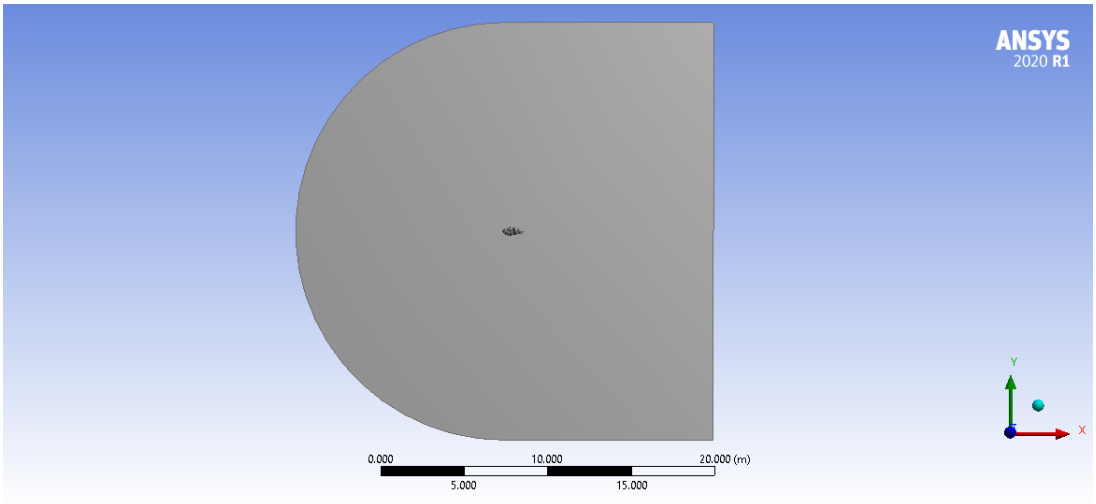

Figure 4.5.1: Computational domain and far-field boundaries

A structured quadrilateral mesh was applied to the geometrical model, with a total number of 376500 elements along with a set of structured quadrilateral boundary layers (inflation layers). The boundary layer was attached on the airfoil surface with 15 layers and a relatively slow growth rate of 1.1, starting with a row depth 0.0002 m. Size function was defined for refinement around the leading and trailing edge to capture the stagnation point and wake flow respectively. This grid density was tested to produce good spatial and temporal resolution for simple aerodynamic and aeroelastic computations.

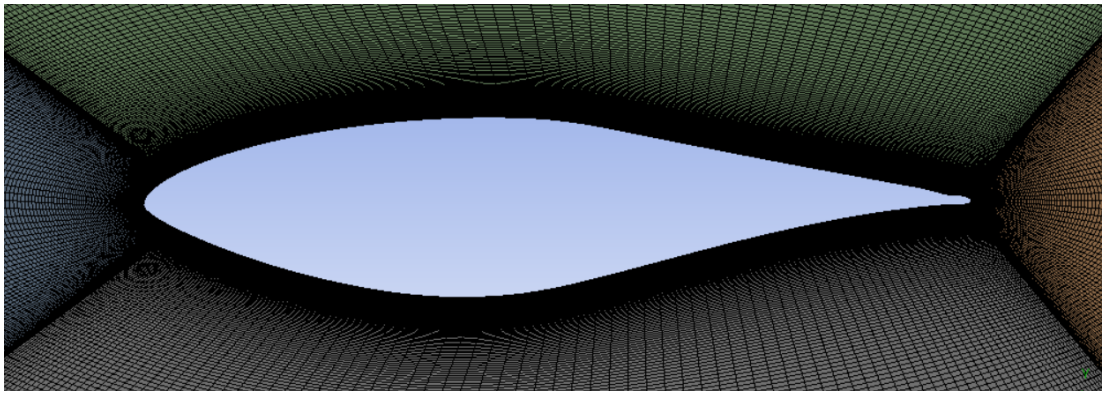

Figure 4.5.2: Detailed mesh around the airfoil

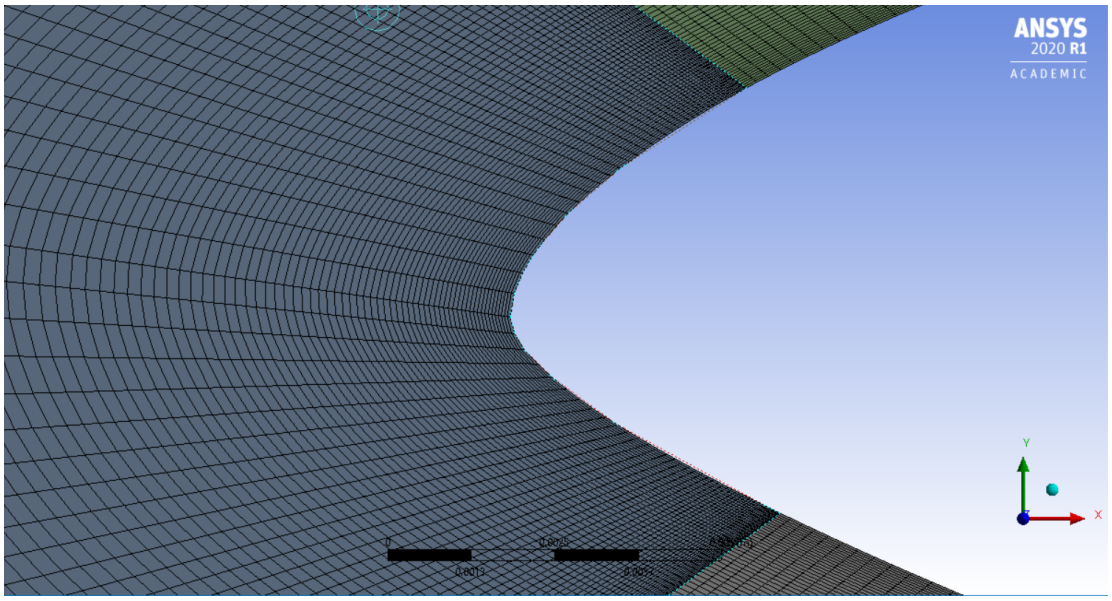

Figure 4.5.3: Detailed mesh around the leading edge

Structured grids have the possibility to reduce the computational time respect to unstructured grids due to the explicit storage of inter cell connectivity, maintaining an high quality to achieve the desired results. On the other hand, it is very complicated to generate a structured mesh for complex body construction, such as a complete aircraft. In this specific case, due to the relative simplicity of the considered geometry, it was decided to use a structured mesh for the advantages described before.

4.5.2 Aerodynamic Results - Steady

Aerodynamic Coefficients

The results for aerodynamic force coefficients, Lift and Drag coefficients, were obtained and shown below in Table 4.5.1. Three different turbulence models were tested in this calculation: Spalart - Allmaras, $k-\epsilon$ and SST $k-\omega$ turbulence model.

Table 4.5.1: Aerodynamic force coefficients prediction

AOA (°)	**Cl**				**Cd**			
	S-A	$k-\omega$	$k-\epsilon$	*Exp*	*S-A*	$k-\omega$	$k-\epsilon$	*Exp*
0.00	0.112	0.096	0.111	0.139	0.0131	0.0141	0.0147	0.0094
5.13	0.665	0.635	0.6632	0.736	0.0163	0.0171	0.0177	0.0097
7.17	0.862	0.823	0.863	0.913	0.0196	0.0205	0.021	0.0127
8.20	0.952	0.906	0.9545	0.952	0.022	0.023	0.0233	0.0169
9.22	1.031	0.976	1.0375	0.973	0.0249	0.0265	0.0262	0.0247
10.21	1.0935	1.0198	1.108	0.952	0.0289	0.0318	0.0297	0.0375
11.21	1.1326	1.032	1.161	0.947	0.035	0.0402	0.0344	0.0725
12.22	1.1379	1.033	1.2	1.007	0.04435	0.0501	0.0403	0.0636
14.24	1.141	1.055	1.221	1.055	0.0662	0.0697	0.0562	0.0828
20.15	0.86775	1	0.95	0.923	0.197	0.20	0.22	0.1853

It is worth mentioning that both steady and unsteady calculations were performed. For high angles of attack (post stall), no convergence could be achieved in steady computation due to a substantial amount of flow separation, thus unsteady time accurate computations were necessary and the results are shown as circled data points in the following plots. Since the $k-\epsilon$ turbulence model has generated coefficients predictions far from the experimental data, with an average difference greater than 10%, a comparison between the other two more promising methods was performed.

According to the plots of lift and drag coefficients shown in Figure 4.5.4 and Figure 4.5.5, it is evident that the $k-\omega$ turbulence model predicts the flow condition much more accurately than the Spalart-Allmaras one, thanks to its accuracy for adverse pressure gradient prediction in simulating near stall flow. Nevertheless, the standard Spalart-Allmaras model actually predicts the trends rather well, despite being inaccurate about the exact values at certain conditions.

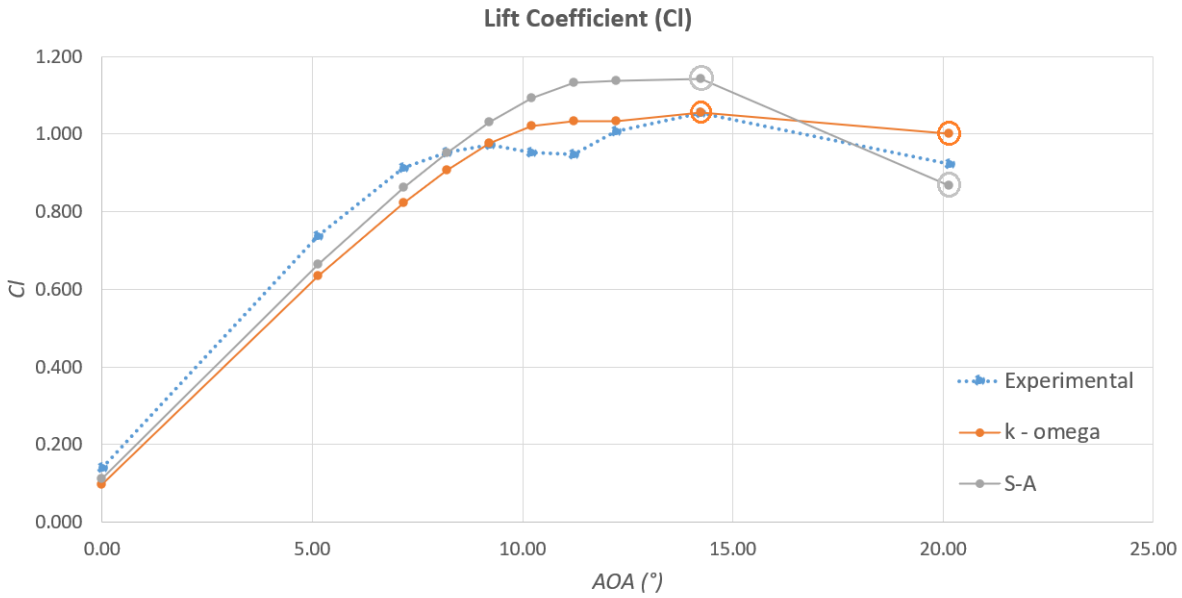

Figure 4.5.4: Lift coefficient vs. angle of attack

It can be seen from the lift coefficient plot shown in Figure 4.5.4 that the lift predicted by the SST $k-\omega$ model is very similar to the DUT experimental measurements. Unlike the experimental results or CFD predictions performed by other authors [79], no apparent point of stall was detected which is supposed to be around 9°. However, the lift curve slope does show a significant decrease between 10.21° and 14.24°, which indicates possible flow separation and the occurrence of stall, even though strictly speaking a decrease of lift coefficient is not detected. This is further proved by inspecting the pressure coefficient and streamline plots at these angles of attack later. Moreover, it is clear that the lift force is under predicted at all incidents compared with DUT measurements until stall takes place (around AOA=9°). The unclear detection of stall point and the over prediction of lift after stall both indicate a lack of turbulence level compared with realistic flow, showing that the separation process takes place a lot slower. The calculated high lift coefficient at 20.15° is on the other hand due to the large amount of unsteady fluctuation, since at this incidence the flow is fully separated from the upper suction surface. Thus, only a cycle averaged value is chosen to be shown on the plot and is very hard to compare with the experimental data since the experiment itself experienced unsteadiness as well at this flow incidence. The general trend of lift prediction by the two codes are very good comparing to some popular previous studies by Wolfe and Ochs [79] and Guerri et al [32]: substantial under- and over-predictions for the same SST $k-\omega$ turbulence model were present.

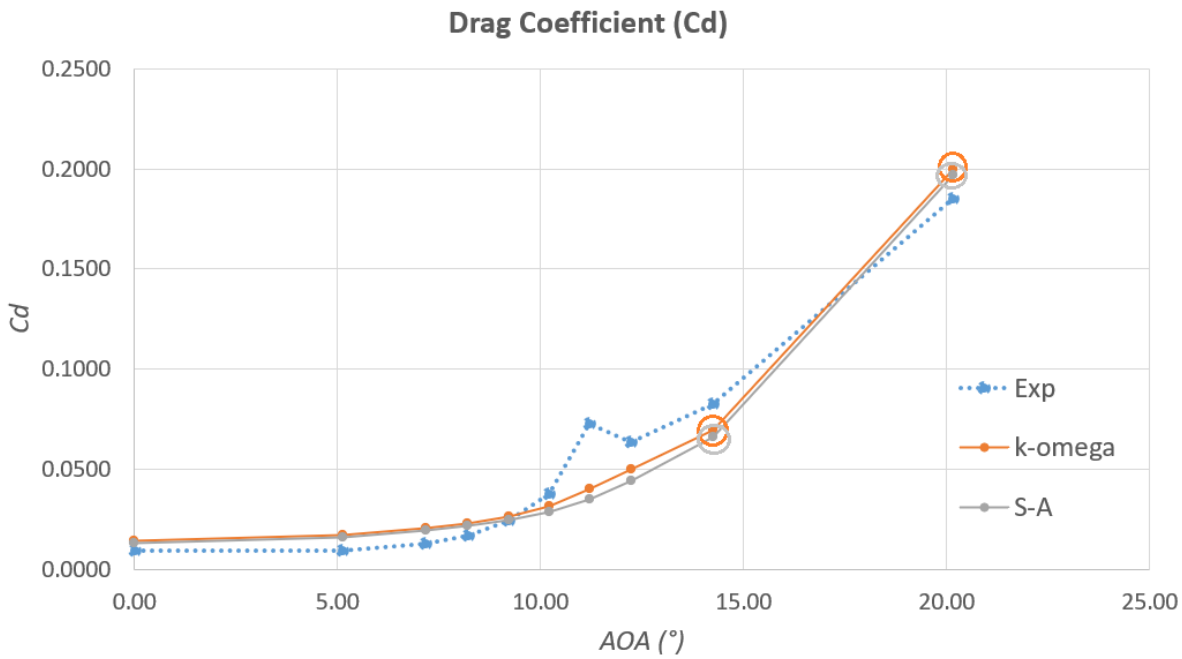

Figure 4.5.5: Drag coefficient vs. angle of attack

In spite of the slightly difference in predicting the lift coefficient by the two models, the drag force is similarly predicted with good agreement with experimental data shown in Figure 4.5.5. It is important to know that only the pressure drag is accounted for in this plot, meaning that the viscous shear drag is ignored since it is considered to be orders of magnitude smaller. The SST $k-\omega$ model experiences an over-prediction until the airfoil reaches stall condition, while after stall an under-prediction is experienced, but always following the parabolic shape of the experimental data. The peak at 11.21° was not captured in the computation. However, by considering that none of the previous authors [32] [79] had successfully predicted the drag peak, it is fair to assume that the peak could be experimentally induced. The slight over-prediction at 20.15° is probably due to the same reason as the over-prediction of lift at the same point.

Predictions of the Spalart-Allmaras model show very similar results with the $k-\omega$ one, except for slightly smaller post stall values. This is sensible as the flow around the airfoil in SST $k-\omega$ computation experiences a higher turbulence level on the suction surface after flow separation, leading to a slightly higher drag force.

Pressure distributions

Pressure coefficients around the airfoil were calculated to further investigate the solver performance. Plots of results using the SST $k-\omega$ turbulence model at angles of attack of 0°, 5.13°, 9.22°, 14.24° and 20.15° are presented below in Figure 4.5.6. The range of the angle of attack in the plots completes a full coverage from zero incidence to fully stalled condition (20.15°), thus should give a general idea of how the code is able to cope with different flow regimes.

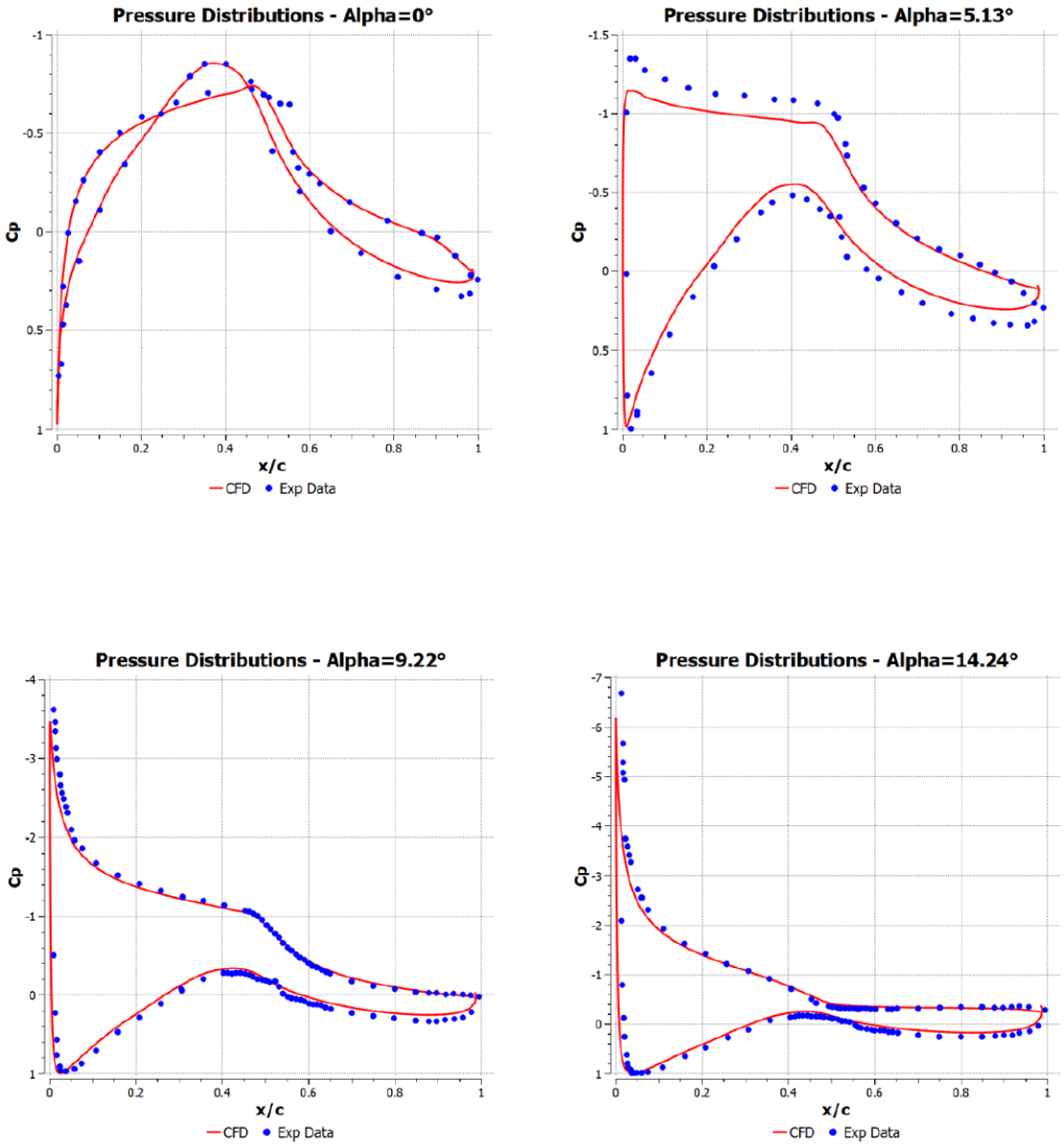

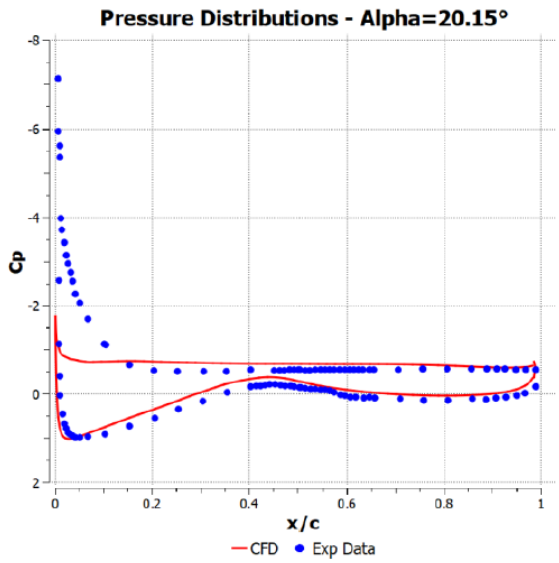

Figure 4.5.6: Pressure distribution around the airfoil at various angles of attack

At zero incidence, the overall prediction shows good agreement with the experimental data, except for mid chord region on the upper surface and the trailing edge region. In the experiment conducted by DUT, laminar separation bubbles were observed on both the pressure and suction surfaces just after the mid chord, causing a nearly flat distribution of pressure with respect to x/c [69], which is not captured by the fully turbulent simulation. The following sudden increase in pressure due to turbulent re-attachment also can not be identified on the plot. The computation error at the trailing edge on the other hand is possibly due to the fact that the thickening of boundary layer as flow travels along airfoil surface is not well captured. This might be the result of a slightly thin boundary layer construction during grid generation phase. Moreover, the situation is likely to deteriorate when the solver is over allowing flow separation due to the numerical setup, which shows a low pressure distribution on the pressure surface at the last 40% of the chord. This phenomenon can be identified on higher angles of attack as well.

For AOA = 5.13°, the general trend of prediction is similar to that of the 0° case. Laminar separation bubbles are not captured, and the rear of the airfoil experiences more separated like flow which is probably due to the same reason as the zero incidence case. The pressure distribution on the forward half of the lower surface is constantly under predicted, but only by a very little amount. However for the forward half of the

upper surface, the suction peak is never reached and the pressure distribution is not well captured. A similar discrepancy of the prediction can be found in many works done on the S809 airfoil such as Wolfe and Ochs [79], Guerri et al [32] and Chang et al [22] although smaller inconsistencies were generally achieved. Wolfe and Ochs [79] further proved the problem for 5.13° angle of attack to be the incapable simulation of laminar to turbulent transition. Therefore, the reason for the major discrepancy between the computation results with the SST $k-\omega$ turbulence model and the experimental data is considered to be the combined effect of a lack of leading edge refinement, which contributes to the failure in capturing the suction peak close to the nose and a lack of transition model, which causes the following over prediction.

At 9.22° angle of attack and afterwards when the angle of attack was increased to 14.24°, the experimental airfoil entered the stall phase with very sharp suction peak (extremely low pressure) due to an exceedingly fast flow around the nose region. The pressure coefficient prediction turns out to be exceptionally good at these incidences, with identical data on the pressure side and on the suction side. The suction peak and the forward half of the suction surface pressure distribution are not perfectly captured, due to similar reasons for the previous cases. Nonetheless, the lift and drag coefficient are well calculated with only 1% and -8% errors respectively, as it is shown in table 4.5.2. Stall is detected while many other authors failed to achieve [79].

Table 4.5.2: Calculation errors of aerodynamic coefficients

AOA (°)	**Cl % error**			**Cd % error**		
	S-A	*k-omega*	*k-epsilon*	*S-A*	*k-omega*	*k-epsilon*
0.00	-19%	-21%	-20%	29%	20%	36%
5.13	-10%	-14%	-10%	28%	26%	42%
7.17	-6%	-10%	-5%	34%	21%	45%
8.20	0%	-5%	0%	30%	26%	38%
9.22	6%	0%	7%	1%	7%	6%
10.21	15%	7%	16%	-23%	-15%	-21%
11.21	20%	9%	23%	-22%	-15%	-33%
12.22	13%	3%	19%	-20%	-11%	-27%
14.24	8%	1%	16%	-13%	-8%	-22%
20.15	-6%	8%	3%	6%	8%	19%

At AOA=20.15°, the flow essentially detaches from the entire suction surface as the transition shifts to the point just after the leading edge. As can be seen on the pressure coefficient plot, the over prediction of pressures on the upper suction surface just behind the leading edge is due to a deeper stall of the airfoil, since it experiences stall earlier than the experimental case. Nevertheless, the data of other regions is in good agreement with experimental measurements, which is better than a lot of other authors calculations with various turbulence models [79] [32]. It is worth noting that the SST $k-\omega$ turbulence model used by Guerri [32] and Le Pape and Lecanu [54] also provided very good results for nearly all angles of attack. This is mainly because of its speciality in predicting adverse pressure gradient, leading to a better simulation of separated flow on the upper surface.

Velocity contour and streamline plots

In order to investigate the behaviour of flow at certain incidences compared with the experimental case, velocity contour and streamline plots are presented with angles of attack 0°, 5.13°, 7.17°, 8.20°, 9.22°, 10.21°, 12.22°, 14.24° and 20.15° for the SST $k-\omega$ turbulence model. According to the contour plots in figure 4.5.8, the growth of flow separation with increasing angle of attack is clearly identified. It can be seen that starting from 7.17°, or even 5.13°, the flow over the upper surface shows a tendency to separate with the boundary layer significantly thickens. To prove this, the streamline plots are constructed below in Figure 4.5.7.

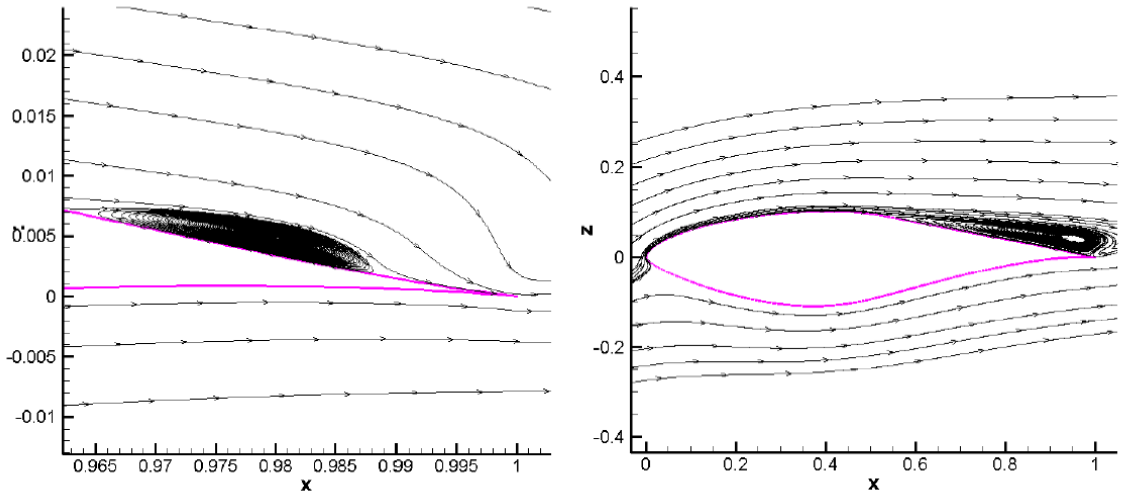

Figure 4.5.7: Streamline plots of 5.13° (left) and 8.20° (right) angles of attack

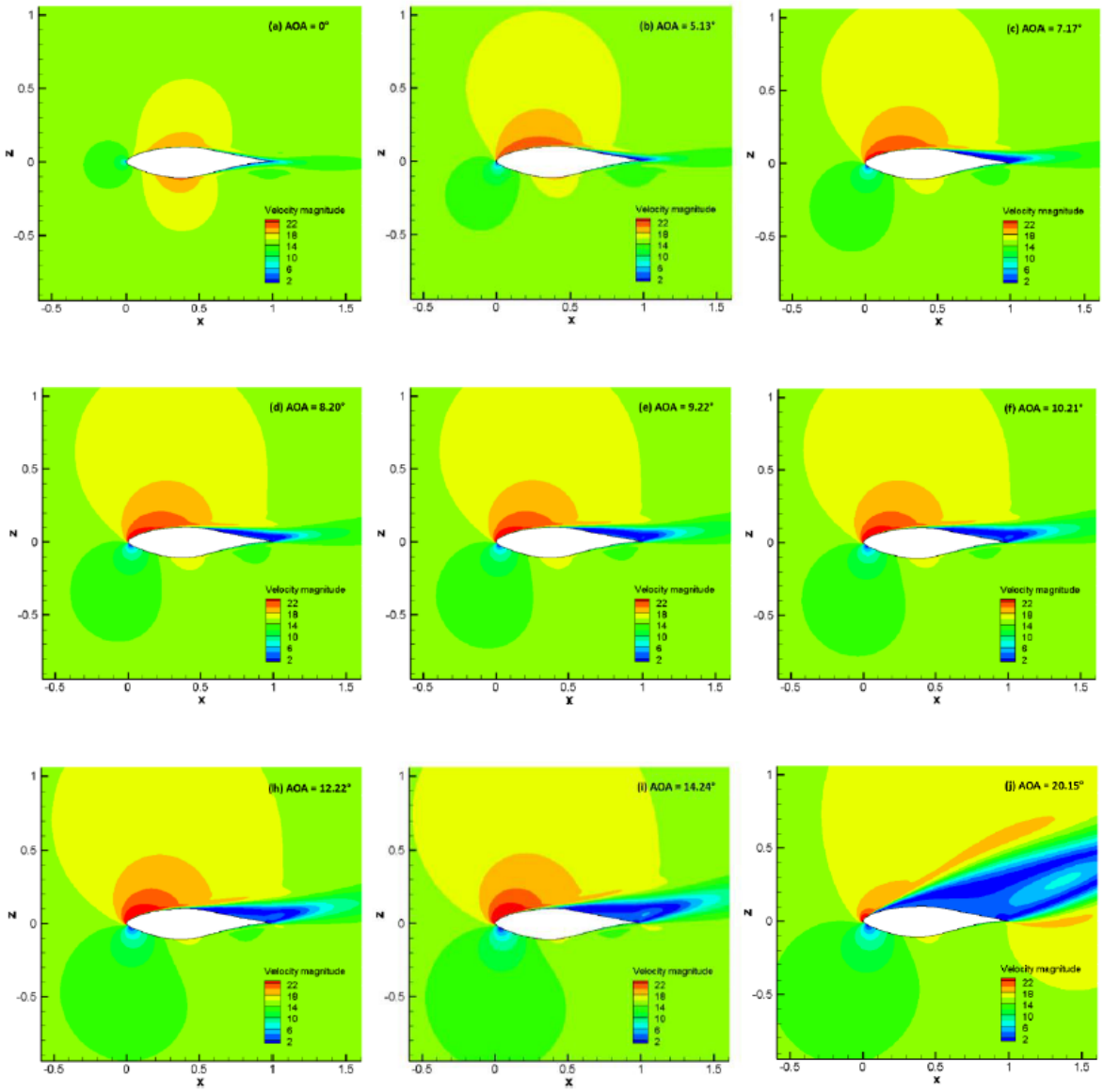

Figure 4.5.8: Steady contours of absolute velocity at AOA from 0° to 20.15°

The left plot of Figure 4.5.7 shows a clear separation very close to the rear end at about 98% chord, which then reattaches to the surface just before leaving the trailing edge. This is a premature separation prediction based on the experiment results, and it is believed to be one of the reasons causing the inaccurate prediction of the pressure distribution near the trailing edge in Figure 4.5.6. With this small separation initiating at 5.13°, the flow becomes more and more detached as the angle of attack increases. It can be seen that at angle of 8.20°, which is plotted on the right of Figure 4.5.7, there is the guessed point of stall initiation in previous sections, the rear half of the airfoil upper surface experiences separated flow. The situation here is far more developed than that measured in the experiment, where a small separation region was detected only

until 9.22°. Considering the sudden decrease of lift slope in the lift coefficient against angle of attack plot (Figure 4.5.4), it is evident that at around 8.20° the separated flow occupying 50% of the chord as seen above, has become so dominant that a further increase of angle of attack will slow down the lift growth.

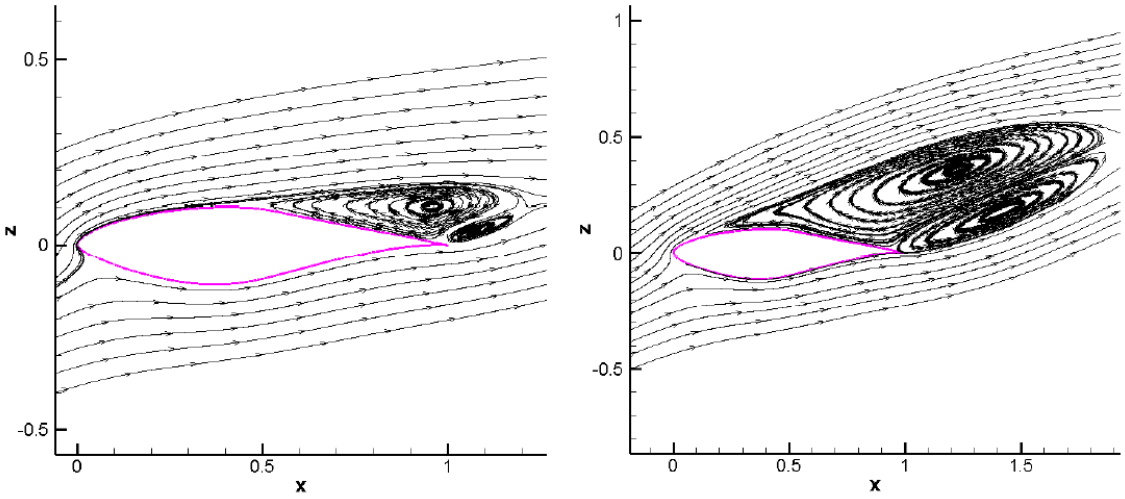

Figure 4.5.9: Flow separation at 14.24° (left) and 20.15° (right) angles of attack

By investigating the streamline plots at even higher angles of attack shown in Figure 4.5.9, the rapid growth of separation region can be identified. At AOA=14.24°, two large vortices are present and the flow separates the upper surface at about x/c=0.4, where in experiment it occurred at x/c=0.5. The close prediction of the separation point at this incidence is one of the main reasons leading to accurate pressure distribution prediction in Figure 4.5.6. Since the flow becomes very unsteady at a high angle of attack of 20.15°, only a stationary snapshot is chosen to be shown on the right of Figure 4.5.9. In this case, a full separation from the upper surface is seen with two huge vortices, causing the predicted lift to drop substantially. It is also interesting to notice that the flow arriving at the stagnation point have to travel backwards to pass around the leading edge which generates very high speed streams. Based on the streamline plot, it is clear why the pressure coefficient plot at 20.15° in Figure 4.5.6 matches very well with experimental data, as the experimental case also had separated flow for the entire upper surface. However, many other authors only got half chord separation from their codes' simulations due to delayed stall.

4.5.3 Aerodynamic Results - Unsteady

Regarding the unsteady behavior of the flow, the case of the airfoil with an angle of attack of 20.15° is considered. In this configuration, full stall is present, as explained in the previous sections. After a short period of transition, where an increasing flow separation from the suction surface is present, the flow starts oscillating with a periodic behaviour, bringing to the consequence formation of eddies in the airfoil wake (Figure 4.5.10).

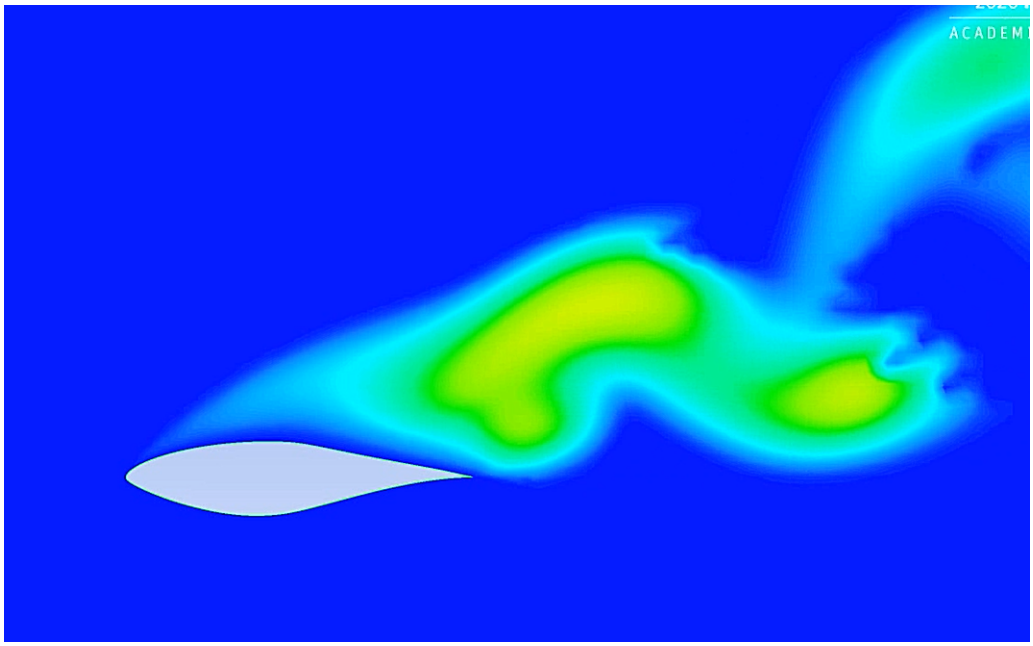

Figure 4.5.10: Eddies formation for airfoil at full stall condition

From this Figure, it is possible to clearly see the Kármán[1] vortex street, which is a repeating pattern of swirling vortices, caused by a process known as vortex shedding, which is responsible for the unsteady separation of fluid flows around bodies. As a consequence of the formation of a vortex, there is a modification of the pressure distribution around the body. Consequently, an alternating formation of vortices generates periodically variable forces and therefore a vibration of the body [80]. If the frequency of formation of the vortices approaches the natural frequency of vibration of the body, the phenomenon of resonance can occur, which can lead to flutter, as explained in Chapter 3, vibrating with harmonic oscillations driven by the energy of the flow with possible failures of the structure.

[1]From T. Von Kármán, the Hungarian engineer and physicist who discovered this phenomenon

This is the mainly reason because it's crucial to analyze the frequency of formation of the vortices and, for this scope, it has been studied the unsteady behaviour of the lift during the transient simulation, which is shown in Figure 4.5.11.

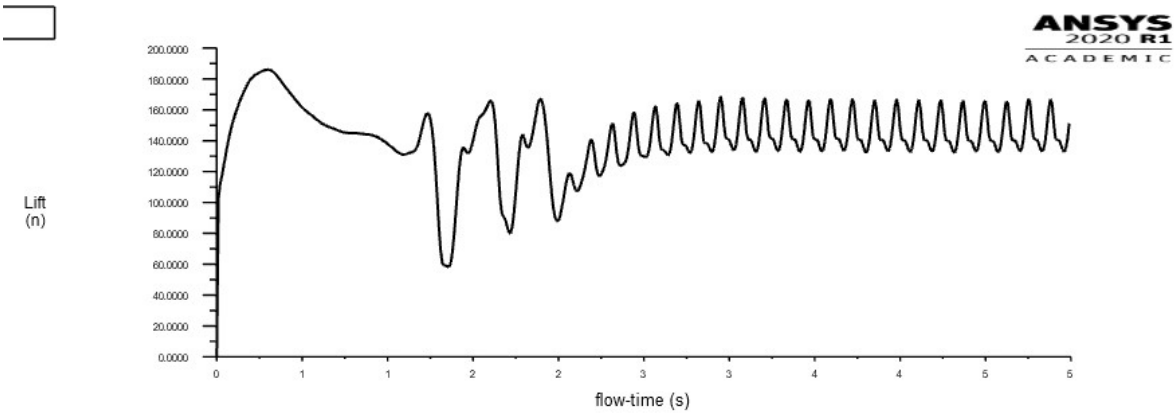

Figure 4.5.11: Unsteady lift curve at 20.15° (Full stall)

It is possible to see the oscillating behaviour due to the formation of the vortices, after the initial transition period of few seconds. This function was analyzed during the oscillation period with a Fast Fourier Transform (FFT), thus the signal was converted in MATLAB through a specific code from its original time domain to a representation in the frequency domain, as shown in figure 4.5.12.

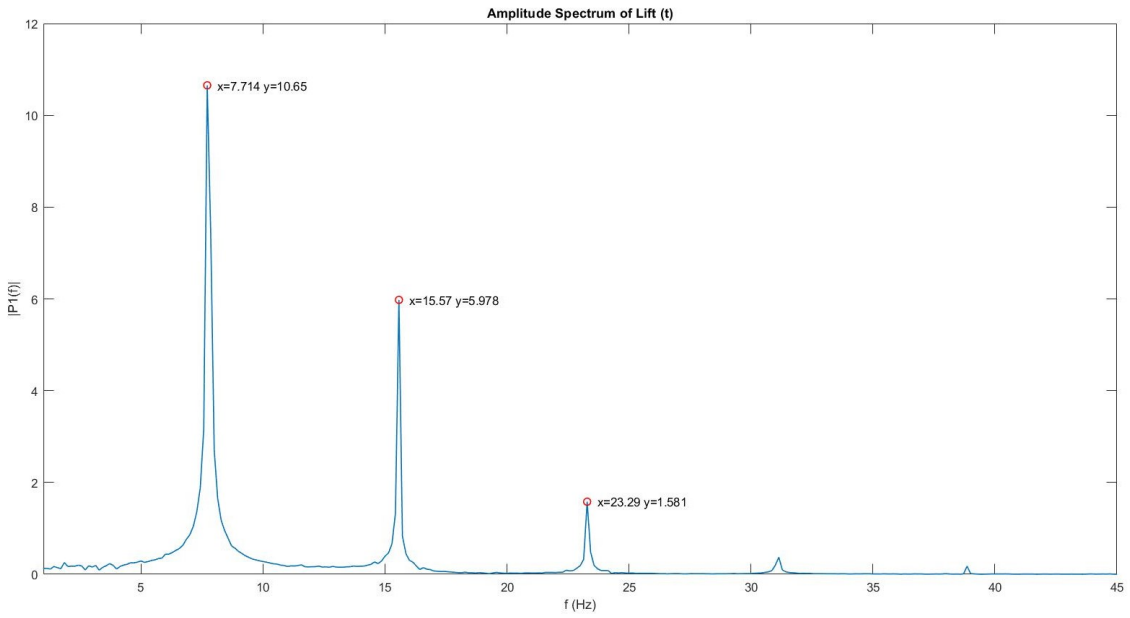

Figure 4.5.12: Lift spectrum in frequency domain

From this plot it can be seen that the first and principal harmonic of the oscillating signal has a frequency $f = 7.714\ Hz \approx 48.5\ rad/s$. From this value, it's possible to calculate a fundamental parameter for this aeroelastic analysis: The Strouhal[2] number, which is a dimensionless number describing oscillating flow mechanisms.

The Strouhal number is given as

$$St = \frac{fL}{u} = \frac{L/u}{1/f} = \frac{\text{time for the flow to travel the entire airfoil}}{\text{time for airfoil to complete a vibration cycle}} \tag{4.3}$$

where f is the frequency of vortex shedding, L is the characteristic length of the airfoil and u is the flow velocity.

Normally, a Strouhal number of 1 indicates by the time a disturbance in the flow passes downstream the chord length, the airfoil has just finished its oscillation cycle. According to Von Kármán [77], this also means that the characteristic length L of the airfoil is equal to the wavelength of the disturbance.

It is always quite dangerous for operations with reduced frequency close to unity, which is introduced by Fung [28] that some experimental and empirical results showed a tendency of flutter around St=1 for large aircraft wings. In this particular case, the characteristic length of the airfoil is $L = 1\ m$ and the flow velocity is $u = 15\ m/s$, which lead to a Strouhal number $St = 0.514$, which implies very low possibility of flutter for this airfoil geometry and specific boundary conditions.

4.5.4 Aerodynamic Results - Trailing Edge Flap

Due to the proven results in aircraft applications and described as the most promising device for loads control in large wind turbines in many publications, it was decided to analyze the effect on applying a Trailing Edge Flap to the 2D S809 airfoil to compare the results with the standard configuration. Same CFD methodology and boundary conditions have been applied to the computational model, while the only different from the previous analysis is indeed in the geometrical model of the airfoil, equipped with a movable trailing edge flap.

[2]Named in honor of the Czech physicist Vincent Strouhal

The trailing edge flap, with a chord length of 20%, was designed using the same CAD software mentioned for the previous analysis and it is presented in Figure 4.5.13, with different flap angle configurations. The length of the trailing edge flap was chosen thanks to the promising results described in important publications like Tsiantas et al. [75] and Lutz et al. [46].

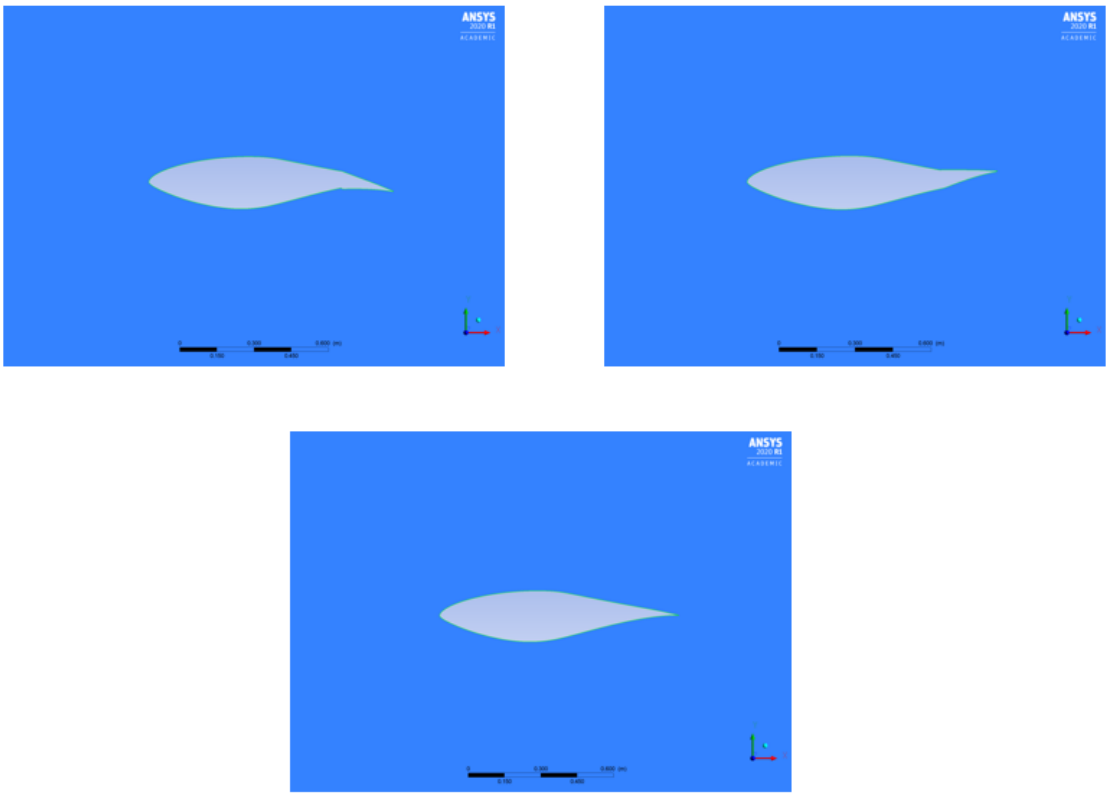

Figure 4.5.13: Cross sections for different flap configurations: +10°, -10°, 0°

The results for aerodynamic Lift force and Drag force were obtained and shown in Table 4.5.3. For this calculations the SST $k-\omega$ turbulence model was used. It is worth mentioning that both steady and unsteady calculations were performed.

For high angles of attack (post stall), no convergence could be achieved in steady computation due to a substantial amount of flow separation, thus unsteady time accurate computations were necessary and the results are shown as circled data points in the following plots.

Table 4.5.3: Aerodynamic force prediction

AOA (°)	Lift Force			Drag Force		
	Flap 10°	*Flap 0°*	*Flap -10°*	*Flap 10°*	*Flap 0°*	*Flap -10°*
0	64.45	13	-70.12	2.91	1.94	4.98
5.13	123.84	83.78	5.14	4.39	2.43	4.68
7.17	138.45	106.93	34.06	6.03	3.03	5.35
9.22	148.25	124.28	60.23	8.25	4.1	6.58
10.21	153.72	130.23	71.85	9.63	5	7.44
12.22	153.97	146.53	91.93	13.41	6.88	9.58
14.24	155.14	151.59	114.11	17.77	9.62	12.7
20.15	139.01	125.22	95.91	52.73	39.7	30.11

It can be noted, as shown in Figure 4.5.14, that the influence of the flap is significant. The deflection of the flap to the pressure surface (+10°) generates an increase in the aerodynamic loads, with a resulting increase of lift; while a deflection to the suction surface (-10°) decreases the aerodynamic loads generating a lift decrease. This occurs because, thanks to a movable flap, it's possible to modify the useful area of the pressure or suction side, with a consequently increase or decrease or lift.

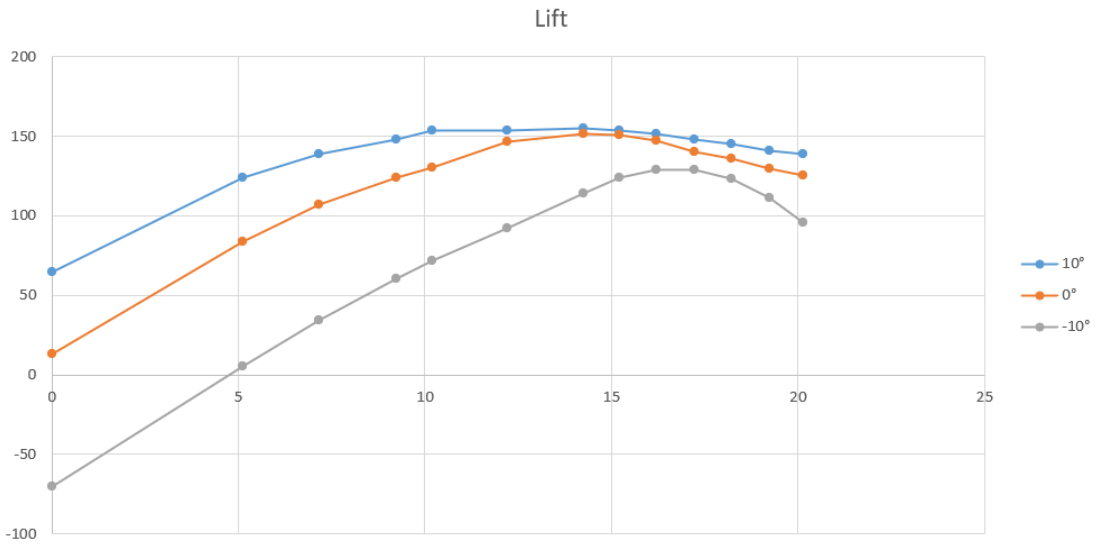

Figure 4.5.14: Lift force for different flap configurations: +10°, 0°, -10°

It's interesting to note that this difference is very high for small angles of attack, while it reduces as the AOA increases, reaching a point around stall where the difference is almost negligible. Again, this is due to the large amount of unsteady fluctuation in the flow, since at this incidence the flow is fully separated from the suction surface.

Two more observations can be done regarding the lift curve for the flap in upstream configuration (grey curve): at incidence of 0°, the lift force is negative, thus producing a rotation in the opposite direction of the desired one. For this reason, this configuration is mainly used for higher angles of attack, when the freestream velocity reaches high speed and the main purpose of the flap is to have a beneficial impact on blade loading, as it will be further explored in Chapter 6. It can be also noted that in this particular configuration, the stall condition starts some degrees of incidence after the standard and +10° configuration, so it can be said that some degrees of incidences are actually gained in this configuration. This is due to the particular geometry of this case, which delays the separation point in the upper surface of the airfoil, resulting in a delay of stall condition.

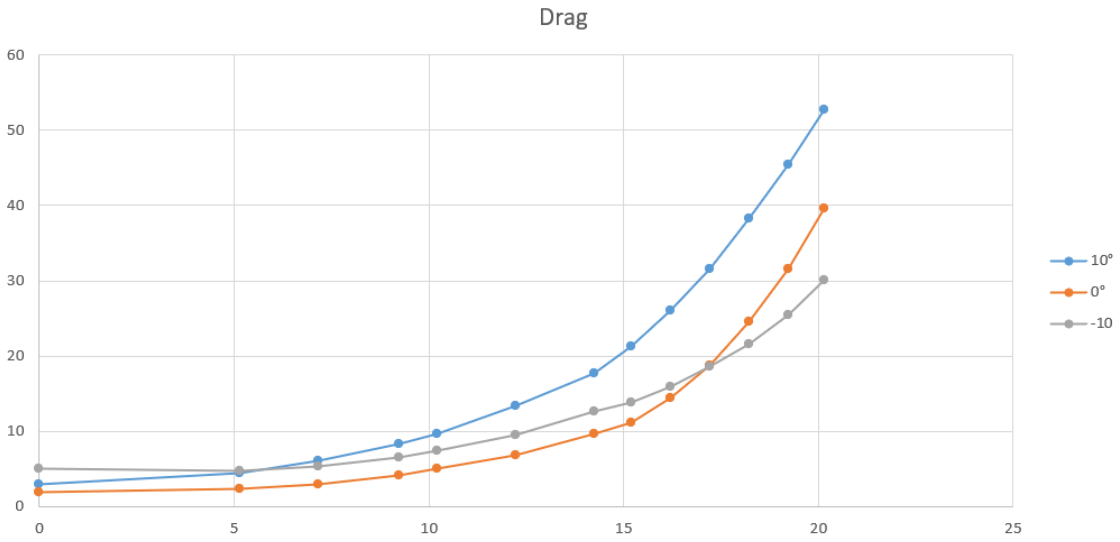

Figure 4.5.15: Drag force for different flap configurations: +10°, 0°, -10°

Regarding the drag force prediction, it's possible to see in Figure 4.5.15 that the behaviour of the drag function for the different configurations is the opposite of the lift function. The different between the configurations is very low for small AOA, while it increases with the increase of the angle of attack. This could be caused by the formation of *Form Drag*, which is due to the separation of the boundary layers from the

airfoil surface and the consequent lack of pressure recovery. This drag component can be larger than the frictional one when massive separation is involved and therefore it is important to reduce it as much as possible by delaying the separation. In this particular case, the separation is much higher for the configuration with the flap moved downwards (+10°), due to the particular geometrical model of this case.

Table 4.5.4: Lift force for different wind speeds

Wind Speed (m/s)	**Lift Force**		
	Flap 10°	*Flap 0°*	*Flap -10°*
3	5.94	3.23	1.36
5	16.61	7.52	3.81
8	42.6	29.34	9.79
10	67.07	45.99	15.29
13	114.4	78.38	25.84
15	153.3	104.24	34.37
18	221.95	152.28	49.42
20	274.66	188.66	60.96

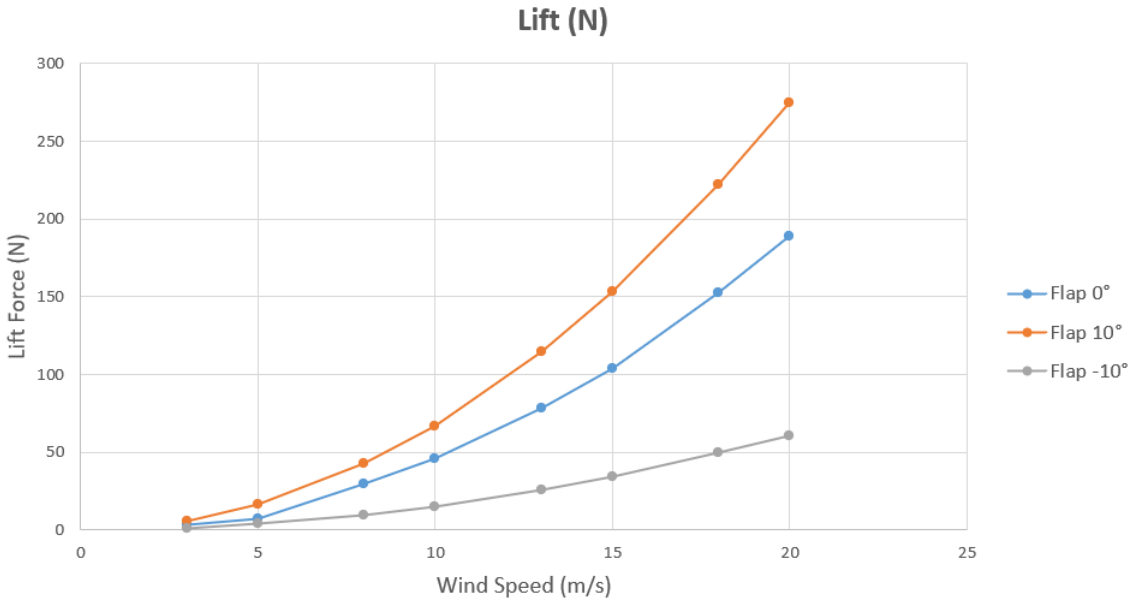

Figure 4.5.16: Lift force for different wind speeds and flap configurations

Lastly, the lift force for different flap configurations at different wind speeds can be seen in Figure 4.5.16. As expected, the lift increases proportionally with the increase in wind speed velocity, mostly for the configuration with flap moved to the pressure side. At the same time, it's very interesting to see that the lift curve for the -10° configuration is very flattened, with a relatively small increase of lift considering the high increase in wind speed. This observation will be an important insight for a further analysis which will be developed in Chapter 6.

Chapter 5

3-D Fluid Structure Interaction

5.1 CFD Case Configuration

For this analysis, a wind turbine blade (Figure 5.1.1) was modelled following the specification of the geometric model of the NREL wind turbine, as shown in details in APPENDIX C. The geometric CAD model of the blade was constructed using a commercial CAD software and then imported into ANSYS. The twisted and tapered blade body was constructed according to APPENDIX C, but since there is no clear record of the exact dimension of the blade root and tip sections, simple geometry was adopted. The blade tip was set to be a flat surface for simplicity and the root connection section was constructed using linear interpolation.

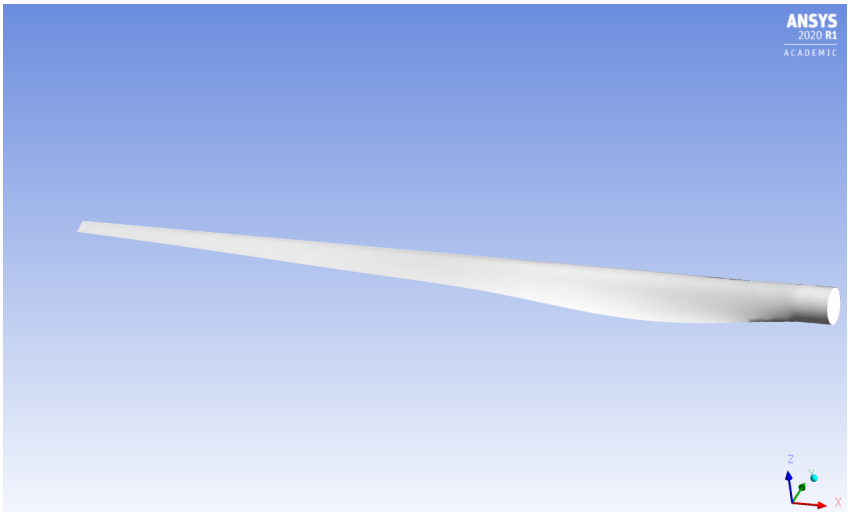

Figure 5.1.1: CAD model of the wind turbine blade

The blade is made out of an orthotropic composite material, it has a varying thickness and it also has a spar inside the blade for structural rigidity. The turbulent wind flows towards the negative z-direction at 15 m/s, which is a typical rated wind speed for a turbine of this size, as shown in figure 5.1.2. This incoming flow is assumed to make the blade rotate at an angular velocity of -3.22 rad/s about the z-axis (the blade is thus spinning clockwise when looking at it from the front, like most real wind turbines). The tip speed ratio (the ratio of the blade tip velocity to the incoming wind velocity) is therefore equal to 5, which is a reasonable value for a wind turbine of this size.

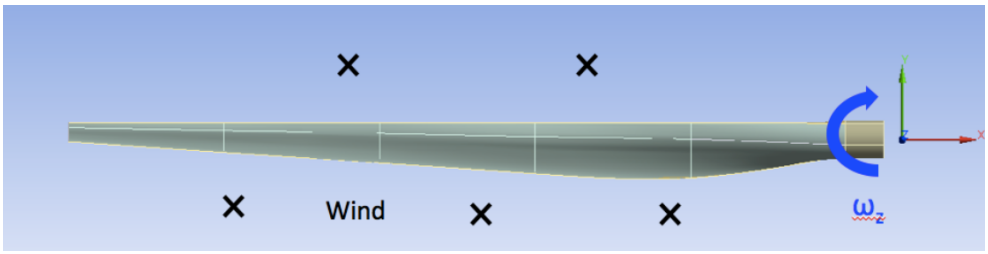

Figure 5.1.2: Front view of the wind turbine blade

5.2 CFD Methodology

The computational fluid dynamic and finite element method package used for this analysis is again ANSYS, thanks to its integrated platform of engineering simulation programs both for aerodynamic and structural analysis. In this case, the two solvers used are FLUENT regarding the CFD analysis in order to obtain the aerodynamic loading, and Mechanical APDL for the FEA structural analysis to determine stresses and deformations from the previous results. Apart from the main solver, also integrated programs for mesh generation, finte element based mode shape interpolation, pre- and post- processing were used.

Governing Equations

For this analysis, the governing equations are divided considering the two different simulations which will be performed. In the CFD analysis, for the case of a 3D rotating blade, the governing equations are the continuity equation or conservation

of mass (5.1) and Navier-Stokes equations or conservation of momentum (5.2). These equations are written in a frame of reference rotating with the blade. This has the advantage of making the simulation not require a moving mesh to account for the rotation of the blade.

$$\frac{\partial \rho}{\partial t} + \nabla \cdot \rho \vec{v}_r = 0 \tag{5.1}$$

$$\nabla \cdot (\rho \vec{v}_r \vec{v}_r) + \rho(2\vec{\omega} \times \vec{v}_r + \vec{\omega} \times \vec{\omega} \times \vec{r}) = -\nabla p + \nabla \tau_r \tag{5.2}$$

Where $\vec{v}_r$ is the relative velocity (the velocity viewed from the moving frame) and $\vec{\omega}$ is the angular velocity. Interesting to note the additional terms for the Coriolis force $(2\vec{\omega} \times \vec{v}_r)$ and the centripetal acceleration $(\vec{\omega} \times \vec{\omega} \times \vec{r})$ in the Navier-Stokes equations.

Also in this case, the flow to be solved is characterized by turbulence and the variables experience a continuous random fluctuation in time. For this reason, again the method of Reynolds averaged Navier-Stokes (RANS) equations is used to solve the problem and the $k - \omega$ SST turbulence model was selected to close the set of equations.

Regarding the FEA analysis, the governing equations are based on shell theory, which are an extension of the Euler-Bernoulli beam theory and plate theory. Shell theory takes the idea form the two previous mentioned theory and extend it to 3-dimensional and curved surface. In shell theory, the main focus is on the mid-surface of the structure and how that mid-surface is going to deform under the influence of a load, assuming that normals will remain normal at every point on the mid-surface. Without exploring in deep the mathematical details of shell theory, which are really complex from an analytical point of view, the main idea is that the solver finds the displacements and rotations at selected point in the mid-surface of the structure where the potential energy is minimized (point of equilibrium), after the influence of the specific load. In order to find the displacements anywhere in the structure, an interpolation process between the points is applied and the stresses and deformations are calculated through the potential energy of the mid-surface, knowing the materials characteristics and surface geometries.

Boundary Conditions

For the aerodynamic simulation, the computational mesh was imported in Fluent pre-processor. Air density was set to the experimental value for each wind speed, as reported in Chapter 4, Table 4.4.1. No slip wall condition was set for the blade, velocity inlet condition was applied for the front section, with wind direction normal to the surface. Turbulent intensity was set to 5% and turbulent viscosity ratio equal to 10. Zero gauge pressure was set to the rear section of the control domain with the pressure outlet condition, and the same turbulence parameters of the inlet section were applied. Discretization for pressure, momentum, k and ω was imposed to second order. A maximum allowable Courant number of 40 was chosen and an high explicit relaxation factors and 10^{-6} residuals were used. The simulation is performed in the rotating frame of reference (frame motion) and the periodic side boundary was applied to the model: only 1/3 of the full domain is modelled (one blade) using periodicity assumptions ($\vec{v}(r_1, \theta) = \vec{v}(r_1, \theta) - 120n$). Pseudo-transient simulation was applied and then 1500 iterations were launched.

Regarding the mechanical simulation, all the material properties reported in Table 5.3.1 are inserted and the pressure loads from the aerodynamic computation are uploaded. A remote rigid point was hold at the center of rotation, in order to simulate the effect of having the blade connected to hub to calculate forces and moment reactions. Stress stiffening effect was applied to the simulation: the faster the blade is spinning, the stiffer the response is going to be. This is very important because natural frequencies of an unstiffened and stiffened blade are very different. After this preliminary set-up, the simulation was launched.

5.3 Results and Analysis

5.3.1 3-D Grid of the Blade

For grid generation, again the integrated mesh generator in ANSYS was used, due to its extensive mesh functions and ease of use. The length of the blade geometrical model was set to 21.5 m in ANSYS, which resulted a free stream air flow of about 15 m/s due to dynamic similarity. In Figure 5.3.1, it is possible to see the geometry of the fluid surrounding the wind turbine blade and the outer boundaries of the fluid volume. In the middle, the blade is represented as a void, so an empty space inside the volume. To do this, the blade geometry was imported, translated and finally oriented, in order to face the incoming wind: indeed, the blade lays along the negative x-direction while the wind flows towards the negative z-direction.

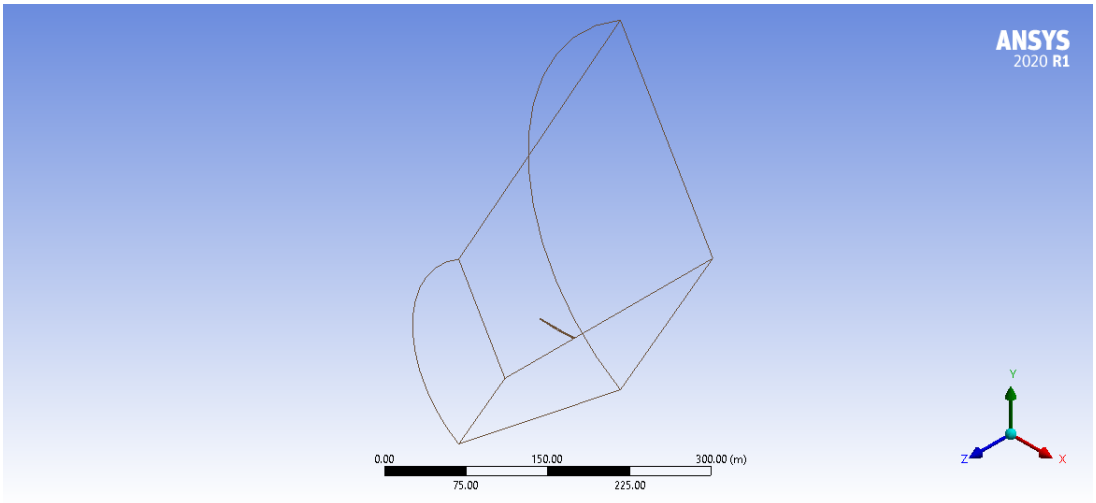

Figure 5.3.1: Computational domain

An unstructured tetrahedral mesh was applied to the geometrical model, with a mesh refinement around the blade in order to obtain more accurate results around this region, for a total number of 369312 elements. The boundary layer was attached on the airfoil surface with 10 layers, with a relatively slow growth rate of 1.2 and an high density around the leading edge and trailing edge. There is no deliberate cluster of elements at the tips or their trails since tip vortices are not the investigation objectives in this study.

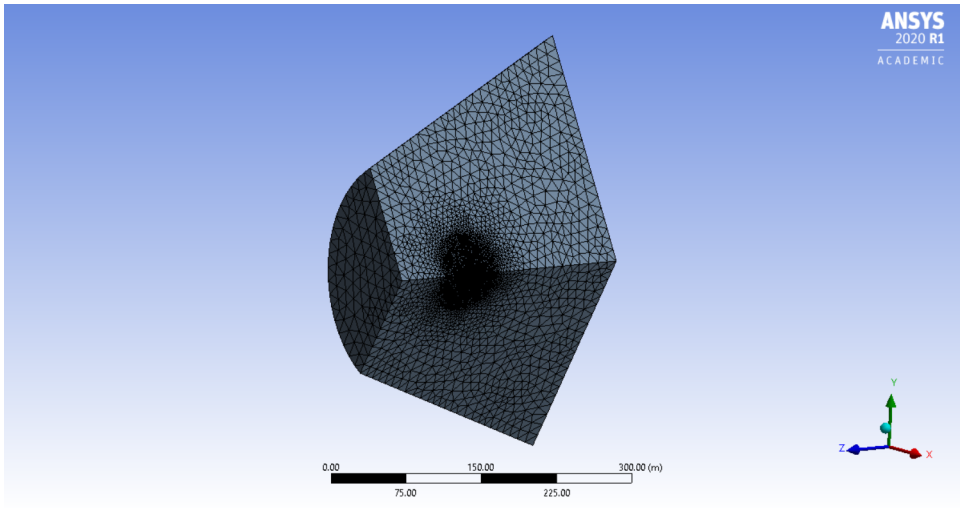

Figure 5.3.2: Meshed computational domain

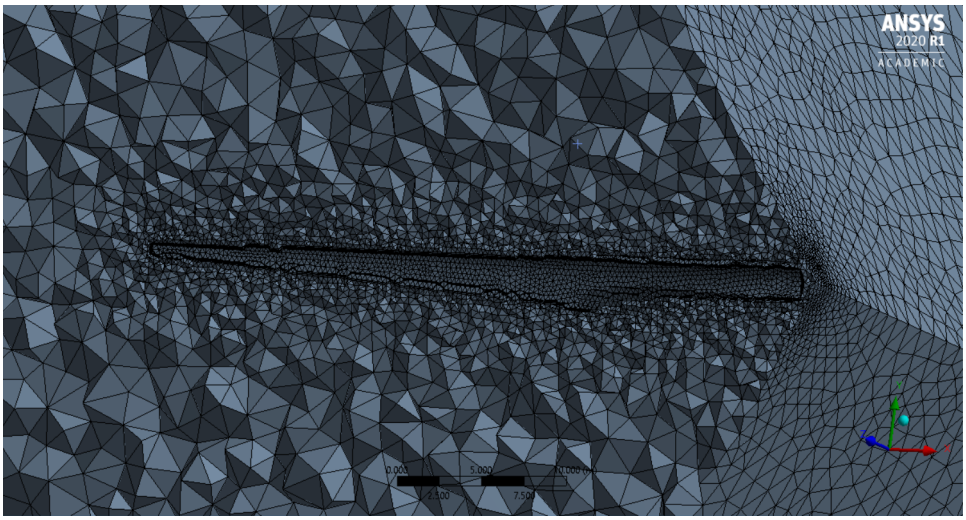

Figure 5.3.3: Detailed mesh around the blade

To avoid possible effects of far field boundary on the flow around the blade, the grid domain was set to be 25 blade lengths in horizontal and 15 blade lengths in vertical direction away from the blade.

Regarding the mesh of the blade for the structural analysis, a mapped face mashing was used for creating about 5000 quadrilateral elements, which are suitable for this kind of model, as it can be seen in Figure 5.3.4 and Figure 5.3.5.

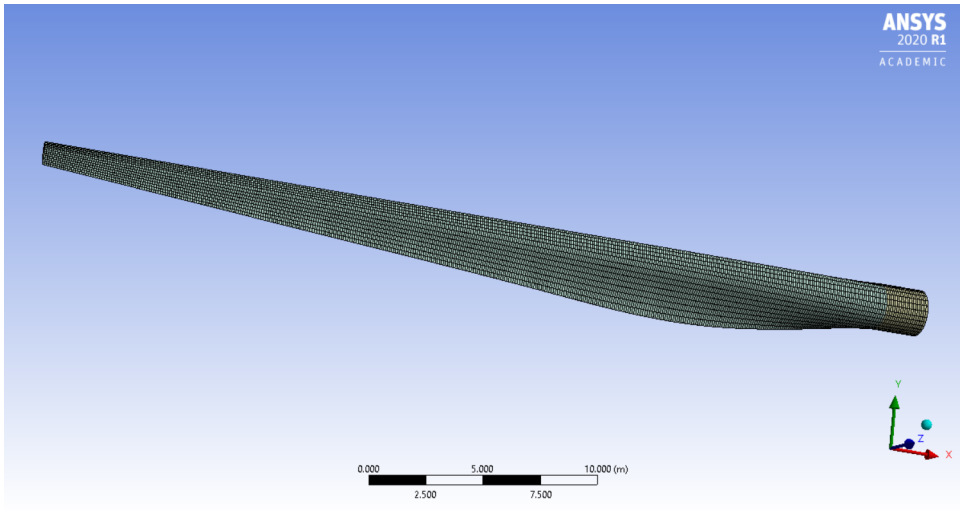

Figure 5.3.4: Detailed mesh of the blade - 1

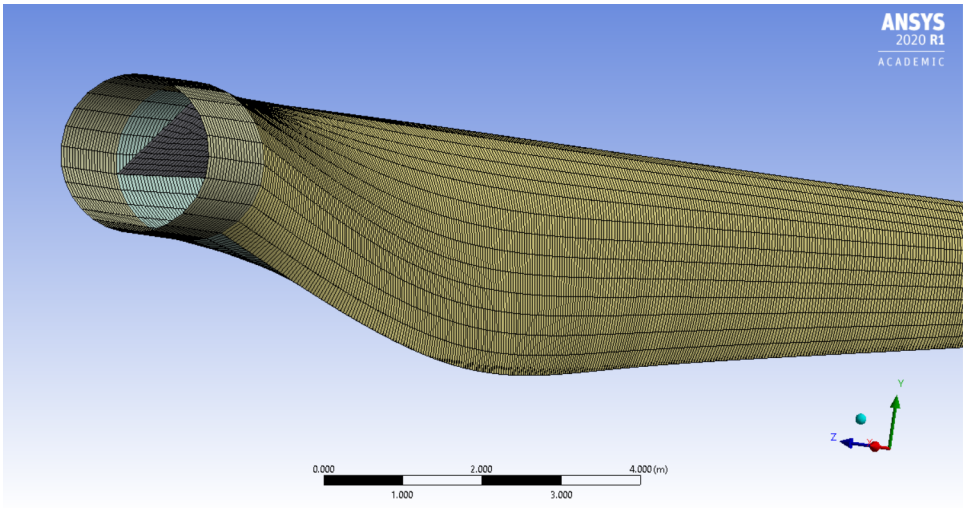

Figure 5.3.5: Detailed mesh of the blade - 2

5.3.2 Aerodynamic Results

In this section it's possible to analyze the results from the first part of this analysis, where the aerodynamics loading on the blade are detected. In the second part, the pressures on certain areas of the blade are passed as pressure loads to ANSYS Mechanical to determine stresses and deformations on the blade.

Velocity Streamlines

The first result which is shown is the velocity streamlines plot. In this plot, it's very interesting to see the clear drop in velocity behind the turbine, which is definitely the correct behaviour, as it's showing the wake behind the wind turbine. Moreover, it can be seen a clear acceleration of the flow around the wake, which is expected from mass and momentum balance. It can be proved that this behaviour matches quite well the actuator disk theory for wind turbines.

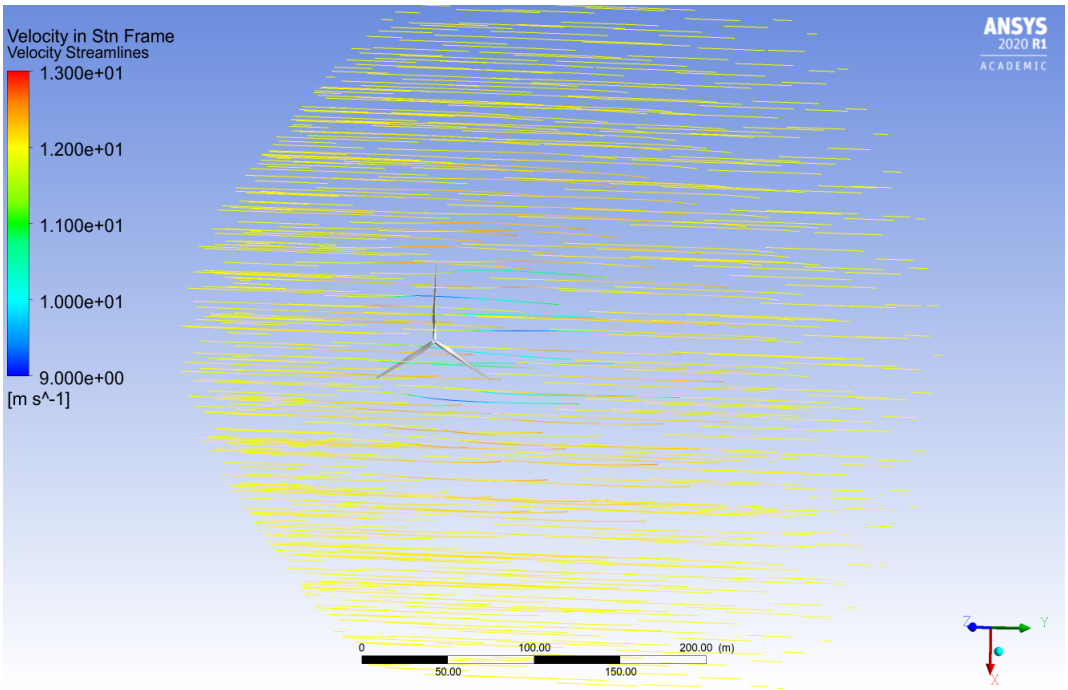

Figure 5.3.6: Velocity streamlines around the turbine

Blade Velocity

The second result which is shown is the blade velocity in standard frame, which is the frame of reference from the ground. As expected, the local blade velocity increases with radius and the velocity at the tip is the highest velocity. In this case, as it can be seen well in figure 5.3.7, the value of the velocity at the tip is about 98 m/s.

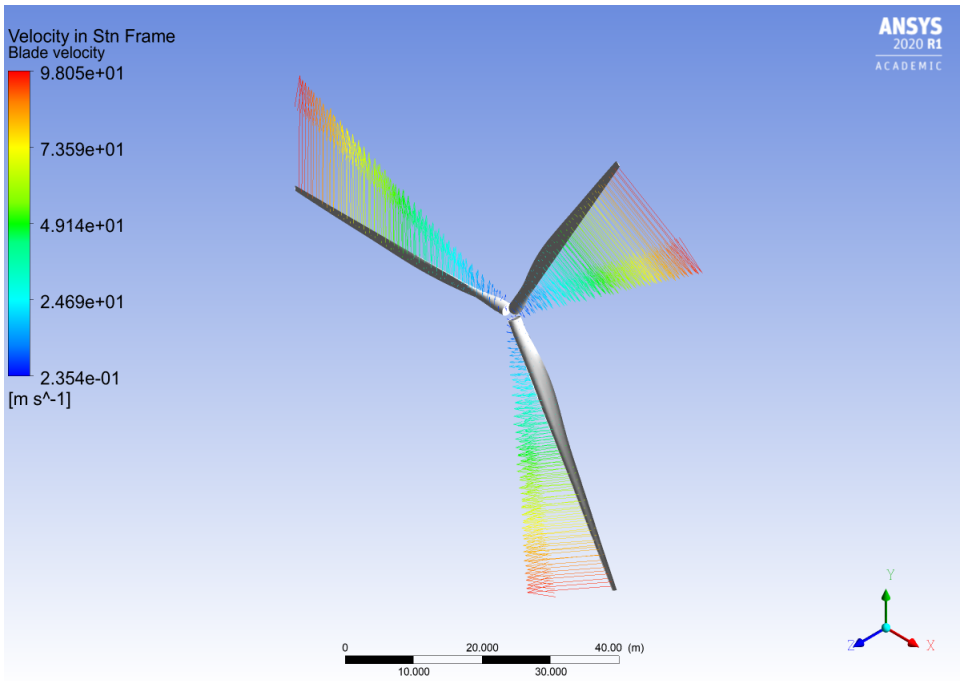

Figure 5.3.7: Blade velocity in standard frame for a 3-Blade rotor

Pressure Contours

Finally, the pressure contours on the surface of the blade are presented. The main understating from these plots is that the pressure is lower on the back surface of the blade, compared to the front surface of the blade. From the color scheme it can be seen that the red regions, which show positive pressures, have about the same magnitude as the green regions that show negative pressures. The blue regions, however, are much higher in magnitude and therefore have more weight towards the negative pressures.

So, this pressure difference between the front and the back surface creates a lift force and it points it normal to the back surface of the blade. Because the blade is not fully perpendicular to the ground, there is a component of the lift in the direction of rotation,

which is the XY plane. The component of the lift in the negative Z direction has a large effect on blade deflection, which will be analyzed in the next section of this analysis.

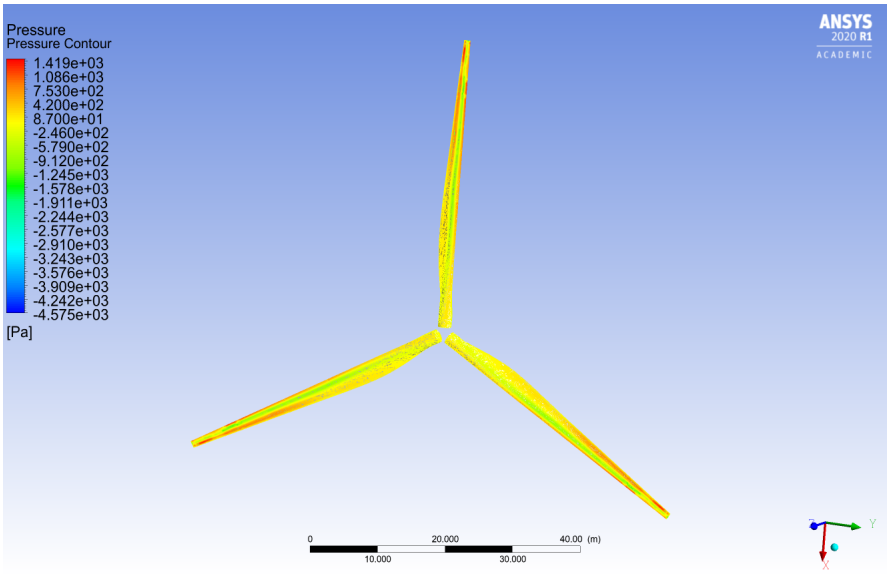

Figure 5.3.8: Pressure contour on the blade front surface

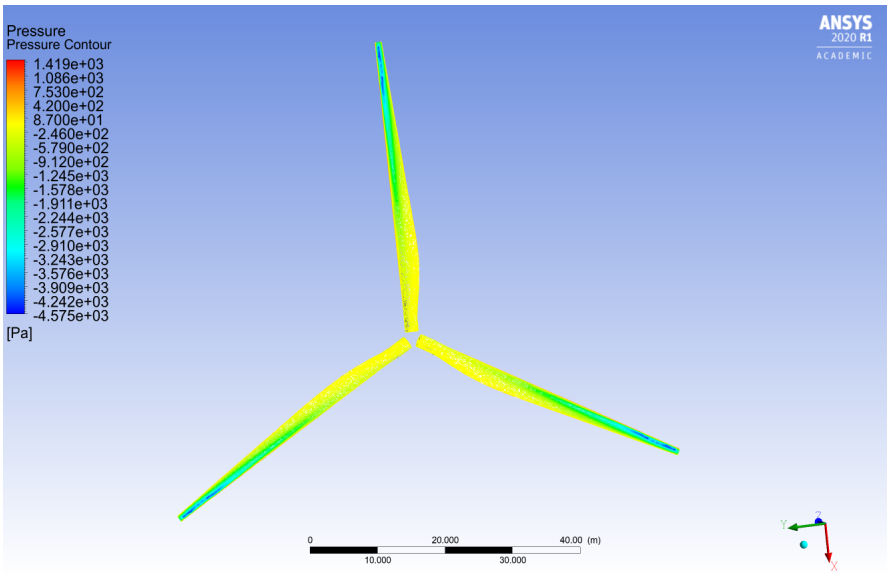

Figure 5.3.9: Pressure contour on the blade back surface

In the next Figure 5.3.10, it's possible to see the pressure contours in the Y-Z plane cutting through the blade. With this view, it can be better seen the pressure distribution around the airfoil: there is an high pressure area (red area) near the leading edge on the pressure surface, while there is a low pressure zone at the mid-span on the suction surface (blue zone). From this pressure difference between the pressure and suction surfaces, as seen before also in the 3D plot, a lift force is generated through the direction of rotation, so the X-Y plane.

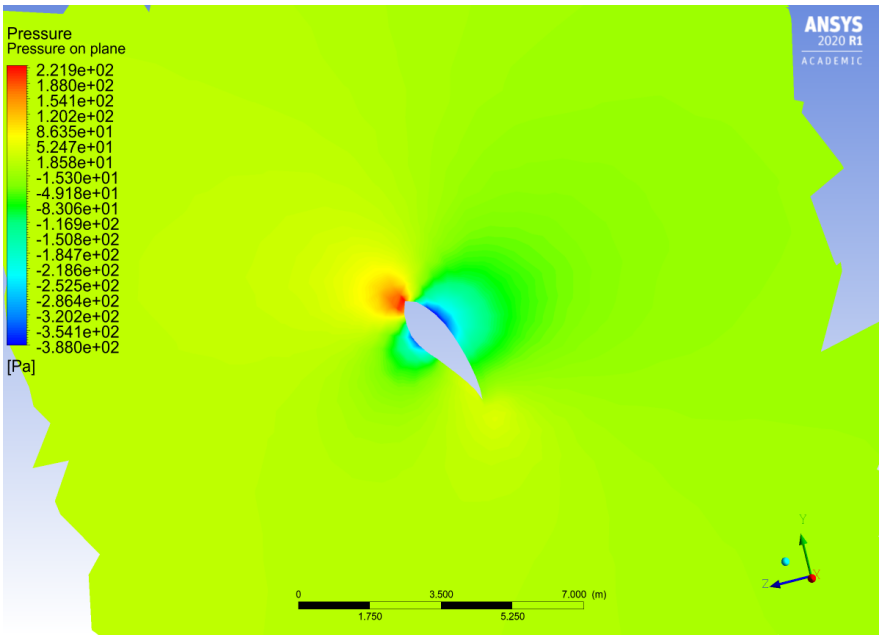

Figure 5.3.10: Pressure contour on the YZ plane

5.3.3 Aeroelastic Results

In this section it's possible to analyze the results from the second part of this analysis, in which the solid mechanics aspects of this wind turbine blade are involved. The pressure load found in the first part are imported in ANSYS Mechanical and the stresses and deformations on the blade are subsequently determined.

Wind turbine blades are now made of composite materials to reduce the weight of these massive machines. In this case, the structural analysis is simplified by assuming that the composite material can be approximated by the following orthotropic material properties (Table 5.3.1).

Table 5.3.1: Blade material properties

Density ($Kg/m3$)	1550
Young's Modulus - X (Pa)	1.14e+11
Young's Modulus - Y (Pa)	7.58e+09
Young's Modulus - Z (Pa)	7.58e+09
Poisson's Ratio - XY	0.32
Poisson's Ratio - YZ	0.37
Poisson's Ratio - XZ	0.35
Shear Modulus - XY (Pa)	5.45e+09
Shear Modulus - YZ (Pa)	2.96e+09
Shear Modulus - XZ (Pa)	2.96e+09

The blade is composed of an outer surface and an inner spar. The thickness of the outside surface linearly decreases from 0.1 m at the root to 0.005 m at the tip. The spar has a similar thickness behavior with 0.1 m at its closest point to the root and 0.03 m at the tip. In the following table, there are the thickness specifications needed along with their location with respect to the global coordinate system (which represents the center of an imaginary hub and thus the center of rotation).

Table 5.3.2: Thickness specifications

	X(m)	*Thickness (m)*
Surface	-1	0.1
	-44.2	0.005
Spar	-3	0.1
	-44.2	0.03

Total Deformation

In Figure 5.3.11 it's possible to see the deflection of the blade due to the pressure loads. As expected, the blade deflection is away from the incoming wind, like actual wind turbines do. In Figure 5.3.12 it's also possible to see the undeformed wire frame, to better understand the blade deflection from the standard unloaded configuration.

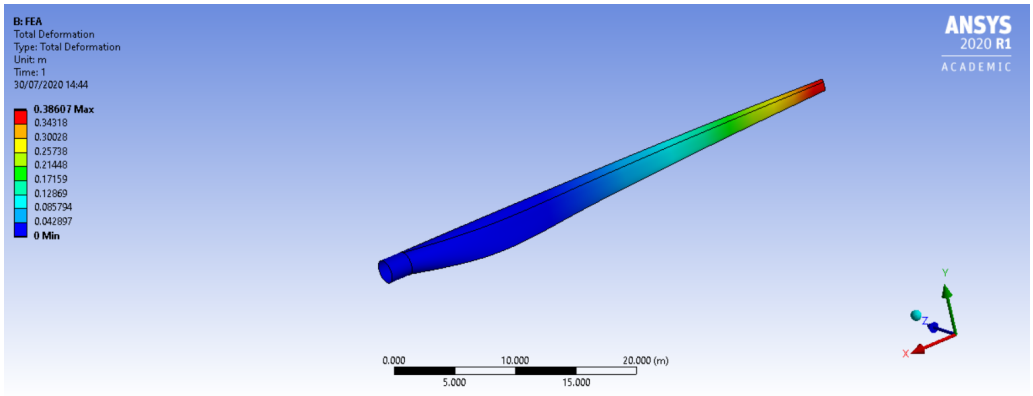

Figure 5.3.11: Blade deflection regions

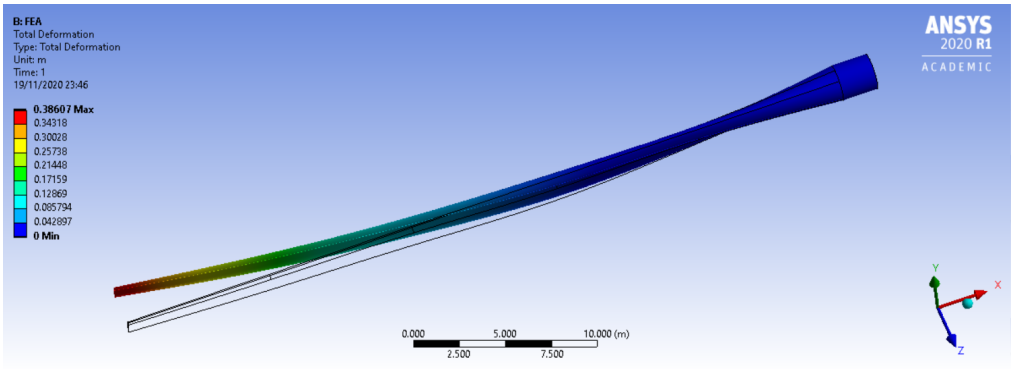

Figure 5.3.12: Blade deflection compared to unloaded case

Von Mises Equivalent Stress

Regarding the equivalent stresses, it can be seen that the maximum stress is located around the mid-span of the blade and is about 32 MegaPascal. This stress is tensile due to the deflection of the blade away from the incoming wind.

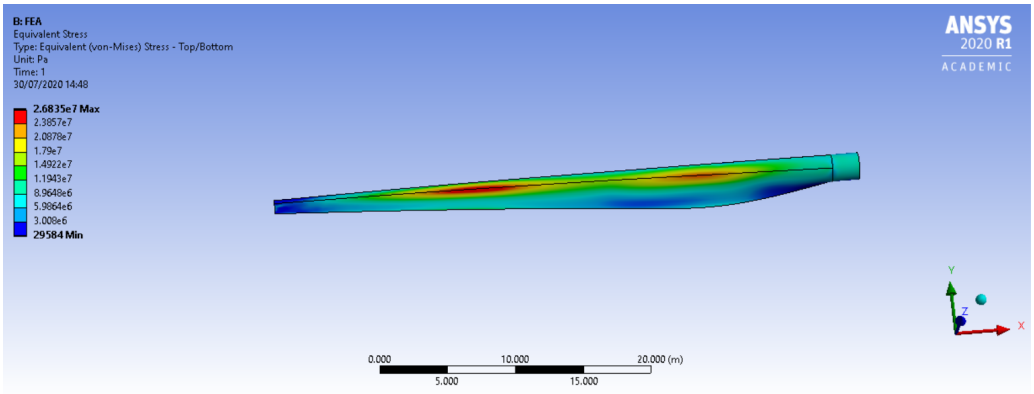

Figure 5.3.13: Equivalent stress - Blade front face

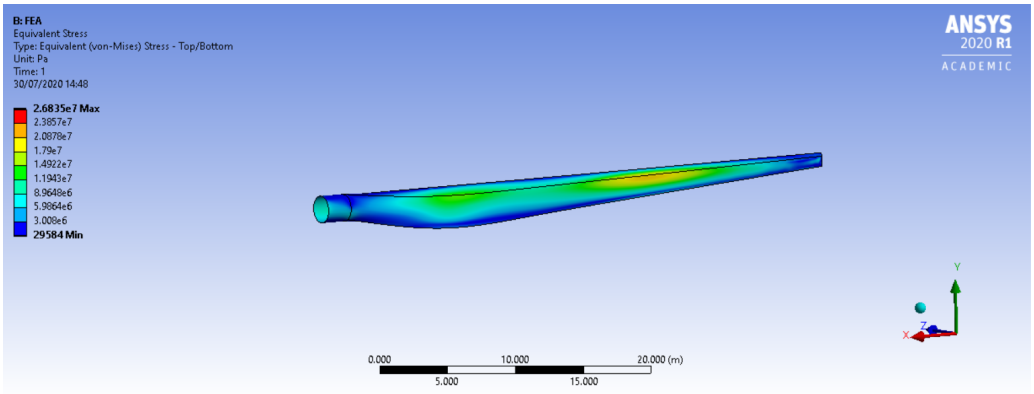

Figure 5.3.14: Equivalent stress - Blade back face

It is worth noting that in the back face of the blade, as shown in Figure 5.3.14, the stresses are lower than in the front face of the blade. Again, this is due to the direction of the deflection of the blade from the pressure loads generated by the incoming wind.

Force Reaction

Regarding the root radial force, it can be seen that almost all the force reaction is in the x-direction (more than 95% of the total force). This is absolutely normal, considering the centripetal acceleration acting on the blade. In table 5.3.3, the values of the force in all directions are computed.

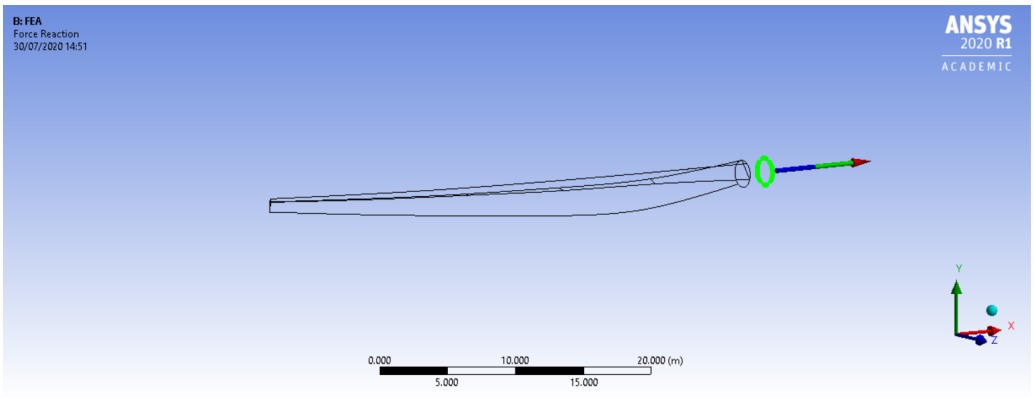

Figure 5.3.15: Root radial force

Table 5.3.3: Force values in all directions

Maximum Value Over Time	
X - Axis	1.582e+06 N
Y - Axis	16633 N
Z - Axis	64911 N
Total	1.663e+06 N

Moment Reaction

Finally, the bending moment acting on the blade is shown. In this case, the majority (almost 94%) of the reaction bending moment is about the y-axis, due to the loading on the blade and its consequently deformation.

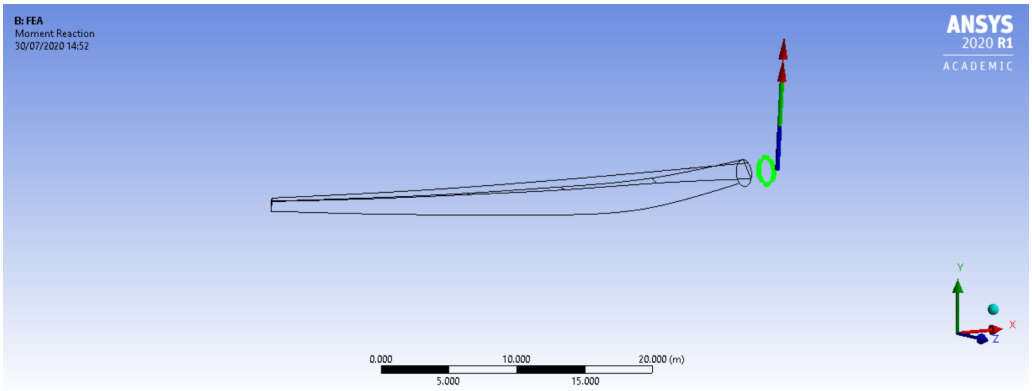

Figure 5.3.16: Bending moment reaction

Table 5.3.4: Moment values in all directions

Maximum Value Over Time	
X - Axis	23829 Nm
Y - Axis	2.26E+06 Nm
Z - Axis	1.31E+05 Nm
Total	2.413E+06 Nm

It's important to say that much more results were obtained from this structural analysis (i.e shear stresses or elastic strain), but it was decided to show just the most important results for the scope of this project.

Chapter 6

Wind Gust Analysis with ATE

The technological advancement in wind turbines is not only centred in a higher energy efficiency, but also in a more safe and economical design of the machine. From this point of view, a deeper knowledge of the environmental conditions in which the turbine has to operate is of utmost importance. Hence, methods for the prediction and simulation of a possible extreme load event have been developed. A wind gust is defined as a short term speed variation within a turbulent wind field. Its typical shape can be characterized by some parameters, as clarified in Figure 6.0.1.

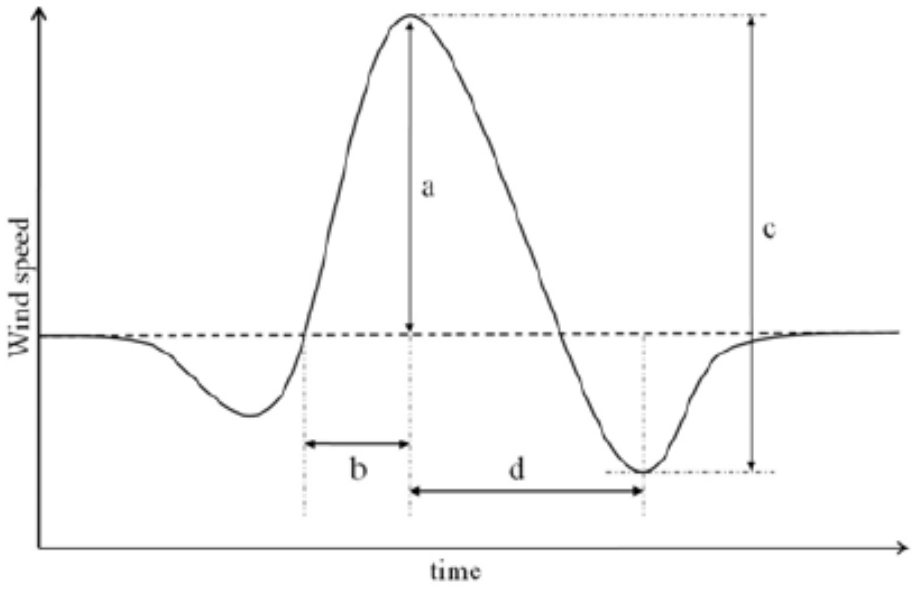

Figure 6.0.1: Characteristic parameters of an average wind gust

The flow field, incoming with an average speed u , is followed by a negative fluctuation, a positive peak and another negative pulse before stabilizing again. The gust relative amplitude a is the speed difference u–u_{max}. The gust rise time b is defined as the period between the beginning of the gust and the reaching of the maximum speed u_{max}, whereas the maximum gust variation c is the absolute difference $u_{max} - u_{min}$. The lapse time d is defined as the period between the max and min velocity occurrences. A parameter to evaluate the gust magnitude is the gust factor $G = u_{max}/u$.

6.1 Gust Models

The importance of gusts for structural issues and loading assessments, combined with their inherent random nature, promoted the development of various gust models. Average gust shapes, probability distributions and simulated wind fields were investigated. The simplest gust models derive from plain mathematical functions. These are Gaussian profiles or sinusoidal profiles, as one-minus-cosine, sine and cosine [7]. The one-minus-cosine is one of the most popular average gust shape model, due to its simplicity, and is currently adopted for load assessment in aerospace industry and international standards. However a good matching with experimental gust measurements is not always present.

Therefore more complex descriptions were investigated. Many approaches are based on the statistical approach of averaging a suitably large number of measured gusts to define a gust shape model. Larsen et al. [42] discuss a model to extract a mean speed gust shape based on the peak over threshold detection procedure. The benefit of including realistic gusts in the stochastic turbulence of the Atmospheric Boundary Layer (ABL) is explained. The original stochastic time series is transformed into a series of Dirac delta functions located at the detected gusts intervals, more precisely at the peak instant. The mean gust shape is then extracted as a function turbulence standard deviation, gust amplitude and time. The spatial shape of the gust is investigated too, by applying the previous procedure also to a second position. The produced gust shapes are then compared both with measured wind data sets and numerically simulated wind field, with good results. Various terrain conditions and atmospheric stability situations are tested too.

The availability of useful measurements for the gust assessment is limited in space and time though. Knigge and Raasch [41] performed a LES simulations to provide a virtual multi-dimensional data sets of atmospheric turbulence with all the ABL characteristics. Both 1D and 2D gust profiles were extracted by means of peak over threshold method. A comparison between the obtained 1D gust profile, the one-cosine gust shape and the measured data is performed. A noticeable difference is found between the 1D profile from Large Eddies Simulation (LES) calculation and the one-cosine shape, mostly in the steep increase and decrease of the wind speed. Therefore, an adjustment is proposed for the one-cosine formulation, parametric for each component of the velocity vector. The accuracy of the method is underlined for low altitudes, suitable for wind turbine applications.

Seregina et al. [66] demonstrate the extrapolation of wind gust velocities from common hourly measurements. The hypothesis made is that both wind and gust velocities follow Weibull distributions. Then the gust model is build as a transfer function between shape and scale parameters of the two different distributions. As gust are fluctuations of wind, the two distributions are thought to have similar shape and different scale. Therefore, the estimation of the gust speed by the combination of the two Weibull functions is explained and validated with meteorological data. Mann [63] elaborated an algorithm to simulate a complete 3D turbulent wind field with realistic ABL behaviour, including gusts and shear layer. The model is based on the spectral tensor for atmospheric turbulence at high wind speeds. The wind turbine company Vestas developed an appropriate software which generates a wind field based on Mann model and gives a 3D velocity components as output. The field is divergence-free, so mass is conserved and the use in CFD simulations is possible.

6.2 IEC Standard

Besides the deep research about wind gusts, the urgency of a safe turbine operation claims for straightforward specifications. As other works about wind turbines and gusts, the approach adopted in this analysis follows the International Electrotechnical Commission (IEC) guidelines [71]. A series of well-defined wind gust models with a set of extreme loading cases are listed in IEC 61400-2. Even if the standard is meant for design purposes, in the present work it has been used as an international reference for

the definition of a gust shape and for an immediate structural verification. For these reasons, the case which will be analyzed in this Chapter doesn't follow exactly the load cases of the standard, as the main goal is to study the aerodynamic response of the turbine in a transient operating condition.

Larger machines are provided with control systems to prevent rotor over-speed and blade overload, but the turbine has to withstand even these loads for safety and continuity reasons. In fact, a system fault is always possible. The most commonly followed procedure consists in the definition of several load cases which may represent the turbine lifetime. In the following analysis, it is considered an Extreme Operating Gust (EOG) for the case of an operative load without fault, which is the most common case, an operative load defined during the turbine normal productive operation.

6.2.1 Extreme Operating Gust

This is the most representative gust profile, a symmetric so called Mexican hat shape. Before and after the rather steep peak, a brief speed dip is included. Gust amplitude and duration vary with the return period. The analytical form is expressed by equation 6.1, for z_{hub} < 30 m, and the resulting velocity fluctuation at hub height in time is reported in Figure 6.2.1. A normal stationary profile $u(z)$ is supposed to persist up to $t = 0\ s$, when the gust begins.

$$u(z,t) = \begin{cases} u(z) & t < 0 \\ u(z) - 0.37 u_{gust}(z) sin(3\pi \frac{t}{T})(1 - cos(2\pi \frac{t}{T})) & 0 < t < T \\ u(z) & t > T \end{cases} \tag{6.1}$$

The gust period T is the total event duration, considered $12\ s$. After that time, the velocity profile goes back to $u(z)$. Hence, the EOG vertical profile shape in time corresponds to a pulsating normal profile.

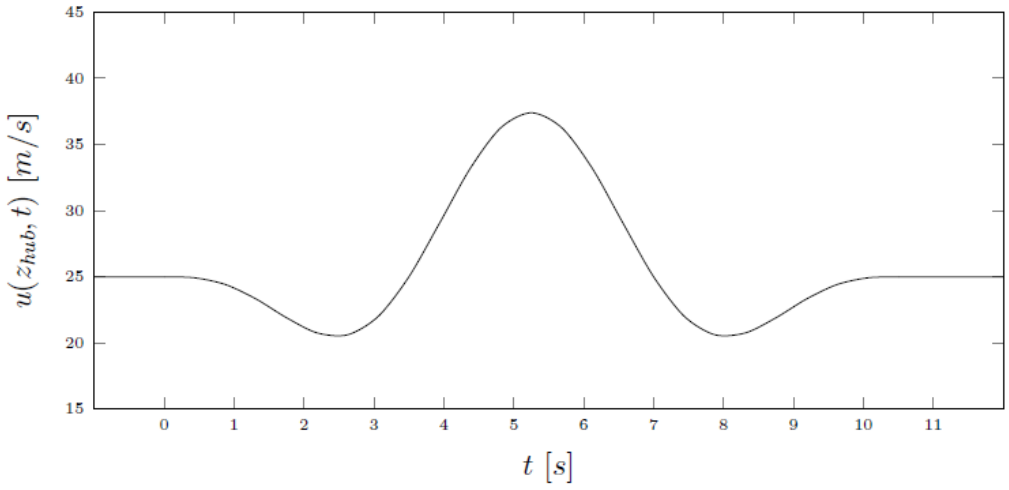

Figure 6.2.1: Canonical Mexican hat gust shape profile ($z = z_{hub} = 12.2m$)

6.3 CFD Case Configuration & Methodology

One of the main reasons for structural issues in offshore wind turbines is the presence of sudden wind gusts during a normal operation, with a resulting increase in loads the blades have to withstand. From the results in Chapter 4, it has been proved how the presence of an adaptive trailing edge flap could provide significant variations in the aerodynamic forces upon the airfoil. In particular, from Figure 4.5.16, it has been shown that the lift force in function of an increasing wind speed, has a relatively small increase when the flap is moved upwards, with a -10° configuration. From this interesting remark, it was thought to assess the influence of a movable trailing edge flap during the presence of a wind gust, in order to understand if this solution can reduce the loads upon the blades.

The same S809 airfoil used in Chapter 4 (flap length = 20% chord) was considered for this analysis, with the only difference of a small gap (1% chord) between the airfoil and the flap, as it is possible to see in Figure 6.3.1. This gap was made for the sake of the simulation, in order to allow a transient simulation with a rotating flap without the risk of a collapsing mesh or formation of negative element volumes, which would compromise or abort the computation. A Mexican hat canonical shape for the gust model was used thanks to its simple, but realistic shape, as explained in the previous sections.

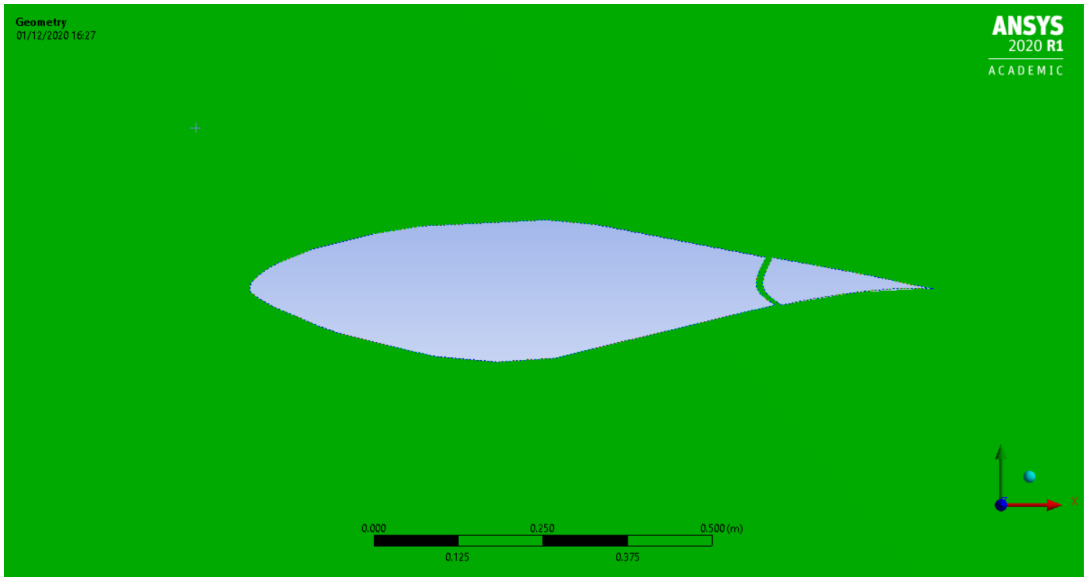

Figure 6.3.1: S809 airfoil with ATE and small gap

To assess the effectiveness of the adaptive trailing edge flap during the wind gust, it was tried to maintain the lift curve as flat as possible, like during normal operational time at rated power, with a constant free stream velocity which would generates a steady and not dangerous load on the blades.

Same CFD methodology of Chapter 4 was applied, with the only difference that in this case the simulation is transient. Time step size was set to 0.01 s with a maximum number of iterations for time step equal to 70, in order to smoothly reach convergence. A number of time steps equal to 1200 was set, so to cover all the 12 s of gust period. For the last case, with the fully transient movement of the flap, the mesh morphing technique was used in FLUENT and the mesh stiffness was improved in order to avoid mesh collapsing or formation of negative volumes during the simulation which would lead to the abortion of the computation. Inlet velocity boundary condition was again applied, but in this case it's not constant, but it varies following the Mexican hat gust shape. After this preliminary set up, 84000 iterations were launched.

6.4 Results and Analysis

6.4.1 2-D Grid & Gust Model

For grid generation, again the integrated mesh generator in ANSYS was used, due to its extensive mesh functions and ease of use. The S809 airfoil has a chord of 600 mm and 21% thickness and it is to be tested with a Reynolds number of 1.0×10^6. The chord length of the airfoil geometrical model was set to 1 m in ANSYS, which resulted a free stream air flow of about 15 m/s due to dynamic similarity. The flap length was set at 20% of the airfoil chord, so 200 mm of flap length with a gap between the airfoil and the flap of 10 mm for computational reasons.

To avoid possible effects of far field boundary on the flow around the airfoil, the grid domain was set to be 30 chord in horizontal and 30 chord in vertical direction away from the blade, as shown previously in Chapter 4, Figure 4.5.1. An unstructured triangular mesh was applied in this case to the geometrical model, with a total number of 44554 elements along with a set of structured boundary layers with quadrilateral elements (inflation layers). The boundary layer was attached on the airfoil surface with 15 layers and a relatively slow growth rate of 1.1 starting with a row depth 0.0002 m. Size function was defined for refinement around the leading and trailing edge to capture the stagnation point and wake flow respectively.

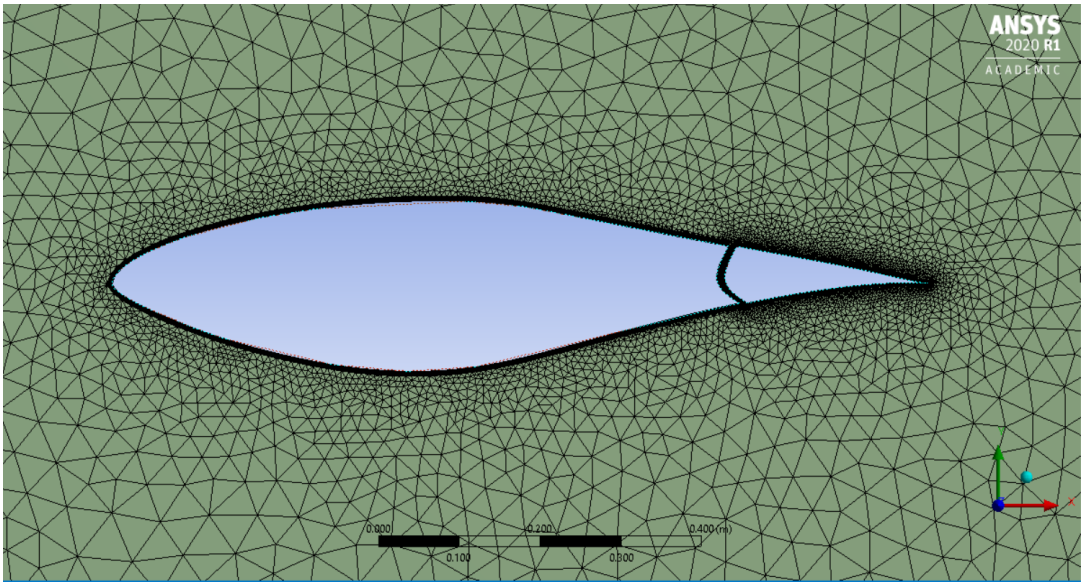

Figure 6.4.1: Detailed mesh around the airfoil

Unstructured grid is known to be more capable of conforming to desired geometries due to flexible element shapes and sizes, while compared with structured grid the computation time is expected to be longer due to the explicit storage of inter cell connectivity. In case of complex geometries or moving mesh, an unstructured mesh is suggested due to its simplicity compared to a structured one. The inner mesh around the airfoil was constructed with triangles except for the boundary layer for better geometry conforming.

Regarding the wing gust, it was modelled following the canonical Mexican hat shape from IEC, in order to consider a real model used for blade design and load forecasting. It can be seen in Figure 6.4.2 the wind gust modelled with the aforementioned standard shape, which will be also the boundary condition for the inlet wind speed considered in this simulation.

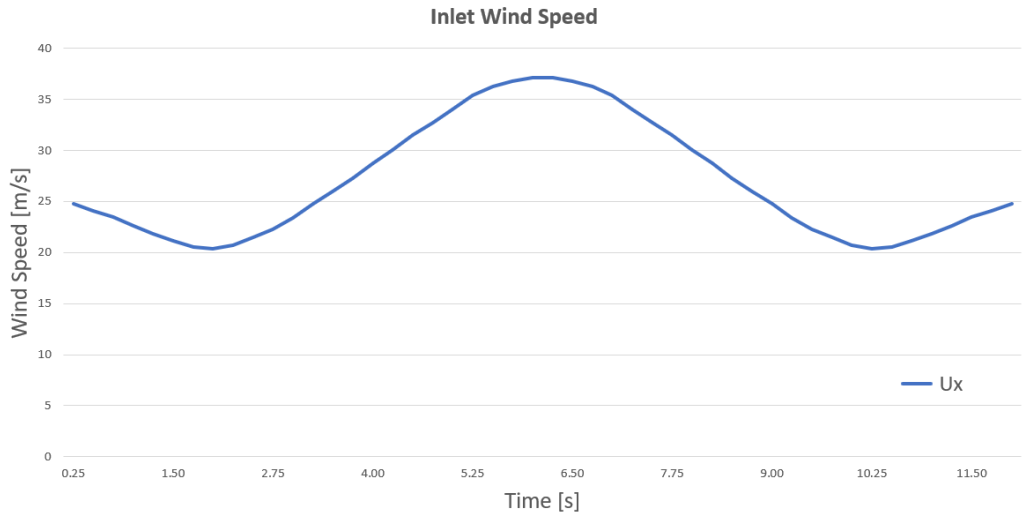

Figure 6.4.2: Inlet wind speed - mexican hat shape

The gust modelled in this Figure, follows perfectly the standard in Figure 6.2.1: before the peak, a brief speed deep is included and the peak can reach a maximum wind speed around 37 m/s. The duration of this phenomenon was considered to be around 12 s, which is a good time-scale for a gust fitting well the Mexican hat shape from IEC. In order to asses the effectiveness of the flap, it was decided to compare three different cases: initially the forces upon the airfoil are calculated without any flap control applied, later on a quasi-steady state simulation is performed in order to move the flap just during the peak of the gust, and finally a fully transient simulation with the flap moving in a continuous fashion is done.

6.4.2 Stationary Flap Response

In this first case, the forces generated by the modelled wind gust on a standard S809 airfoil are determined. It's important to underline that the geometric model is the same one of Chapter 4, but in this case the inlet velocity is changing in function of time, following the curve shown in Figure 6.4.2. For this reason, the simulation is considered to be a transient simulation due to the variable inlet wind speed and also the response of the airfoil, as expected, will change in function of the inlet wind speed. The difference between the next cases, it's in the stationary behaviour of the flap, which will be always in its standard configuration, as shown in Figure 6.4.1.

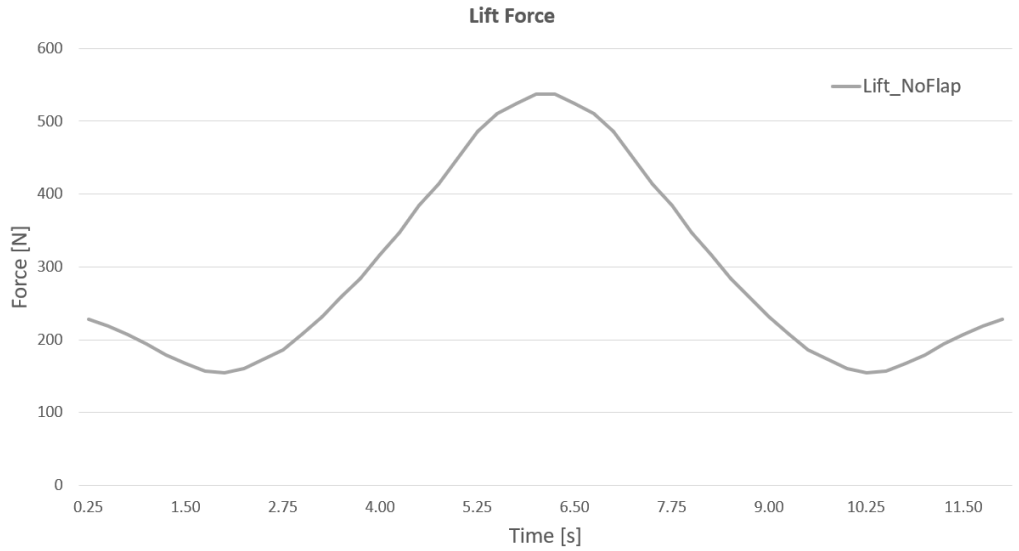

Figure 6.4.3: Lift force generated by the wind gust

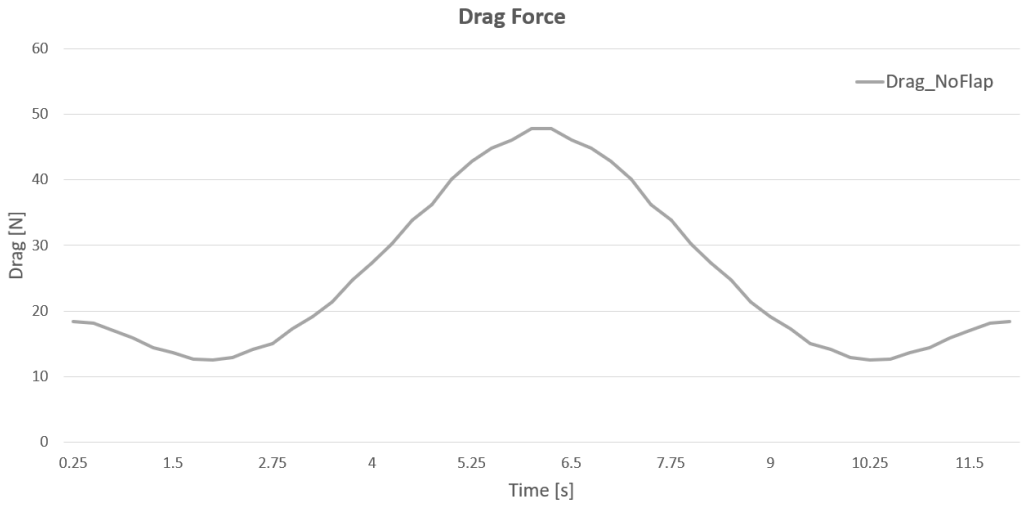

Figure 6.4.4: Drag force generated by the wind gust

The lift force L(t) and drag force D(t) monitored during the simulation are reported in Figure 6.4.3 and Figure 6.4.4. It can be seen for the lift plot that the trend reflects well the wind gust profile: coming from 25 m/s, the first value for t=0 s agrees with the lift result of the steady case with the same speed. The effect lowers, and after the peak the trend continues almost in a symmetrical way, restoring the initial value at t=12 s. Within 3 seconds from t=3 s the lift experiences a steep enhancement, with an increase of about 70% from the beginning. This strong gradient is of interest for structural ultimate and fatigue analyses of both the blade and the shaft.

Same consideration can be done also for the drag plot: the trend reflects well the wind gust profile and it's very similar to the lift plot, indeed the L/D ratio is almost constant during the whole gust ($11 \div 12$). This is due because in this aerodynamic analysis these variables depend only on the flow kinetic energy and due to their purely aerodynamic cause, the curves reflect the gust shape, with the slow oscillation period of the gust. A real blade would bend in downwind direction, so even gravitational and inertial forces would influence the result.

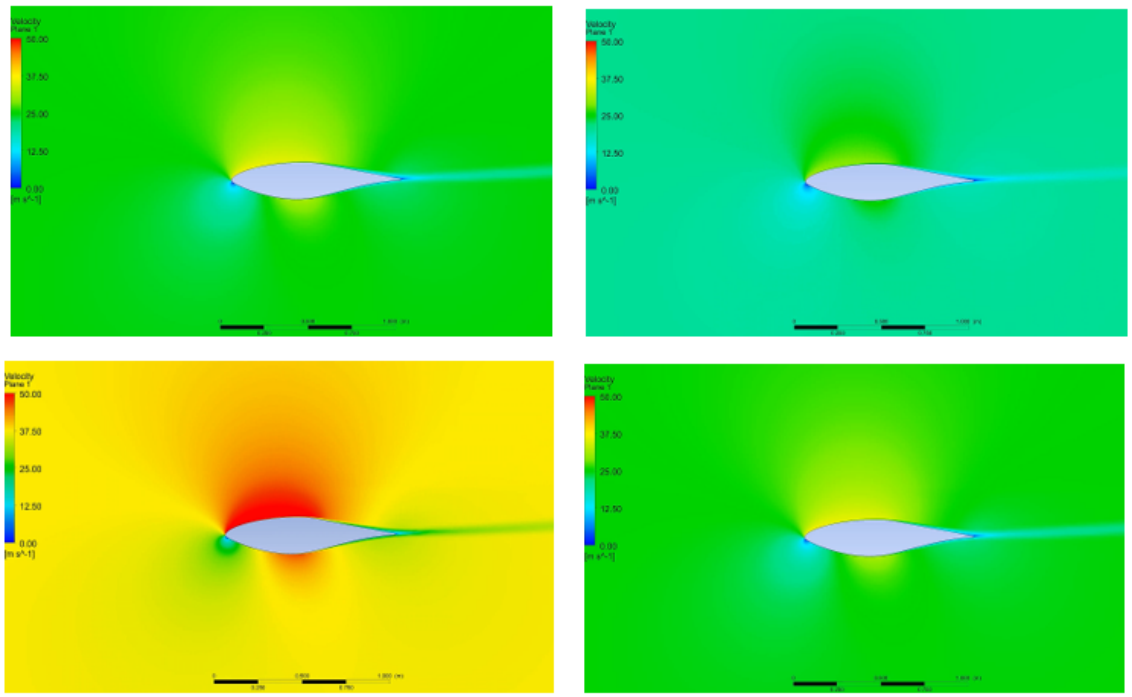

Figure 6.4.5: Velocity contours of wind gust evolution: t=0 s, t=2 s, t=6 s, t=12 s

In Figure 6.4.5 it's possible to see the evolution of the velocity contours during the analyzed wind gust with a total period t=12 seconds. In the first picture, at time t=0 s, a stable situation is shown, normally with a constant free stream velocity. In the second picture, at t=2 s, the wind speed is decreased from the stable configuration, showing the brief speed deep before the gust. In the third picture, at t=6 s, the peak with the maximum wind speed reached is shown: a big velocity enhancement is present on the suction surface of the airfoil and for Bernoulli equation, it means that a big pressure gradient is generated from the suction surface and the pressure surface, enhancing the lift force. For this reason, during the peak, the lift force experiences a steep increase as shown in Figure 6.4.3. In the last picture, at t=12 s, a stable situation after the wind gust is again reached.

6.4.3 Quasi-Steady Response

In this second intermediate analysis, it was decided to move the flap upwards by 5° (Figure 6.4.6) just during the peak, to check whether it has a positive influence on the blade loads. From a timeline point of view, the flap was moved from its stationary position at time t=0 s directly to the sloped position at t=3.5 s and finally again to the stationary one at time t=7.5 s. For this reason, the behaviour of the flap was considered to be quasi-steady respect to the changing wind speed velocity during the simulation.

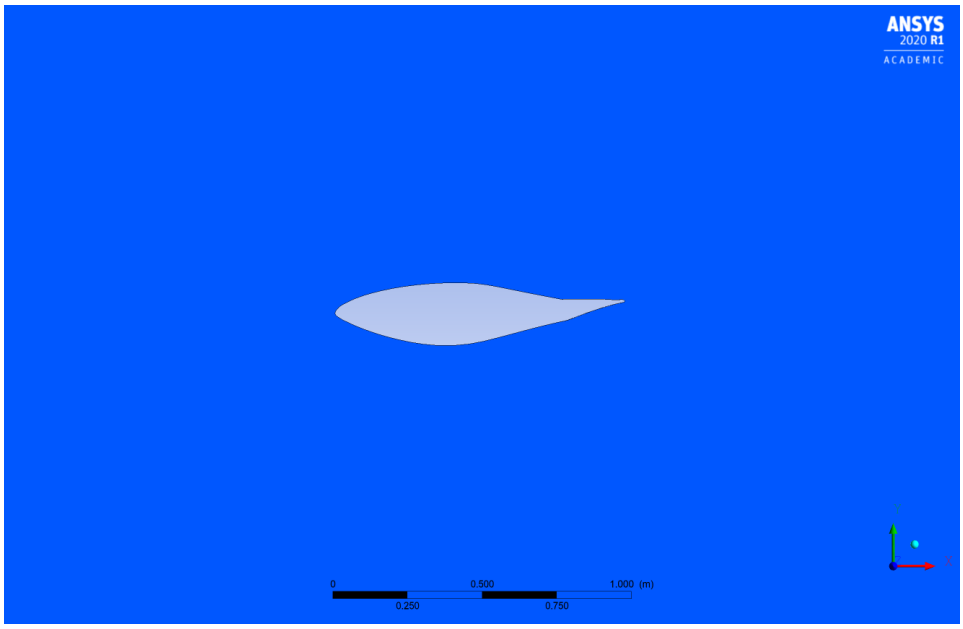

Figure 6.4.6: Airfoil configuration with flap at -5° inclination angle

The lift force L(t) monitored during the simulation is reported in the following Figure. It can be seen also in this case that the trend of the lift plot reflects the shape of the wind gust profile, but for this configuration the benefits of the flap are evident. In Figure 6.4.7 are compared the lift force for the first standard configuration (blue curve) and the second configuration with the flap moved upwards (orange curve). From t=3.5 s when the steep enhancement in wind speed starts, until t=7.5 s when the velocity starts decreasing, the peak was flatted about 40% of its original value, which means a serious and positive effect of the flap on the loads generated by this wind gust.

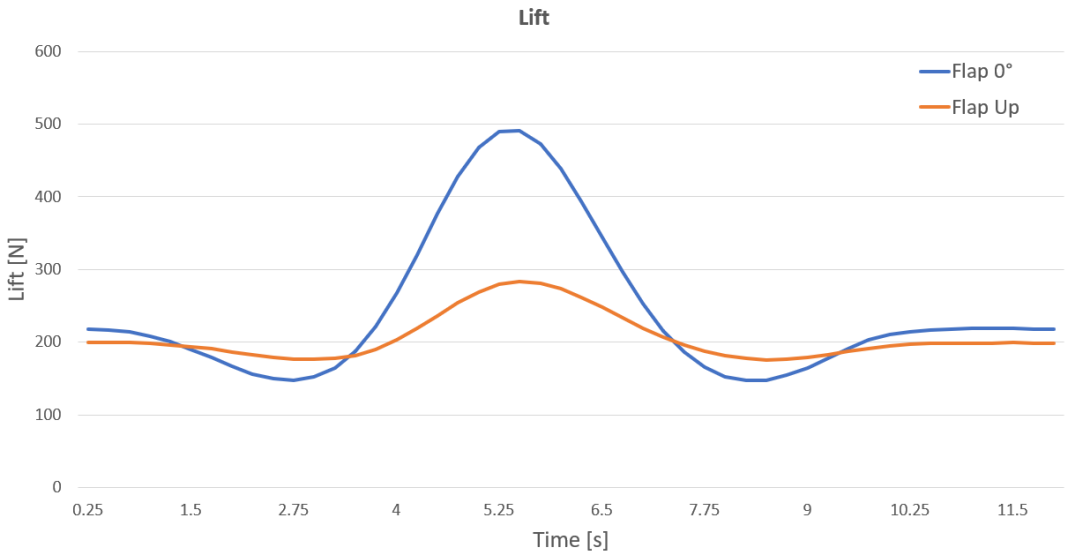

Figure 6.4.7: Lift force comparison between two flap configurations: 0° and -5°

It's possible to see that also in this case the brief speed deep before and after the peak are still present, as well as the peak in lift force is not completely flattened. The outcome for this intermediate analysis was to understand if moving the flap could give some important results from a load point of view and what was understood is that the movable flap can modify significantly the lift force generated by the gust, if it is controlled properly. The next step for this analysis, which will be shown in the next section, is to see if moving the flap in a continuous fashion during the whole wind gust can reduce completely the peak in lift and flatten the curve for the whole period of the phenomenon, like if no gust was come and the velocity remains constant, producing a constant value of lift.

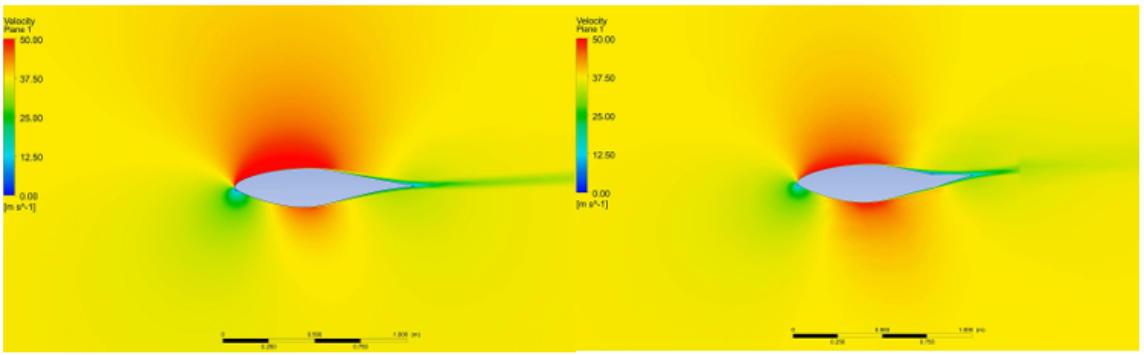

Figure 6.4.8: Vel. contours comparison between first and second case at t=3.5 s

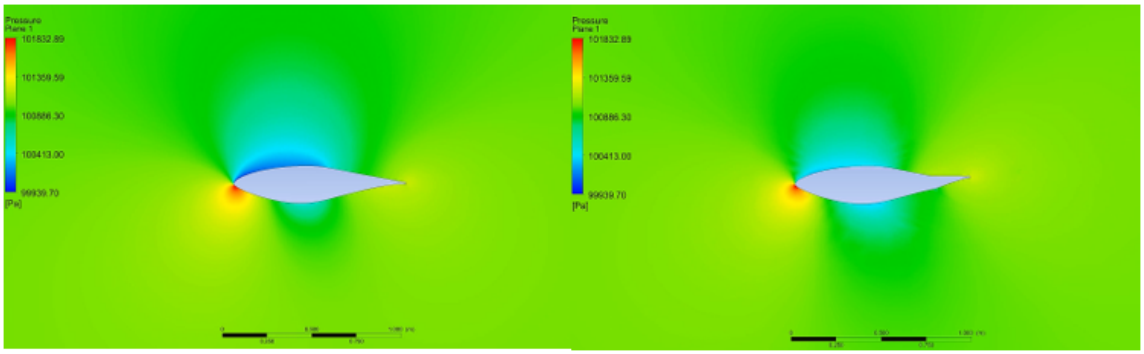

Figure 6.4.9: Pres. contours comparison between first and second case at t=3.5 s

In Figure 6.4.8 and Figure 6.4.9 it's possible to see respectively the velocity contours and pressure contours for the two configurations analyzed so far. It can be well observed that in the first configuration an higher pressure drop (velocity increment) is present in the upper surface of the airfoil. From this higher pressure difference between the suction surface and pressure surface, an higher lift force is generated by the airfoil, always perpendicular to the incoming wind speed for definition. In this condition, the flap has a fundamental contribution to decrease the loads on the blade: indeed it modifies the useful area facing the incoming wind on the pressure surface, decreasing the pressure difference between the upper and lower face of the airfoil.

Furthermore, it's interesting to see that a slight increase of pressure is created on the suction surface directly on the flap when it's moved upwards, hence it's very important to design it properly to guarantee an efficient utilization. It's important to underline that in this project all the issues related with the actuator system and sensors are not considered, due to the limited importance from an aerodynamic and aeroelastic point of view.

6.4.4 Fully Transient Response

In this last analysis, a fully transient simulation is performed. The airfoil flap is moving upwards and downwards according to the inlet velocity in a continuous fashion, in order to maintain the lift curve function as flat as possible during the wind gust. Thanks to this continuous motion of the flap and flattened lift force function, it would be possible to reduce or theoretically avoid any dynamic structural load caused by the wind gust. As explained in Chapter 4, in order to increase the lift, the flap has to be moved downwards, while to decrease the lift it has to be moved upwards. It follows that during the speed deep before and after the peak the flap inclination will have positive values, while during the peak it will have negative values.

For this computation, a fixed range of flap inclination is considered for simplicity, which is approximately between -10° and +10° from the chord line. The limits of this range were set according to several studies about trailing edge flaps applications in the wind energy sector: with this range boundaries and flap length, the stresses upon the mechanical connections between flap and airfoil are considered almost neglectable. The lift force L(t) and drag force D(t) monitored during the simulation are reported respectively in Figure 6.4.10 and 6.4.11.

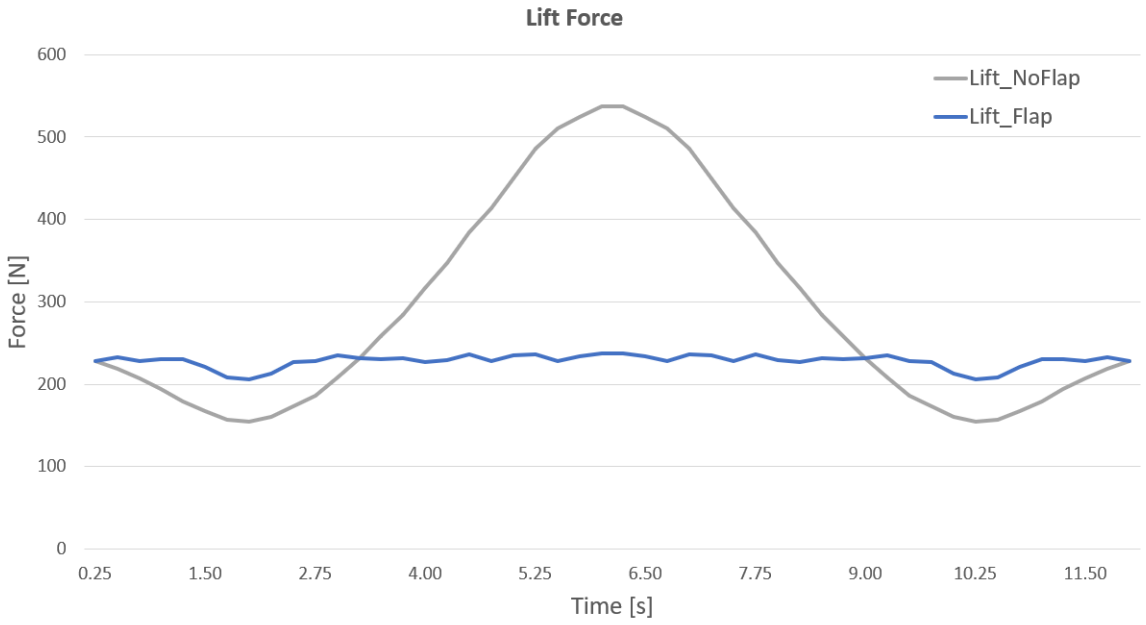

Figure 6.4.10: Lift comparison between two flap cases: 0° and movable (±10°)

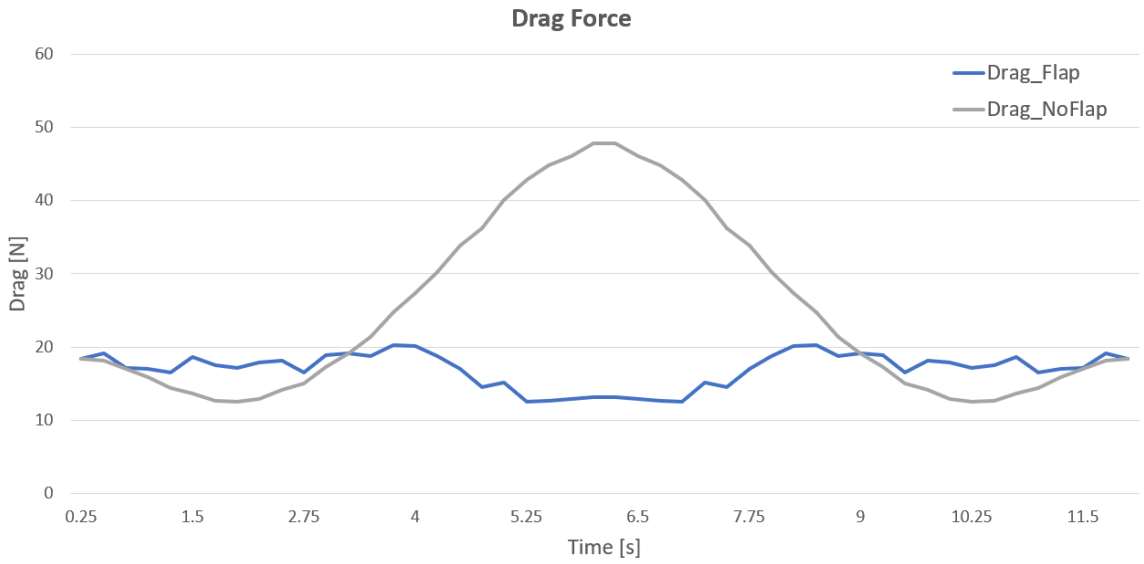

Figure 6.4.11: Drag comparison between two flap cases: 0° and movable (±10°)

It can be well observed how the continuous motion of the flap had a significant impact on the lift and drag force experienced by the airfoil. In Figure 6.4.10 the lift force for the ”No Flap” case (grey curve) has the same shape of the Mexican hat wind gust, as it was explained in the previous sections. In this case, the steep lift enhancement during the peak produces high loads the blade has to withstand, with serious problems in maintenance and reliability. In the ”Flap” case instead (blue curve), the lift force was almost completely flattened thanks to the motion of the flap, which increased the lift during the speed drop and decreased the lift during the peak.

Thanks to a smart use of the flap, it was possible to reduce significantly the lift produced by a sudden wind gust, with a resulting enormous benefit from the loads applied to the rotor blade. This result is of extreme importance, because it shows an alternative possible solution for loads control besides traditional pitch control. The main advantage of flap controls respect to pitch control, mainly during a wind gust, is that flap control has a much faster reaction than pitch control, if designed properly. Furthermore, it allows the possibility to control the loads in a local scale, without the need to pitch the whole blade if not necessary. This is also very important, because frequently high dynamic loads are applied only to a local section on the blade and pitching the entire blade would signify some losses of useful power as well.

In Figure 6.4.11 the drag force for the two cases is shown. It can be seen also in this case the positive influence of the flap, which didn't increase the drag during the gust, but instead did decreased it compared to the standard case. The L/D ratio (Glide ratio) is almost constant during the whole gust ($12 \div 15$), which is quite similar for the ratio of the first case. This means that the flap does not increase the aerodynamic efficiency of the airfoil, but it allows an important management of the loads applied to the airfoil, reducing significantly the experienced lift.

In the following Figure it's shown the flap inclination during the time period of the wind gust. As previously anticipated, during the wind speed decrease the flap was moved towards the pressure surface in order to increase the lift and maintain the curve as flat as possible, while during the gust peak it was moved to the suction surface in order to decrease the lift and reduce the aerodynamic loads, as seen before. It's interesting to observe how the flap inclination function has approximately the opposite shape of the Mexican hat gust shape, with a velocity raise before and after the central velocity drop. Knowing the behaviour of the flap in response to the inlet wind speed, through a smart sensor system it would be possible to design an ideal flap motion for every type of incoming wind gust and boundary condition.

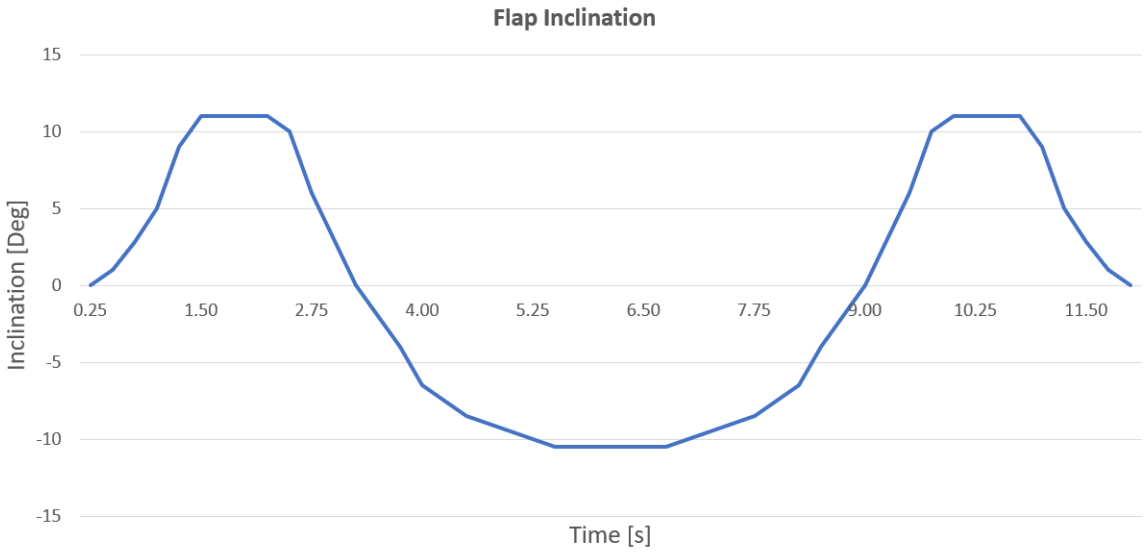

Figure 6.4.12: Flap inclination during the wind gust

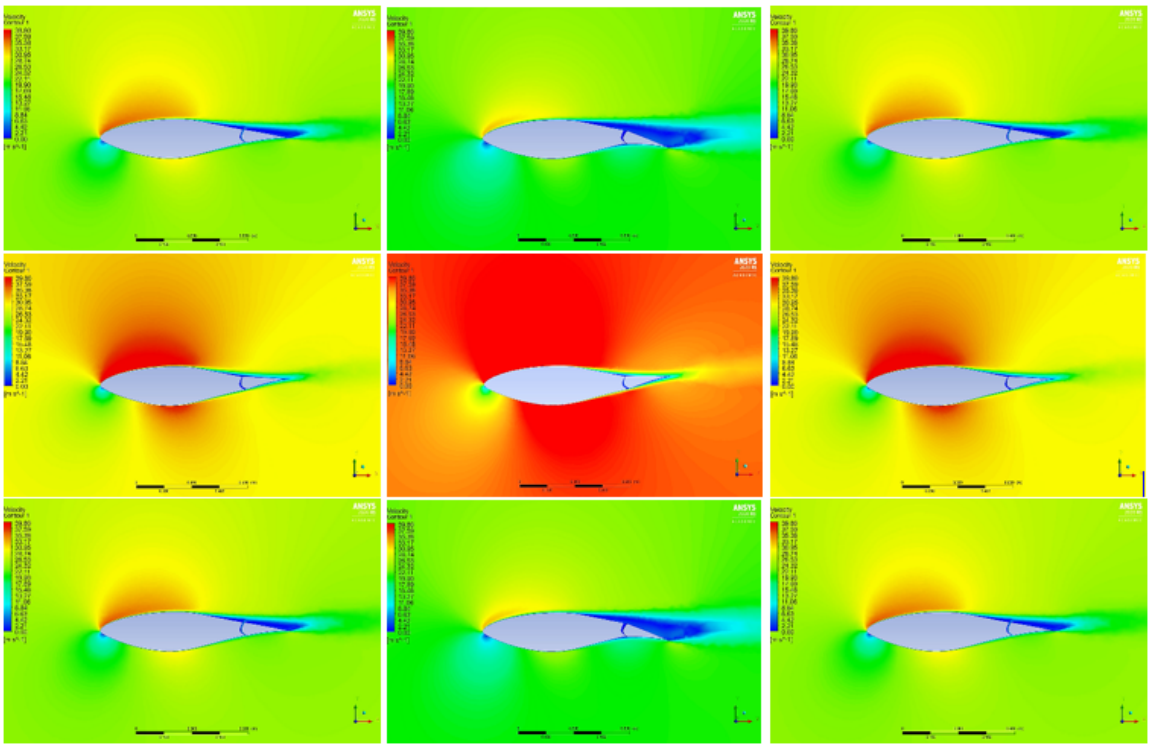

Figure 6.4.13: Velocity contours during the wind gust evolution (t=0 s → t=12 s)

In Figure 6.4.13 it's possible to see the evolution of the velocity contours during the analyzed wind gust, with a total period t=12 seconds. In the first and third row, respectively from t=0 s to t=3.5 s and from t=8.5 s to t=12 s, the brief velocity deeps before and after the peak are shown. It can be seen during the velocity decrease the motion of the flap towards the pressure surface and then its return to the initial configuration. It can be also observed that when the flap is down, a low speed (high pressure) zone is created at the end of the flap on the suction surface, which explains well the increase in lift compared to the "No flap" configuration.

In the second row, from t=3.5 s to t=8.5 s, the steep enhancement of wind velocity is reported. In this case, during the velocity increase the motion of the flap is towards the suction surface, producing an important lift reduction during the peak, as explained in the previous section.

Chapter 7

Conclusions

Since the current design trend is to have longer blades for wind turbines in order to achieve higher power output, blades are going to be less stiff and exposed to higher loads. The first objective of this project was to study the aerodynamic and aeroelastic behaviour of a wind turbine blade by investigating the interaction between the structure and the fluid, both in 2D and 3D configuration. The second objective of the project was to assess the effectiveness of a trailing edge flap applied to the studied airfoil, in order to analyzed its influence in reducing the dynamic loads applied to the blade, mainly produced during a wind gust event.

Initially, the computational model applied to a wind turbine airfoil has been successfully validated with a comparison between numerical CFD results and experimental data. The results of aerodynamic coefficients, pressure distributions and velocity contours have been confirmed. Then the behaviour of the turbine operating in unsteady conditions has been presented together with the results of the transient simulation. Through an analysis in the frequency domain of the signal generated by the oscillating airfoil, it was evaluated the low possibility of flutter for the studied geometry and boundary conditions.

Afterwards, a 3D fluid structure-interaction analysis was performed to a specific wind turbine blade, using the provided specifications. The blade model was designed with a commercial CAD software, and an aerodynamic analysis was done at the beginning. Blade velocity and pressure loads were determined in this stage, in order to have the input for the following aeroelastic analysis. The total deformation, the Von Mises

equivalent stress, the root radial force and the bending moment applied to the blade were finally calculated, in order to understand the behaviour of this blade interacting with the incoming wind.

Finally, the effectiveness of applying a trailing edge flap to the airfoil during a wind gust was assessed. Initially, the airfoil response with its standard configuration was tested: lift and drag force in function of time are reported. Afterwards, a quasi-steady computation was performed in order to observe the initial response of the flap, with positive benefits during the gust peak in reducing the lift. Lastly, a fully transient simulation was done during the entire wind gust time: the flap played a fundamental role in flattening almost completely the lift function, with positive effects in reducing the aerodynamic loads produced by a sudden wind gust.

7.1 Future Work

Based on the difficulties and uncertainties faced in this project, the following ideas are recommended to be attempted in future works so that the methods established in this project could be further validated and enhanced in term of accuracy and scope of potential applications.

Firstly, alternative sources of unsteady aerodynamic loading should be included in the analysis. Alternative sources such as variation of wind speed with height (i.e to model the atmospheric boundary layer) should be included in future analysis. This would introduce an additional dimension to the project which will allow the assessment method to be applied to assess the feasibility of constructing wind turbines in different and more realistic wind climate conditions.

Secondly, due to a limited amount of time, studies such as grid density effects and yaw angle for the 3D wind turbine were not performed, and is needed for further research. Improvement on stall prediction can also be investigated, maybe with the utilization of more complicated turbulence models like unsteady-Reynolds-Averaged Navier–Stokes (URANS), detached eddy simulations (DES) or Large Eddy Simulation (LES), in order the assess the aerodynamic performance of the wind turbine.

Thirdly, a technical and economical feasibility assessment should be done for the utilization of trailing edge flaps as load control technique for offshore wind turbines. Also a technical and economical comparison between pitch control and flap control in different unsteady conditions should be done, in order to understand the drawbacks and benefits of these control solutions and when one is better than the other. A huge study is also needed regarding the mechanical linkage between the flaps and the blade, the actuator system which controls the flap movement and all the sensors needed for a correct utilization of the trailing edge flap.

Lastly, a natural development and possible next stage for this project is to make an active wind gust control using machine learning and deep reinforcement learning techniques, in a such a way to have the flap moving automatically according to the inlet wind speed condition without any external control. In this way, it would be possible to have an optimal control of this complex dynamic system maintenance free.

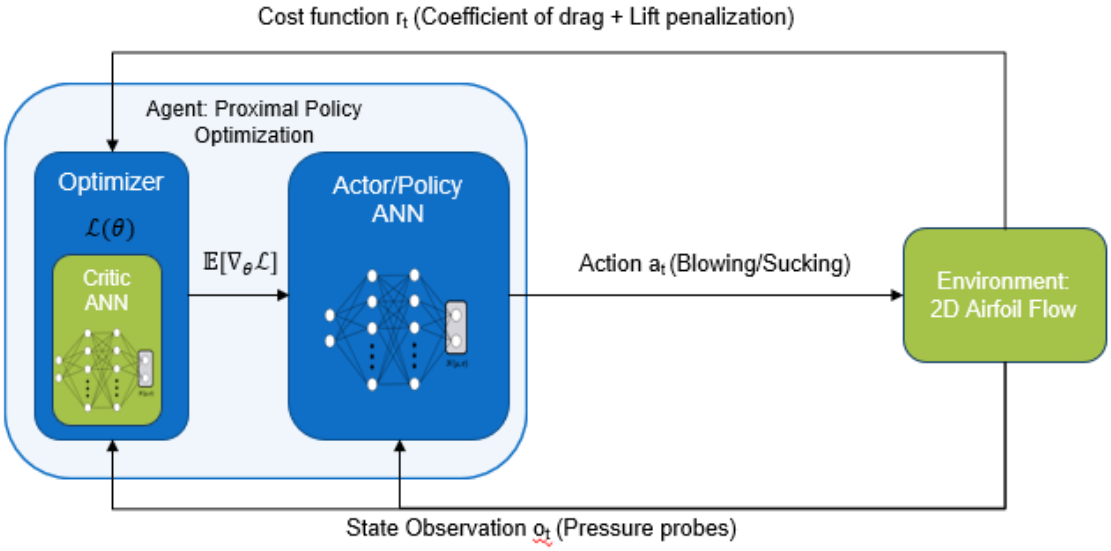

Figure 7.1.1: Deep reinforcement learning for aerodynamic optimization

Bibliography

[1] Abdel Gawad, Ahmed. “New, Simple Blade-Pitch Control Mechanism for Small-Size, Horizontal-Axis Wind Turbines”. In: *Journal of Energy and Power Engineering* 7 (Dec. 2013), pp. 2237–2248. DOI: 10.17265/1934-8975/2013.12.004.

[2] Andersen, Peter, Gaunaa, Mac, Bak, Christian, and Buhl, Thomas. “Load alleviation on wind turbine blades using variable airfoil geometry”. In: (Jan. 2006).

[3] Arakawa, C., Fleig, O., Iida, M., and Shimooka, M. “Numerical Approach for Noise Reduction of Wind Turbine Blade Tip with Earth Simulator”. In: 2005.

[4] Aslam Bhutta, Muhammad Mahmood, Hayat, Nasir, Farooq, Ahmed Uzair, Ali, Zain, Jamil, Sh. Rehan, and Hussain, Zahid. “Vertical axis wind turbine – A review of various configurations and design techniques”. In: *Renewable and Sustainable Energy Reviews* 16.4 (2012), pp. 1926–1939. ISSN: 1364-0321. DOI: https://doi.org/10.1016/j.rser.2011.12.004. URL: http://www.sciencedirect.com/science/article/pii/S136403211100596X.

[5] Bangga, Galih, Lutz, Thorsten, Jost, Eva, and Krämer, Ewald. “CFD studies on rotational augmentation at the inboard sections of a 10 MW wind turbine rotor”. In: *Journal of Renewable and Sustainable Energy* 9.2 (2017), p. 023304. DOI: 10.1063/1.4978681.

[6] Barlas, T K and Kuik, G A M van. “State of the art and prospectives of smart rotor control for wind turbines”. In: *Journal of Physics: Conference Series* 75 (July 2007), p. 012080. DOI: 10.1088/1742-6596/75/1/012080. URL: https://doi.org/10.1088%2F1742-6596%2F75%2F1%2F012080.

[7] Bartels, Robert E. “Development, verification and use of gust modeling in the nasa computational fluid dynamics code fun3d”. In: (2012).

[8] Basualdo, Santiago. “Load alleviation on wind turbines using variable airfoil geometry (a two-dimensional analysis)”. In: *Fluid Mechanics Section. Master of Science, Technical University of Denmark* (2004).

[9] Bergami, Leonardo. “Adaptive Trailing Edge Flaps for Active Load Alleviation in a Smart Rotor Configuration”. English. PhD thesis. Denmark, 2013.

[10] Binnie, A. M. and Easterling, H. J. “Hydrodynamics and Hydraulics”. In: *Journal of Fluid Mechanics* 38.4 (1969), pp. 855–856. DOI: 10.1017/S0022112069212655.

[11] Bir, Gunjit and Jonkman, Jason. “Aeroelastic Instabilities of Large Offshore and Onshore Wind Turbines”. In: *Journal of Physics: Conference Series* 75 (July 2007), p. 012069. DOI: 10.1088/1742-6596/75/1/012069.

[12] Björck, A, Dahlberg, J Aa, Östman, A, and Ganander, H. “Computations of aerodynamic damping for blade vibrations in stall”. In: *EWEC-CONFERENCE-*. BOOKSHOP FOR SCIENTIFIC PUBLICATIONS. 1997, pp. 503–507.

[13] Bossanyi, EA. “GH bladed theory manual”. In: *GH & Partners Ltd* 2 (2003), pp. 56–58.

[14] Bottasso, C.L., Campagnolo, F., Croce, A., and Tibaldi, C. “Optimization-based study of bend–twist coupled rotor blades for passive and integrated passive/active load alleviation”. In: *Wind Energy* 16.8 (2013), pp. 1149–1166. DOI: 10.1002/we.1543. eprint: https://onlinelibrary.wiley.com/doi/pdf/10.1002/we.1543. URL: https://onlinelibrary.wiley.com/doi/abs/10.1002/we.1543.

[15] Breton, Simon-Philippe. “Study of the stall delay phenomenon and of wind turbine blade dynamics using numerical approaches and NREL’s wind tunnel tests”. In: (June 2008).

[16] Buhl, Thomas and Bak, Christian. “Erratum: “Potential Load Reduction Using Airfoils with Variable Trailing Edge Geometry””. In: *Journal of Solar Energy Engineering-transactions of The Asme - J SOL ENERGY ENG* 128 (Nov. 2006). DOI: 10.1115/1.2344829.

[17] Buhl, Thomas, Gaunaa, Mac, and Bak, Christian. “Load reduction potential using airfoils with variable trailing edge geometry”. In: *43rd AIAA Aerospace Sciences Meeting and Exhibit*. 2005, p. 1183.

[18] Buhl, Thomas, Gaunaa, Mac, and Bak, Christian. “Potential load reduction using airfoils with variable trailing edge geometry”. In: (2005).

[19] Buhl, Thomas, Gaunaa, Mac, Bak, Christian, Hansen, Per, and Clemmensen, Kasper. “Measurements on the Thunder TH-6R actuator”. In: *Proceedings of the ASME2007 Fluids Engineering Division Summer Meeting, Riso*. 2005.

[20] Buning, P., Jespersen, D., Pulliam, Tom, Chan, William, Slotnick, J., Krist, Steven, and Renze, K. “OVERFLOW User”s Manual, Version 1. 8b”. In: (Jan. 1998).

[21] Carrión, M., Steijl, Rene, Woodgate, Mark, Barakos, George, Munduate, Xabier, and Gomez-Iradi, Sugoi. “Aeroelastic analysis of wind turbines using a tightly coupled CFD–CSD method”. In: *Journal of Fluids and Structures* 50 (Oct. 2014). DOI: 10.1016/j.jfluidstructs.2014.06.029.

[22] Chang, YL, Yang, SL, and Arici, O. *Flow field computation of the NREL S809 airfoil using various turbulence models*. Tech. rep. American Society of Mechanical Engineers, New York, NY (United States), 1996.

[23] Chaviaropoulos, PK. “Flap/lead–lag aeroelastic stability of wind turbine blades”. In: *Wind Energy: An International Journal for Progress and Applications in Wind Power Conversion Technology* 4.4 (2001), pp. 183–200.

[24] Chiu, Phillip. “Aerodynamics and Optimal Design of Biplane Wind Turbine Blades”. PhD thesis. University of California, Los Angeles, Jan. 2017.

[25] Dam, C., Berg, D., and Johnson, S. J. “Active load control techniques for wind turbines.” In: 2008.

[26] Duque, Earl and Johnson, Wayne. “Navier-Stokes and Comprehensive Analysis Performance Predictions of the NREL Phase VI Experiment”. In: *Journal of Solar Energy Engineering-transactions of The Asme - J SOL ENERGY ENG* 125 (Jan. 2003). DOI: 10.1115/1.1624088.

[27] Echjijem, Imane and Djebli, Abdelouahed. “Design and Optimization of Wind Turbine with Axial Induction Factor and Tip Loss Corrections”. In: *Procedia Manufacturing* 46 (2020). 13th International Conference Interdisciplinarity in Engineering, INTER-ENG 2019, 3–4 October 2019, Targu Mures, Romania, pp. 708–714. ISSN: 2351-9789. DOI: https://doi.org/10.1016/j.promfg.2020.03.100. URL: http://www.sciencedirect.com/science/article/pii/S2351978920309781.

[28] Fung, Yuan Cheng. *An introduction to the theory of aeroelasticity*. Courier Dover Publications, 2008.

[29] Gaunaa, Mac. "Unsteady 2D potential-flow forces on a thin variable geometry airfoil undergoing arbitrary motion". In: (2006).

[30] Gómez-Iradi, S and Barakos, G N. "Computational fluid dynamics investigation of some wind turbine rotor design parameters". In: *Proceedings of the Institution of Mechanical Engineers, Part A: Journal of Power and Energy* 222.5 (2008), pp. 455–470. DOI: 10.1243/09576509JPE526.

[31] Griffin, D A. "NREL Advanced Research Turbine (ART) Aerodynamic Design of ART-2B Rotor Blades". In: (Sept. 2000). DOI: 10.2172/763408.

[32] Guerri, Ouahiba, Bouhadef, Khadidja, and Harhad, Ameziane. "Turbulent Flow Simulation of the NREL S809 Airfoil". In: *Wind Engineering* 30.4 (2006), pp. 287–301. DOI: 10.1260/030952406779295471.

[33] Haidar, Muhmmad, Kamel, M., Shabka, A., and Negm, Hanan. "Flutter Investigation of Isotropic 3-D Wings". In: *International Conference on Aerospace Sciences and Aviation Technology* 15 (May 2013), pp. 1–13. DOI: 10.21608/asat.2013.22192.

[34] Hand, MM, Simms, DA, Fingersh, LJ, Jager, DW, Cotrell, JR, Schreck, S, and Larwood, SM. *Unsteady aerodynamics experiment phase VI: wind tunnel test configurations and available data campaigns*. Tech. rep. National Renewable Energy Lab., Golden, CO.(US), 2001.

[35] Hansen, M.O.L., Sørensen, J.N., Voutsinas, S., Sørensen, N., and Madsen, H.Aa. "State of the art in wind turbine aerodynamics and aeroelasticity". In: *Progress in Aerospace Sciences* 42.4 (2006), pp. 285–330. ISSN: 0376-0421. DOI: https://doi.org/10.1016/j.paerosci.2006.10.002. URL: http://www.sciencedirect.com/science/article/pii/S0376042106000649.

[36] Hansen, MH. "Aeroelastic stability analysis of wind turbines using an eigenvalue approach". In: *Wind Energy: An International Journal for Progress and Applications in Wind Power Conversion Technology* 7.2 (2004), pp. 133–143.

[37] Hansen, Morten. "Stability analysis of three-bladed turbines using an eigenvalue approach". In: *42nd AIAA Aerospace Sciences Meeting and Exhibit*. 2004, p. 505.

[38] Hansen, Morten Hartvig. “Aeroelastic instability problems for wind turbines”. In: *Wind Energy: An International Journal for Progress and Applications in Wind Power Conversion Technology* 10.6 (2007), pp. 551–577.

[39] Hoffmann, MJ, Reuss Ramsay, R, and Gregorek, GM. *Effects of grit roughness and pitch oscillations on the NACA 4415 airfoil*. Tech. rep. National Renewable Energy Lab., Golden, CO (United States); The Ohio State ..., 1996.

[40] J.G. Shepers A. J. Brand, M. M. Hand. “Enhanced Field Rotor Aerodynamics Database”. In: *IEA RD Wind Executive Committee* (1997), pp. 1–104.

[41] Knigge, Christoph and Raasch, Siegfried. “Improvement and development of one-and two-dimensional discrete gust models using a large-eddy simulation model”. In: *Journal of Wind Engineering and Industrial Aerodynamics* 153 (2016), pp. 46–59.

[42] Larsen, Gunner C and Hansen, Kurt S. “Database on Wind Characteristics–Analyses of Wind Turbine Design Loads”. In: *Risø National Laboratory, Roskilde, Denmark. Feb* (2004).

[43] Larsen, Torben J., Aagaard Madsen, Helge, and Thomsen, K. “Investigation of stability effects of an offshore wind turbine. The new aeroelastic code HAWC2”. eng. In: *Windtech International* 2.March (2006), pp. 33–35. ISSN: 15742415.

[44] Lobitz, Don W. “Aeroelastic stability predictions for a MW-sized blade”. In: *Wind Energy: An International Journal for Progress and Applications in Wind Power Conversion Technology* 7.3 (2004), pp. 211–224.

[45] Lobitz, Don W. “Parameter sensitivities affecting the flutter speed of a MW-sized blade”. In: (2005).

[46] Lutz, T, Wolf, A, Wiirz, W, and Jeremiasz, JG. “Design and verification of an airfoil with trailing edge flap and unsteady wind tunnel tests”. In: *Stuttgart, Germany* (2011).

[47] Marrant, BAH, Van Holten, Th, and Kuik, GAM van. “Smart Dynamic Rotor Control of Large Offshore Wind Turbines”. In: *Inventory of Rotor Design Options and Possible Load Reductions, Duwind* (2002).

[48] Marrant, BAH, Van Holten, Th, and Kuik, GAM van. “Smart Dynamic Rotor Control of Large Offshore Wind Turbines”. In: *Inventory of Present Techniques* (2002).

[49] Marrant, BAH, Van Holten, Th, and Kuik, GAM van. “Smart Dynamic Rotor Control of Large Offshore Wind Turbines”. In: *Inventory and assessment of available tools* (2002).

[50] Mayda, Edward, Dam, C.P., and Nakafuji, Dora. “Computational Investigation of Finite Width Microtabs for Aerodynamic Load Control”. In: (Jan. 2005). DOI: 10.2514/6.2005-1185.

[51] Nayeri Pechlivanoglu, Paschereit. “Performance Optimization of Wind Turbine Rotors With Active Flow Control”. In: *Proceedings of the ASME 2011 Turbo Expo: Turbine Technical Conference and Exposition* 1 (2011), pp. 763–775.

[52] Obeid, Sohaib, Ahmadi, Goodarz, and Jha, Ratneshwar. “NARMAX Identification Based Closed-Loop Control of Flow Separation over NACA 0015 Airfoil”. In: *Fluids* 5.3 (2020), p. 100.

[53] Øye, Stig. “FLEX4 simulation of wind turbine dynamics”. In: *Proceedings of the 28th IEA Meeting of Experts Concerning State of the Art of Aeroelastic Codes for Wind Turbine Calculations*. 1996, pp. 129–135.

[54] Pape, A Le and Lecanu, J. “3D Navier–Stokes computations of a stall-regulated wind turbine”. In: *Wind Energy: An International Journal for Progress and Applications in Wind Power Conversion Technology* 7.4 (2004), pp. 309–324.

[55] Peeters, Mathijs, Santo, Gilberto, Degroote, Joris, and Van Paepegem, Wim. “The Concept of Segmented Wind Turbine Blades: A Review”. In: *Energies* 10 (July 2017), p. 1112. DOI: 10.3390/en10081112.

[56] Petersen, J Thirstrup, Madsen, Helge Aagaard, Björck, Anders, Enevoldsen, Peder, Øye, Stig, Ganander, Hans, and Winkelaar, Danny. “Prediction of dynamic loads and induced vibrations in stall”. In: (1998).

[57] Petersen, J Thirstrup, Thomsen, Kenneth, and Madsen, Helge Aagaard. *Local blade whirl and global rotor whirl interaction*. 1998.

[58] Potsdam, Mark and Mavriplis, Dimitri. “Unstructured Mesh CFD Aerodynamic Analysis of the NREL Phase VI Rotor”. In: *47th AIAA Aerospace Sciences Meeting including The New Horizons Forum and Aerospace Exposition*. DOI: 10.2514/6.2009-1221. eprint: https://arc.aiaa.org/doi/pdf/10.2514/6.2009-1221. URL: https://arc.aiaa.org/doi/abs/10.2514/6.2009-1221.

[59] R. Reuss, M. J. Hoffmann and Gregorek, G. M. “Effects of Grit Roughness and Pitch Oscillations on the S809 Airfoil”. In: (1995), pp. 1–158.

[60] Radmanesh, Amir Reza, Abbaspour, Madjid, and Soltani, Mohamad. “Effect of Unsteady Flow over Aerodynamic Fluctuation of Different Multi MW Horizontal Axis Wind Turbine Blade Profiles on SST-K-ω Model”. In: June 2015.

[61] Rasmussen, F, Petersen, Jørgen Thirstrup, Winkelaar, D, and Rawlinson-Smith, R. “Response of stall regulated wind turbines-stall induced vibrations”. In: *Final Report on JOULE* 1 (1993).

[62] Rasmussen, Flemming, Petersen, J Thirstrup, and Madsen, H Aagaard. “Dynamic stall and aerodynamic damping”. In: (1999).

[63] Sathe, Ameya, Mann, Jakob, Barlas, Thanasis, Bierbooms, WAAM, and Van Bussel, GJW. “Influence of atmospheric stability on wind turbine loads”. In: *Wind Energy* 16.7 (2013), pp. 1013–1032.

[64] Schreck, S, Sant, T, and Micallef, D. “Rotational Augmentation Disparities in the MEXICO and UAE Phase VI Experiments: Preprint”. In: (May 2010).

[65] Sepahy, D. “Advances in Aeroelasticity”. In: *Numerical Techniques for Engineering Analysis and Design*. Ed. by G. N. Pande and J. Middleton. Dordrecht: Springer Netherlands, 1987, pp. 153–161.

[66] Seregina, Larisa S, Haas, Rabea, Born, Kai, and Pinto, Joaquim G. “Development of a wind gust model to estimate gust speeds and their return periods”. In: *Tellus A: Dynamic Meteorology and Oceanography* 66.1 (2014), p. 22905.

[67] Sieros, G., Chaviaropoulos, P., Sørensen, J. D., Bulder, B. H., and Jamieson, P. “Upscaling wind turbines: theoretical and practical aspects and their impact on the cost of energy”. In: *Wind Energy* 15.1 (), pp. 3–17. DOI: 10.1002/we.527. URL: https://onlinelibrary.wiley.com/doi/abs/10.1002/we.527.

[68] Simms, David, Schreck, S., MM, Hand, and Fingersh, L. “NREL Unsteady Aerodynamics Experiment in the NASA-Ames Wind Tunnel: a Comparison of Predictions to Measurements”. In: (Jan. 2001). DOI: 10.2172/783409.

[69] Somers, Dan M. *Design and experimental results for the S809 airfoil*. Tech. rep. National Renewable Energy Lab., Golden, CO (United States), 1997.

[70] Sørensen, N. N., Michelsen, J. A., and Schreck, S. “Navier–Stokes predictions of the NREL phase VI rotor in the NASA Ames 80 ft × 120 ft wind tunnel”. In: *Wind Energy* 5.2□3 (2002), pp. 151–169. DOI: https://doi.org/10.1002/we.64. eprint: https://onlinelibrary.wiley.com/doi/pdf/10.1002/we.64. URL: https://onlinelibrary.wiley.com/doi/abs/10.1002/we.64.

[71] Standard, IEC. “61400-2,(2006) Design requirements for small wind turbines”. In: *International Electrotechnical Commission* (2006).

[72] THEODORSEN, T. “General Theory of Aerodynamic Instability and the Mechanism of Flutter”. In: *N. A. C. A. Thecnical Report* 496 (1935). URL: https://ci.nii.ac.jp/naid/10003492039/en/.

[73] Thomsen, K, Petersen, J Thirstrup, Nim, E, Øye, S, and Petersen, B. “A method for determination of damping for edgewise blade vibrations”. In: *Wind Energy: An International Journal for Progress and Applications in Wind Power Conversion Technology* 3.4 (2000), pp. 233–246.

[74] Troldborg, Niels. “Computational study of the risø-b1-18 airfoil equipped with actively controlled trailing edge flaps”. In: *Technical University of Danmark* (2004).

[75] Tsiantas, Theofanis, Manolas, Dimitris I, Machairas, Theodore, Karakalas, Anargyros, Riziotis, Vasilis A, Saravanos, Dimitrios, and Voutsinas, Spyros G. “Assessment of fatigue load alleviation potential through blade trailing edge morphing”. In: *Journal of Physics: Conference Series*. Vol. 753. 4. 2016.

[76] Vermeer,
L.J., Sørensen, J.N., and Crespo, A. “Wind turbine wake aerodynamics”. In: *Progress in Aerospace Sciences* 39.6 (2003), pp. 467–510. ISSN: 0376-0421. DOI: https://doi.org/10.1016/S0376-0421(03)00078-2. URL: http://www.sciencedirect.com/science/article/pii/S0376042103000782.

[77] Von Karman, Th. “Turbulence and skin friction”. In: *Journal of the Aeronautical Sciences* 1.1 (1934), pp. 1–20.

[78] “Will communities “open-up” to offshore wind? Lessons learned from New England islands in the United States”. In: *Energy Research Social Science* 34 (2017), pp. 13–26. ISSN: 2214-6296. DOI: https://doi.org/10.1016/j.erss.2017.05.009.

[79] Wolfe, Walter, Ochs, Stuart, Wolfe, Walter, and Ochs, Stuart. “CFD calculations of S809 aerodynamic characteristics”. In: *35th Aerospace Sciences Meeting and Exhibit*. 1997, p. 973.

[80] Yarusevych, Serhiy, Sullivan, Pierre E, and Kawall, John G. “On vortex shedding from an airfoil in low-Reynolds-number flows”. In: *Journal of Fluid Mechanics* 632 (2009), p. 245.

[81] Zahle, Frederik, Johansen, Jeppe, Sørensen, Niels, and Graham, J. Michael R. “Wind Turbine Rotor-Tower Interaction Using an Incompressible Overset Grid Method”. English. In: *The Proceedings of the 45th AIAA Aerospace Sciences Meeting and Exhibit*. See also http://www.aiaa.org/; null ; Conference date: 08-01-2007 Through 11-01-2007. United States: American Institute of Aeronautics and Astronautics, 2007.

[82] Zhang, Zhenyou. “Automatic Fault Prediction of Wind Turbine Main Bearing Based on SCADA Data and Artificial Neural Network”. In: *Open Journal of Applied Sciences, Vol.8 No.6, June 28, 2018* ().

Appendix - Contents

Appendix A

S809 Airfoil Profile Coordinates

Upper Surface		Lower Surface	
x/c	y/c	x/c	y/c
0.00037	0.00275	0.00140	-0.00498
0.00575	0.01166	0.00933	-0.01272
0.01626	0.02133	0.02321	-0.02162
0.03158	0.03136	0.04223	-0.03144
0.05147	0.04143	0.06579	-0.04199
0.07568	0.05132	0.09325	-0.05301
0.10390	0.06082	0.12397	-0.06408
0.13580	0.06972	0.15752	-0.07467
0.17103	0.07786	0.19362	-0.08447
0.20920	0.08505	0.23175	-0.09326
0.24987	0.09113	0.27129	-0.10060
0.29259	0.09594	0.31188	-0.10589
0.33689	0.09933	0.35328	-0.10866
0.38223	0.10109	0.39541	-0.10842
0.42809	0.10101	0.43832	-0.10484
0.47384	0.09843	0.48234	-0.09756
0.52005	0.09237	0.52837	-0.08697
0.56801	0.08356	0.57663	-0.07442
0.61747	0.07379	0.62649	-0.06112
0.66718	0.06403	0.67710	-0.04792
0.71606	0.05462	0.72752	-0.03558
0.76314	0.04578	0.77668	-0.02466
0.80756	0.03761	0.82348	-0.01559
0.84854	0.03017	0.86677	-0.00859
0.88537	0.02335	0.90545	-0.00370
0.91763	0.01694	0.93852	-0.00075
0.94523	0.01101	0.96509	0.00054
0.96799	0.00600	0.98446	0.00065
0.98528	0.00245	0.99612	0.00024
0.99623	0.00054	1.00000	0.00000
1.00000	0.00000	0.00000	0.00000

Appendix B

NREL Phase VI Turbine Blade Root Surface Depiction

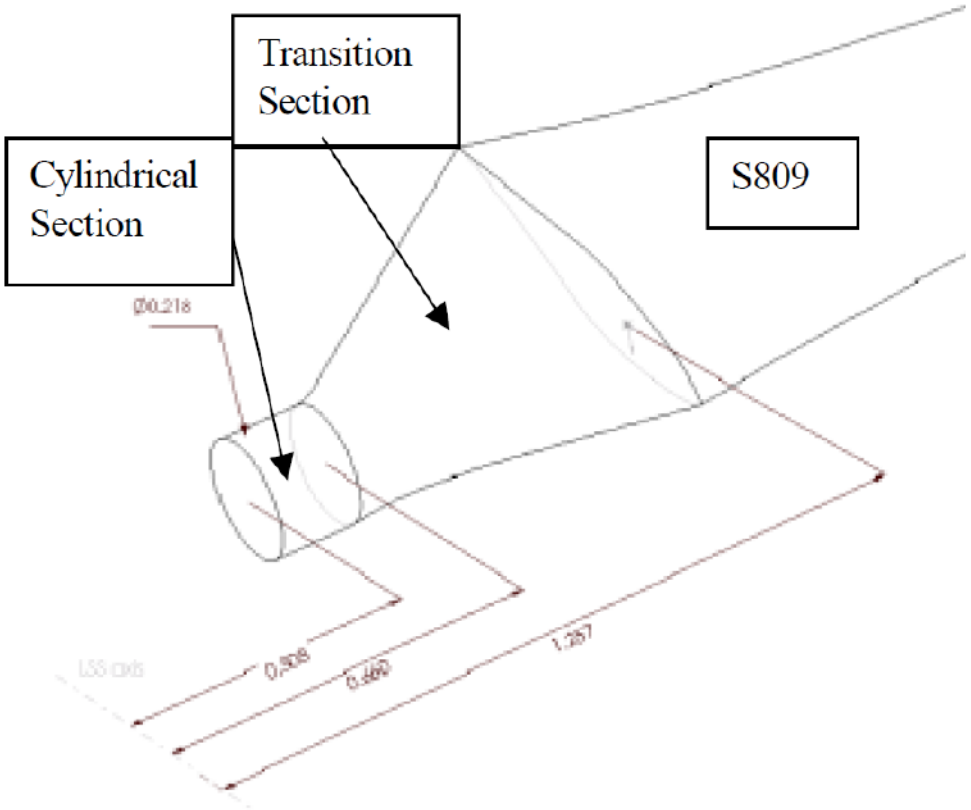

(Source: Hand et al, 2001)

Appendix C

Data for NREL Phase VI Turbine

- Number of blades: 2
  - Rotor diameter: varies with tip attachment
  - 10.058 m with standard tip or smoke tip (all sequences except V and W)
  - 9.886 m with tip plate (Sequence V)
  - 11.064 m with tip extension (Sequence W)
- Hub height: 12.192 m
- Type of rotor: teetered (Sequences B, C, D, G, and 4) or rigid
- Rotational speed: 71.63 RPM synchronous speed, 90 RPM (Sequence X only)
- Cut in wind speed: 6 m/s some tests were run at 5 m/s
- Power regulation: stall
- Rated power: 19.8 kW
- Tilt: 0°
- Cone angle: 0° , 3.4° , or 18°
- Location of rotor: upwind or downwind
- Rotational direction: counter clockwise (viewed from upwind)
- Rotor overhang: 1.401 m (yaw axis to blade axis); 1.469 m (yaw axis to teeter pin)

(Source: Hand et al, 2001)